IPP-Report

Max-Planck-Institut
für Plasmaphysik

Nille, D.

Comparison between 1D and 2D approximations describing heat diffusion in the ASDEX Upgrade Divertor

IPP 2019-03
Februar 2019

ulm university universität
uulm

Universität Ulm | 89069 Ulm | Germany
Fakultät für Naturwissenschaften

Max-Planck-Institut
für Plasmaphysik

Comparison between 1D and 2D approximations describing heat diffusion in the ASDEX Upgrade Divertor

Abschlussarbeit an der Universität Ulm
zur Erlangung des akademischen Grades
Master of Science

Vorgelegt von:
Dirk Joachim Nille
dirk.nille@uni-ulm.de

Gutachter:
PD Dr. Emanuele Poli
Dr. Thomas Eich

Betreuer:
Dr. Thomas Eich

Fassung vom 21. Januar 2016

Abstract

Power exhaust is a major issue for the development and design of a fusion power plant. This thesis addresses diffusive heat transport in the scrape-off layer, with focus on the divertor region. Target heat flux density profiles are described by a 1D model, assuming an exponentially decaying heat flux profile at the X-point and spreading of the heat in the divertor region by perpendicular diffusion. Recent measurements revealed a characteristic deviation of target heat flux profiles from the 1D model. This motivates a comparison of the 1D model and measured heat flux profiles to simulations of the scrape-off layer heat transport solving the 2D heat diffusion equation. Experimental target heat flux profiles are obtained in the tokamak ASDEX Upgrade by infrared thermography. In addition, Langmuir probe data from JET are analysed.

In this thesis a numerical code to solve the 2D heat diffusion equation in the scrape-off layer is developed. Different temperature dependencies of the perpendicular diffusion, including Bohm- and Gyro-Bohm-like, are studied. Parallel transport is described by Spitzer-Härm conductivity. The 2D simulation exhibits the same deviation from the 1D model as the experimental data. The deviation from the 1D model to the 2D simulation is similar for a variety of boundary conditions and different temperature dependencies of the perpendicular diffusivity.

The 1D model describes the point spread function of the divertor as a Gaussian, the fundamental solution of the 1D heat diffusion equation. By deconvolving the target heat flux profile obtained in simulations with the X-point profile a deviation from this Gaussian is found. This deviation is characteristic for the temperature dependence of the perpendicular transport. Alternative fit functions are introduced and their applicability to measured data is assessed. These functions describe the target profiles better than the 1D model, but no physical interpretation of the parameters describing the heat spreading is found yet.

Fitting the profiles in the inner and outer divertor for single null configuration yields distinct heat flux decay lengths $\lambda_{q,i}$ for the inner and $\lambda_{q,o}$ for the outer target. Neither the 1D model nor the alternative fit functions are able to describe the target heat flux profiles with a single λ_q.

Analysing the applicability of the two point model, neglecting perpendicular transport, leads to an approximation of the divertor spreading S, describing its decrease with increasing target separatrix temperature found in experiments.

Zusammenfassung

Eine große Herausforderung für die Entwicklung eines zukünftigen Fusionskraftwerks ist die Leistungsabfuhr. Diese Arbeit behandelt den diffusiven Wärmetransport in der Abschälschicht, mit Fokus auf den Divertorbereich. Profile der Wärmeflussdichte auf den Divertor werden mit einem 1D Modell beschrieben, das ein exponentiell abfallendes Wärmeflussprofil am X-Punkt und dessen Verbreiterung über Diffusion senkrecht zu den Feldlinien annimmt. Aktuelle Messungen zeigen eine charakteristische Abweichung des Divertorprofils zum 1D Modell. Diese Abweichung motiviert einen Vergleich zwischen dem 1D Modell und gemessenen Wärmeflussprofilen mit Simulationen des Wärmeflusses in der Abschälschicht durch lösen der 2D Wärmeleitungsgleichung. Die experimentellen Wärmeflussprofile wurden im Tokamak ASDEX Upgrade mittels Infrarot Thermographie gemessen. Zusätzlich werden Daten von Langmuirsonden in JET analysiert.

In dieser Arbeit wurde ein numerischer Code zum Lösen der 2D Wärmeleitungsgleichung in der Abschälschicht entwickelt. Verschiedene Temperaturabhängigkeiten der Senkrechtdiffusion, einschließlich Bohm- und Gyro-Bohm-artig, werden untersucht. Der parallele Transport wird mittels Spitzer-Härm Konduktivität beschrieben. Die 2D Simulation zeigt die gleiche Abweichung vom 1D Modell wie die experimentellen Daten. Die Abweichung vom 1D Modell zur 2D Simulation ist für diverse Randbedingungen und Temperaturabhängigkeiten der Senkrechtdiffusion vergleichbar.

Das 1D Modell beschreibt die Punktspreizfunktion des Divertors als Gauß-Verteilung, der Fundamentallösung der 1D Wärmeleitungsgleichung. Die Entfaltung des durch die Simulation erhaltenen Divertorprofiles mit dem Profil am X-Punkt zeigt eine Abweichung zu dieser Gauß-Verteilung. Diese Abweichung is charakteristisch für die Temperaturabhängigkeit des Senkrechttransports. Alternative Funktionen zur Beschreibung des Wärmeflusses werden eingeführt und ihre Anwendbarkeit auf gemessene Daten geprüft. Diese Funktionen beschreiben die Divertorprofile besser als das 1D Modell, aber es wurde noch keine physikalische Interpretation für die Parameter die diese Verbreiterung beschreiben gefunden.

Wärmeflussprofile des inneren und äußeren Divertors mit dem 1D Modell zu beschreiben liefert unterschiedliche Wärmeflussabfallängen $\lambda_{q,i}$ für den inneren und $\lambda_{q,o}$ für den äußeren Divertor. Weder das 1D Modell noch die alternativen Funktionen können die Profile mit einem einzigen λ_q beschreiben.

Eine Analyse der Anwendbarkeit des Zweipunktmodells unter Vernachlässigung des Senkrechttransports führt zu einer Abschätzung der Divertorverbreiterung S und beschreibt dessen Abnahme mit zunehmender Divertortemperatur an der Separatrix.

Name: Dirk Joachim Nille Matrikelnummer: 734180

Selbstständigkeitserklärung

Ich erkläre, dass ich die Arbeit selbständig verfasst und keine anderen als die angegebenen Quellen und Hilfsmittel verwendet habe.

Ulm, den .....

Dirk Joachim Nille

Contents

1.Introduction

Reliable, sustainable energy is an important part in our way of living and will be even more relevant in the future, as the economic status of billions of human beings will rise. This connects basic necessities like clean and affordable drinking water with sources of electric power, which don't rely on fossil fuels. One way to produce electricity in the future could be to mimic the energy releasing process in stars and use nuclear fusion in power plants. In principle fusion can be used in a CO_2-emission-free power plant, without long living nuclear waste. Closest to this goal is the confinement of hot plasma in a magnetic cage, realised in the so called tokamak.

In this work a detailed investigation of the heat transport onto the material wall surrounding the plasma is shown. This chapter presents an overview of the basics of fusion and possible confinement methods. For magnetic confinement of plasma, for example a tokamak, the limiter and divertor configuration are explained. For the fusion relevant divertor configuration the heat flux onto the wall is outlined. Quantifying the underlying processes is important for the design of a fusion power plant and focus of this thesis.

1.1. Basics of Fusion

In this section the fundamental principles of nuclear fusion are introduced, starting with a comparison to nuclear fission. Afterwards the Lawson criterion is presented, describing the operational parameters required to achieve a self sustained fusion reaction.

1.1.1. Fusion as a Source of Energy

Nuclear fission is an established tool to gain energy in what is commonly called a nuclear power plant. A heavy nucleus like uranium is split and the resulting mass defect is released as energy, as quantified by $E = mc^2$. There is another way to obtain energy using the opposite process: nuclear fusion.

If two light nuclei fuse to a heavier one, the net mass is reduced and energy is released. Iron is the nucleus with the highest binding energy per nucleon, therefore lighter nuclei will release energy by fusion, heavier ones by fission. The energy gained per

reaction is in the order of MeV. The energy density with respect to the reactant mass is about six orders of magnitude larger compared to chemical reactions – e.g. burning fossil fuels – with binding energies in the order of eV. This is one reason for the success of nuclear fission to gain energy, which stands against the issue of long lived radioactive isotopes ($\tau \simeq 10^6$ a).

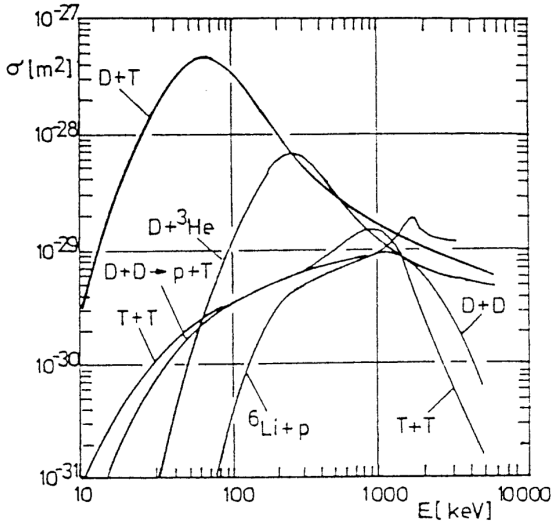

Figure 1.1.: Cross section of fusion reaction for different nuclei combinations [1]. Note the high cross section of the DT-reaction at comparably low energies.

Fusion of two isotopes of hydrogen, deuterium D and tritium T, is favoured for the use in a fusion power plant. Reason is the highest cross section at the lowest energy of 64 keV of all fusion reaction, as shown in figure 1.1. This is because He^5 – the resulting nucleon – has an excited state 64 keV above the combined mass equivalent of D and T. This isotope of helium is not stable and decays to He^4, a neutron and energy:

$$D + T \rightarrow He^5 \rightarrow He^4 + n + 17,6\,MeV \tag{1.1}$$

The side product of this reaction is a neutron, which is absorbed in the first wall and can lead to unstable isotopes in the wall material. Since the wall materials can be chosen such as to form mostly stable elements under neutron irradiation, the known issue of fission and its long lived products can be mitigated. The exhaust is then only non-toxic and stable helium. In the process of DT fusion 17.6 MeV of energy are released, dividing to 14.1 MeV kinetic energy to the neutron and 3.5 MeV to the He^4.

The need for kinetic energies in the order of several tens of keV is due to the repulsive electrostatic potential, which has to be overcome. Temperatures of around 10 keV

are sufficient to achieve fusion, which is about 100 million Kelvin. Reasons for this is the tunnel effect and the energy distribution for a given temperature. In the end, 100 million Kelvin are a reachable temperature, but do prohibit the use of solid walls to contain the particles. This temperature is several orders of magnitude above the ionisation energy, resulting in a separation of electrons and nuclei. This is called plasma, the fourth state of matter. It can be influenced by electric and magnetic fields, providing a way for confinement.

1.1.2. Lawson Criterion

To achieve self sustained fusion, certain conditions with respect to particle density and temperature have to be fulfilled. First, power produced by fusion has to compensate the energy losses to the surrounding. Two major loss channels can be identified: plasma transport with power loss density P_{trans} and radiation with P_{rad} [1]. As the motion of neutrons is not influenced by the magnetic field and their interaction with particles in the plasma is negligible, their energy is not available for further fusion reactions. Thus only the fraction

$$P_\alpha = P_{fusion} - P_n = 0.2 \cdot P_{fusion} \tag{1.2}$$

of the fusion power density P_{fusion} is available for the power balance:

$$P_\alpha \geqslant P_{trans} + P_{rad} \tag{1.3}$$

Bremsstrahlung is the dominant radiation process in the core, leading to the radiation power density

$$P_{rad} \simeq P_{brems} = c_B \, n_e^2 \, Z_{eff} \, T^{1/2} \tag{1.4}$$

for electron density n_e, Temperature T, effective ion charge Z_{eff} and the factor $c_B = 5.3 \cdot 10^{-37}\mathrm{Wm}^3$.

For plasma transport of heat no such expression is available, therefore the energy confinement time τ_E is introduced as the ratio of the thermal energy density to the transport loss power density

$$\tau_E = \frac{3 n_e k_B T}{P_{trans}} \tag{1.5}$$

n_e represents the electron density and T the temperature.

In the end an expression for n_e and τ is found

$$n_e\tau \geqslant \frac{3k_BT}{\langle\sigma(v)v\rangle E_\alpha/4 - c_BT^{1/2}} =: f(T) \tag{1.6}$$

with $Z_{eff} \equiv 1$ for single ionised atoms and $E_\alpha = 3.5\,\mathrm{MeV}$. The function $f(T)$ is shown in figure 1.2 versus temperature T with a minimum at $T = 27\,\mathrm{keV}$ and $n_e\tau \simeq 1.6 \cdot 10^{20}\,\mathrm{m}^{-3}\,\mathrm{s}$. For a power plant based on magnetic confinement values of

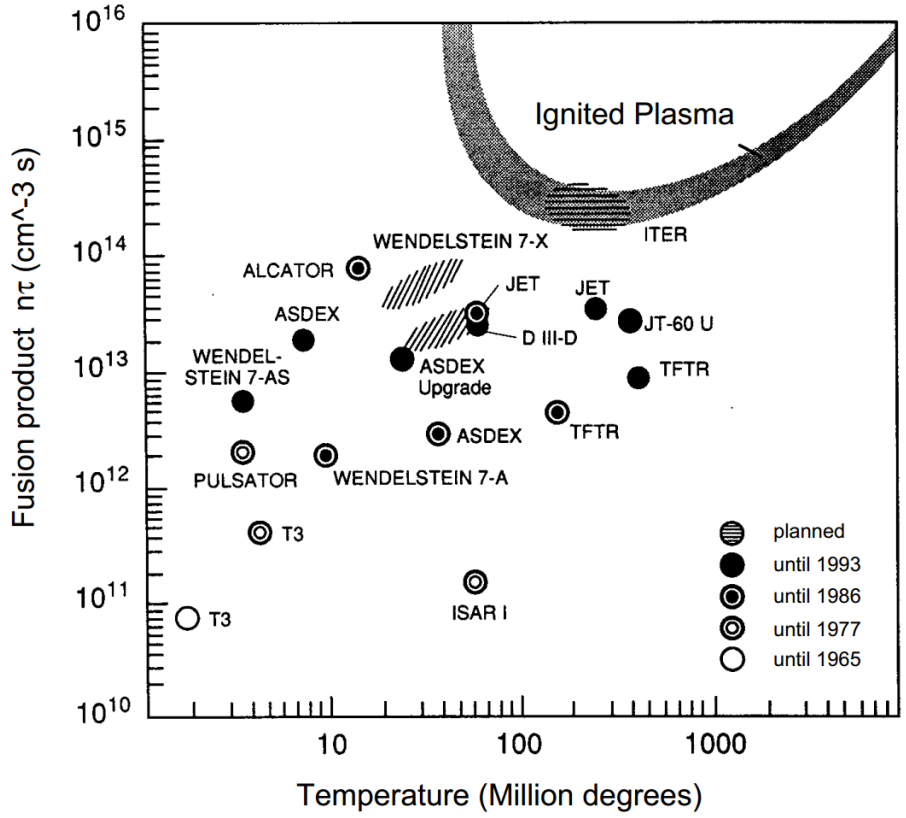

Figure 1.2.: Condition for an ignited – self sustained – plasma according to equation (1.6), [1].

$T \simeq 10\,\mathrm{keV}$, $n_e \simeq 10^{20}\,\mathrm{m}^{-3}$ and $\tau \simeq 5\,\mathrm{s}$ are foreseen.

This overview neglects dilution of the fusion fuel – helium as reaction product is intrinsic – as they increase radiation losses and lower the fuel density.

1.2. Confining a Fusion Plasma

As discussed before, high temperatures are mandatory to obtain fusion, prohibiting direct contact to solid matter as a containment. There are three ways to trap such hot particles: by gravity, as it is done in stars, by inertial fusion, where the fusion fuel is compressed, and by magnetic confinement. Confinement by gravity requires masses only available on stars and comparable celestial bodies. Inertial fusion is mainly researched for military purposes. Magnetic confinement is a promising way to achieve fusion for use in a power plant and is the concept discussed in this work. Before introducing different concepts for magnetic confinement, the basic interactions of charged particles in a plasma with a magnetic field are discussed.

1.2.1. Lorentz Force and Gyration

Charged particles – like ions and electrons – move freely along magnetic field lines, while performing a gyro-motion perpendicular to it. Basis for this is the Lorentz force

$$\boldsymbol{F}_L = q\,\boldsymbol{v} \times \boldsymbol{B} \tag{1.7}$$

with the particle charge q, magnetic field $\boldsymbol{B}$ and velocity $\boldsymbol{v}$.

By separating the velocity into a component perpendicular to the magnetic field

$$\boldsymbol{v}_\perp = \frac{\boldsymbol{B}}{B} \times \left(\boldsymbol{v} \times \frac{\boldsymbol{B}}{B} \right) \tag{1.8}$$

and a parallel velocity

$$\boldsymbol{v}_\parallel = \boldsymbol{v} \cdot \frac{\boldsymbol{B}}{B} \tag{1.9}$$

with

$$\boldsymbol{v}_\parallel \times \boldsymbol{B} = \boldsymbol{0} \tag{1.10}$$

we see that a velocity component along the magnetic field does not result in a force. Comparing the perpendicular velocity with the centripetal force we find

$$F_L = F_Z \tag{1.11}$$

$$qv_\perp B = \frac{mv_\perp^2}{\rho} \tag{1.12}$$

$$qB = \frac{mv_\perp}{\rho} \tag{1.13}$$

with particle mass m and radius ρ. As this force is perpendicular to the motion, no energy is transferred and in a homogeneous field a gyro motion with radius

$$\rho = \frac{mv_\perp}{qB} \tag{1.14}$$

is found. Introducing the circumference $c = 2\pi\rho$ the gyro frequency is defined by

$$\Omega = \frac{v_\perp}{c} = \frac{qB}{2\pi m} \tag{1.15}$$

which is independent of the particles velocity.

The Lorentz force on a charged particle in a homogeneous magnetic field results in a gyro motion perpendicular to the field with superimposed movement parallel to it.

1.2.2. Toroidal Setup and Drifts

The tokamak concept presented in this section was developed in the former Soviet Union in the 1950's. The experimental data for this thesis was obtained at ASDEX (*Axial Symmetric Divertor EXperiment*) Upgrade in Garching, illustrated in figure 1.3, which is a tokamak operated by the Max-Planck-Institute for Plasma Physics (IPP) in Garching near Munich.

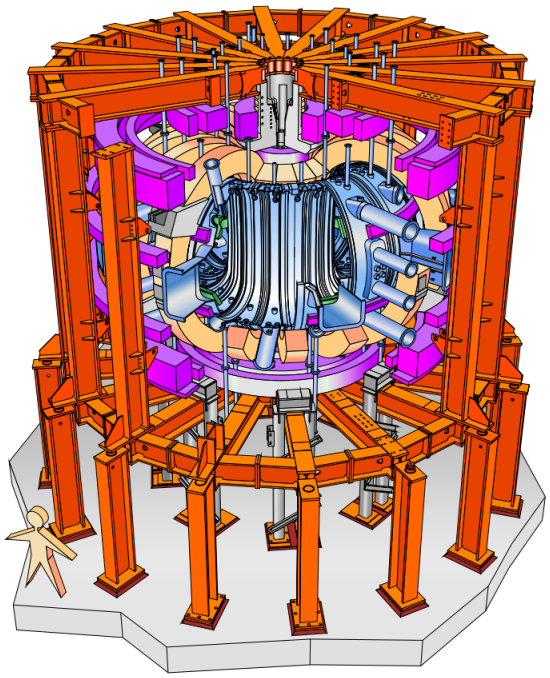

Figure 1.3.: Cut away drawing of ASDEX Upgrade [2].

Drifts in a Toroidal Magnetic Field

A charged particle in a magnetic field gyrates along the magnetic field lines and therefore shows no net perpendicular movement, as discussed above. A magnetic trap for charged particles is build by creating a toroidal magnetic structure, depicted in figure 1.7. A gyrating particle moves around the torus indefinitely, as long as the gyro motion does not intersect the surrounding, also called plasma facing components. Considering the inhomogeneous magnetic conditions – as the distance between the coils increases with the radius – and the interaction of a set of particles reveals new issues. The reason are drifts and the different behaviour of electrons and ions.

For the general case of an external Force $\boldsymbol{F}$ acting on a gyrating particle with charge q the resulting drift velocity is described by:

$$\boldsymbol{v}_F = \frac{\boldsymbol{F} \times \boldsymbol{B}}{q\, B^2} \tag{1.16}$$

Assuming a pure toroidal magnetic field, the gradient of the magnetic field is directed towards the central axis of the torus – $B \propto 1/R$ – resulting in the so called $\nabla \boldsymbol{B}$ drift

$$\boldsymbol{v}_{\nabla \boldsymbol{B}} = \frac{m\boldsymbol{v}_\perp^2}{2} \frac{\boldsymbol{B} \times \nabla \boldsymbol{B}}{qB^3} \tag{1.17}$$

and the curvature drift

$$\boldsymbol{v}_{curv} = m\boldsymbol{v}_\parallel^2 \frac{\boldsymbol{B} \times \nabla \boldsymbol{B}}{qB^3} \tag{1.18}$$

which depend on the charge q of the particle and lead to a charge separation in the vertical direction. Figures 1.4 show the drift motions due to the magnetic field B and its gradient and figure 1.5 the curvature drift parallel to the central axis.

The charge separation resulting from the $\nabla \boldsymbol{B}$ and curvature drift in turn results in an electric field $\boldsymbol{E}$, leading to the $\boldsymbol{E} \times \boldsymbol{B}$-drift. The drift velocity

$$\boldsymbol{v}_{\boldsymbol{E}\times\boldsymbol{B}} = \frac{\boldsymbol{E} \times \boldsymbol{B}}{B^2} \tag{1.19}$$

is independent of the individual charge and mass of the particle. Figure 1.6 shows the orientation of the movement of ions and electrons relative to a magnetic field B and electric field E. Therefore $\boldsymbol{v}_{\boldsymbol{E}\times\boldsymbol{B}}$ is the same for all particles in direction and magnitude, leading to a bulk movement directed outwards in a tokamak. To circumvent this outward motion, the electric field has to be avoided.

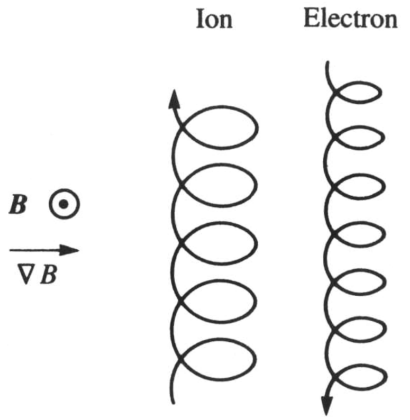

Figure 1.4.: Schematic motion of ions and electrons in a magnetic field $\boldsymbol{B}$ in presence of a gradient ∇B [3].

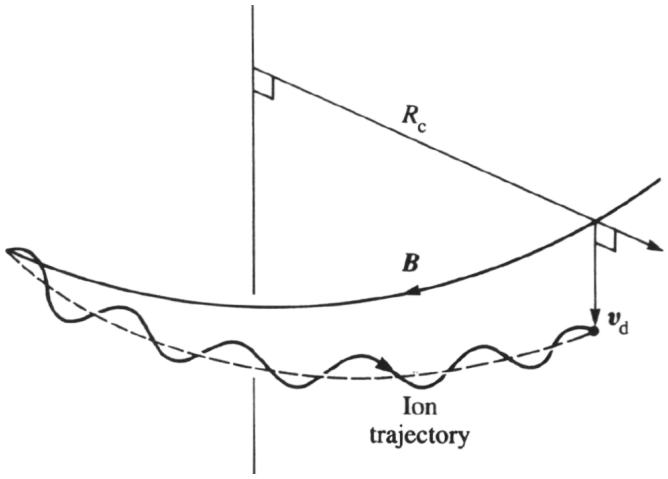

Figure 1.5.: Motion of a captured ion in a static, curved magnetic field [3]. R_C is the radius of curvature and the axial drift speed is denoted by v_d.

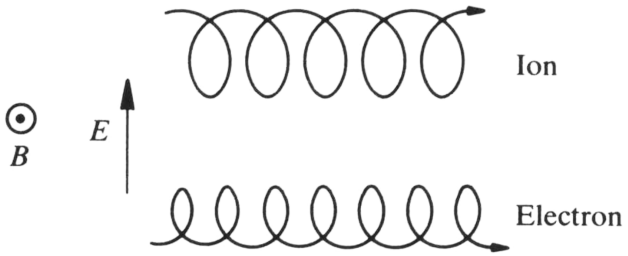

Figure 1.6.: Schematic depicting the $\boldsymbol{E} \times \boldsymbol{B}$ drift motion of ions and electrons in a magnetic field $\boldsymbol{B}$ with additional electric field $\boldsymbol{E}$ [3].

Adding a Poloidal Magnetic Field

A solution to the charge separation is an additional poloidal field, resulting in a helicity of the toroidal magnetic field. The helical twisted magnetic field lines connect the top and bottom of the confined plasma, allowing so called Pfirsch-Schlüter currents to flow, counteracting the charge separation. One possibility to achieve this is to induce a toroidal current inside the plasma. This can be done by installing a solenoid in the centre of the torus, acting as the primary coil of a transformer, the plasma itself acts as the secondary coil, resulting in a toroidal current.

Figure 1.7 shows the basic coil system to realise the described magnetic configuration. The toroidal field coils (blue) for the toroidal field. The central solenoid (green) for the induction of the plasma current. The poloidal field coils (grey) for control of the plasma shape and position. This concept is the so called tokamak.

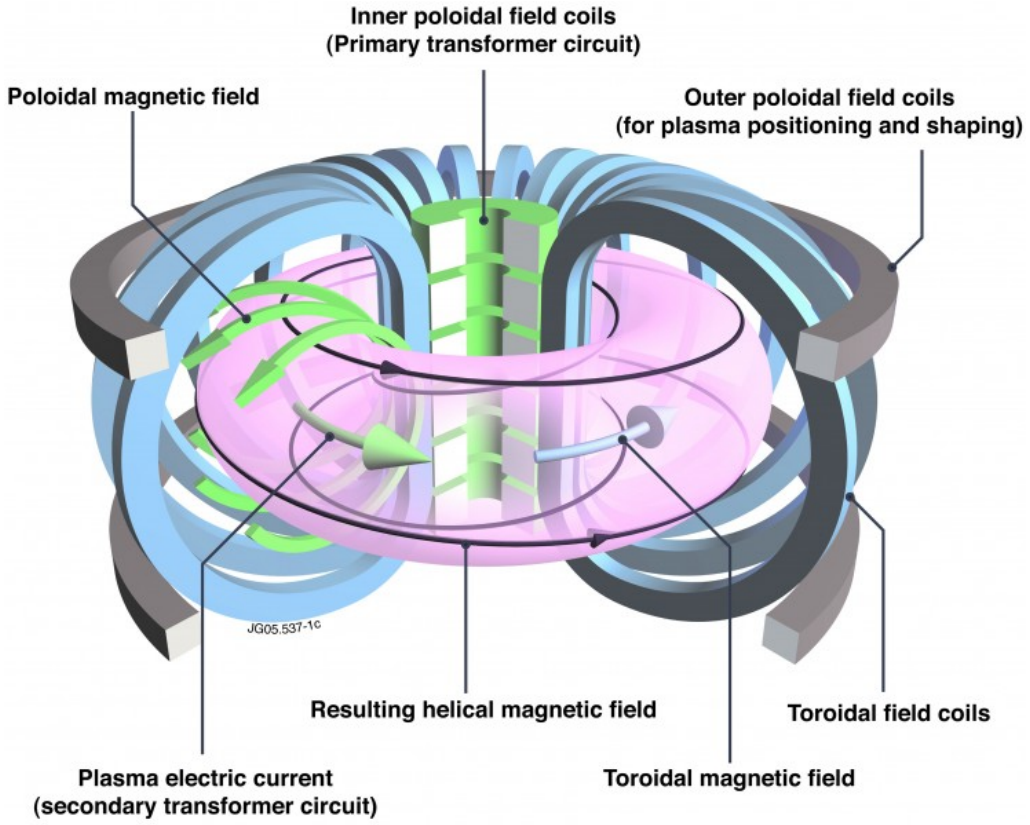

Figure 1.7.: Sketch of the coil system forming a tokamak [4]. Green: central solenoid, blue: toroidal field coils, grey: poloidal field coils.

The current in the central solenoid has to be changed continuously to sustain the plasma current. Therefore this concept allows only pulsed operation, due to the limited current in the central solenoid. One possibility to operate a tokamak in

steady state, is to induce the toroidal plasma current by other means than the central solenoid. The use of auxiliary heating systems is investigated for this purpose [5].

1.2.3. Limiter and Divertor Configuration

It is necessary to extract the ash and impurities from the confined region, as they lead to a high amount of radiation losses – especially for heavy atoms like tungsten – and dilution of the fusion fuel. In the early days of fusion research the so called limiter was used, where the plasma touches the wall in a defined region. Figure 1.8 a) shows the heat shield at the left hand side acting as limiter. The confined area (red) is defined by the so called last closed flux surface ($LCFS$). The area between the confined region and the surrounding wall (orange) is called scrape-off layer (SOL). Main problem of the limiter is the proximity of the wall to the plasma, resulting in a high concentration of impurities in the confined area. This is because particles released from the wall can directly enter the confined plasma.

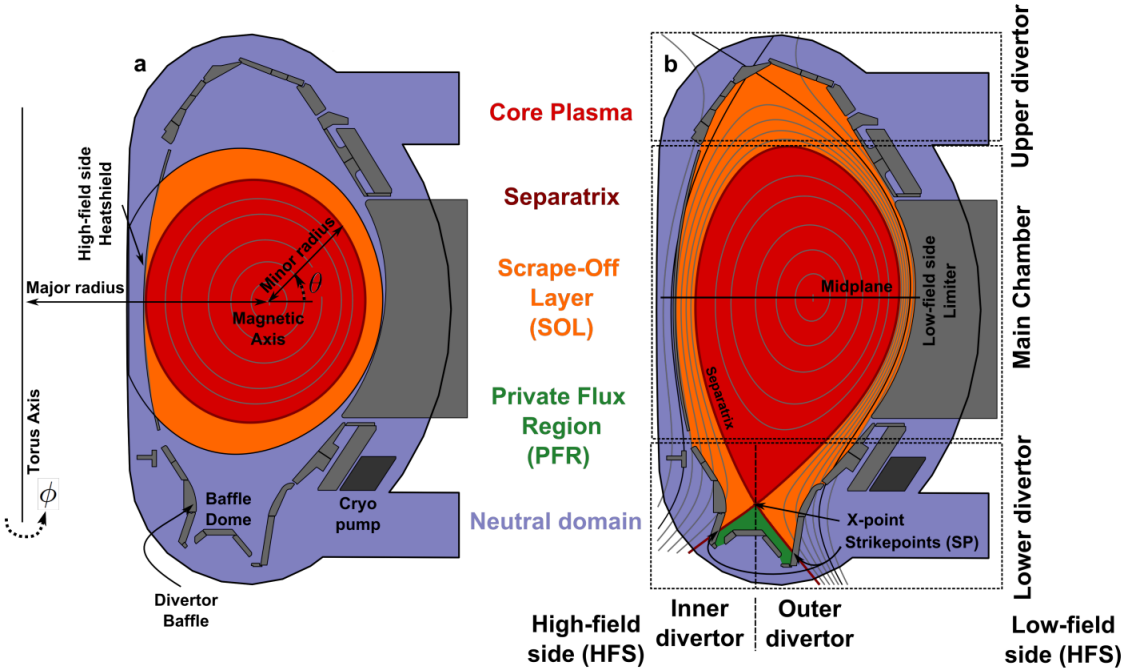

Figure 1.8.: Poloidal cross section for a) limiter geometry and b) divertor geometry [6]. The midplane mp is defined by the magnetic axis in the poloidal cross section for both configurations.

An advanced setup was successfully applied in Garching with ASDEX [7], where two additional coils above and below the torus result in the so called X-points. There the poloidal magnetic field of the plasma current cancels out with the magnetic field

induced by these coils, which carry a current parallel to the plasma current.

Figure 1.8 b) shows a lower single null configuration in ASDEX Upgrade, where only the lower X-point is *active*. The upper X-point is behind the target plates, so the strike points – where the highest heat flux arrives by plasma transport – form only in the bottom of the machine.

Because of the distance between the confined plasma and the target surface, energy can be dissipated by means of radiation and a cushion of neutral particles can form in front of the target, slowing down the incoming particles. Additionally, impurities by sputtering of the target are less likely to reach the core plasma. This will be vital for large fusion devices such as ITER, which is envisaged to produce ten times the fusion power by DT-reactions compared to the auxiliary heating power. The heat flux density parallel to the magnetic field for ITER at the outer midplane can be approximated by the heat crossing the Separatrix $P_{Sep} \simeq 100\,\mathrm{MW}$ divided by the area given by the major radius $R = 6.2\,\mathrm{m}$ and the extent of the SOL [8] $\lambda_q \simeq 1\,\mathrm{mm}$:

$$q_{ITER,\parallel} = \frac{P_{Sep}}{2\pi R \lambda_q} \cdot \frac{1}{\sin(\alpha_{pitch,mp})} \simeq 17\,\mathrm{GW\,m^{-2}} \tag{1.20}$$

$\alpha_{pitch,mp} \simeq 10^\circ$ represents the inclination of the magnetic field lines to the toroidal orientation at the outer midplane (mp). This inclination changes to $\alpha_{pitch,div} \simeq 3^\circ$ in the divertor (div) near the target:

$$q_{ITER,div} = q_{ITER} \cdot \frac{\sin(\alpha_{pitch,mp})}{\sin(\alpha_{pitch,div})} \simeq 60\,\mathrm{GW\,m^{-2}} \tag{1.21}$$

Radiative losses and spreading of the heat have to reduce this heat flux density to around $10\,\mathrm{MW\,m^{-2}}$ at the divertor target, which can be handled by actively cooled components.

Figure 1.9 shows two different configurations for the divertor geometry in ASDEX Upgrade, called *open divertor* (Div I) and *closed divertor* (Div IIa). While the open divertor delivers target surfaces distant to the confined region, the closed divertor in addition supports a higher pressure of neutral particles. This is important for large machines, as the pumping flow is proportional to the particle density [6].

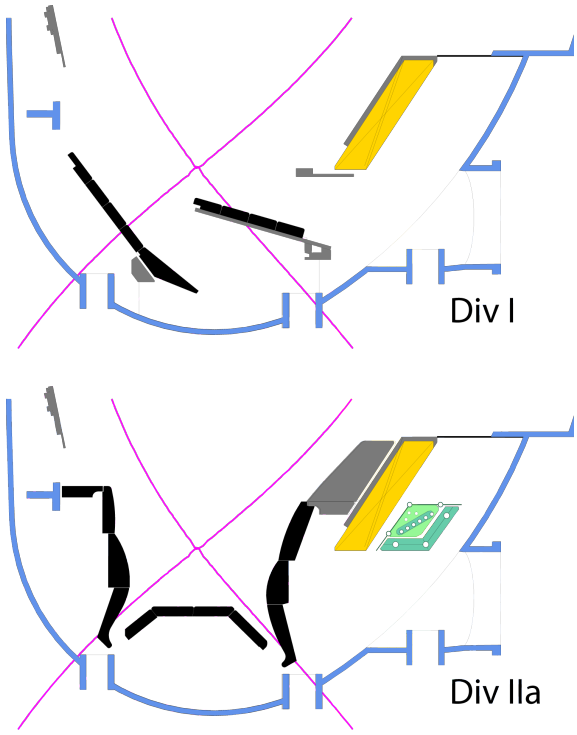

Figure 1.9.: Comparison between two divertor configurations in ASDEX Upgrade [2]. Upper part: *open divertor configuration* of divertor *Div I*. Lower part: *closed divertor configuration* of divertor *Div IIa*.

1.2.4. Heat Flux Profiles

Heat reaching the target plates in the divertor is examined in poloidal heat load profiles. Their peak value and gradient influence the life time of the material. Fluxes of heat and particles degrade the material, spatially and temporally varying heat loads lead to cracking [9]. Predicting and controlling these profiles is necessary in order to design and operate a fusion power plant. Steady state heat loads of several tens and intermittent events with hundreds of $\mathrm{MW\,m^{-2}}$ have been measured in present day devises, usually operating for some seconds [10]. The experimental reactor ITER is therefore designed to handle $10\,\mathrm{MW\,m^{-2}}$ in steady state. A good description for the heat flux profile at the X-point is an exponential with fall-off length λ_q and peak q_0, represented in figure 1.10 as blue line. Spreading the heat lowers the peak heat flux and the gradients. Better understanding of this spreading process is important for the design of future divertors and yields information about the heat transport in the SOL.

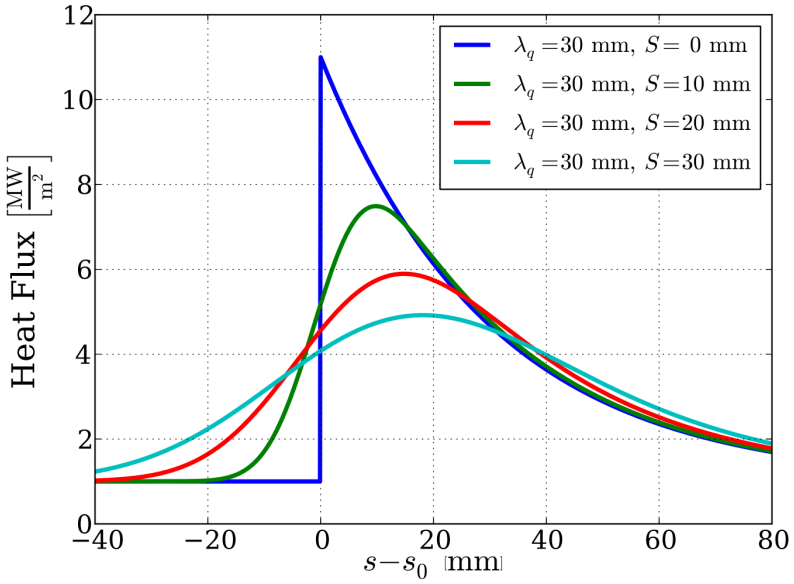

Figure 1.10.: Spreading of the heat flux profile by diffusion from X-point to target for different spreading factors S [11]. The location on the target is called s, with s_0 as position of the initial step – the separatrix. A Background of $1\,\mathrm{MW\,m^{-2}}$ and peak heat flux of $10\,\mathrm{MW\,m^{-2}}$ are used for illustration.

1.3. Scope of this thesis

Chapter two introduces the theory describing the heat transport in the SOL and methods to describe the heat load profile on the target. Conductive transport of heat to the target is introduced and discussed for the parallel and perpendicular orientation with respect to the magnetic field. Better understanding of the transport is necessary, to quantify experimental results and predict the behaviour for future machines. Geometric aspects relevant to this thesis and the used nomenclature are introduced.

Chapter three introduces the geometry used to describe the diffusive transport in the simulation, including boundary and initial conditions. In the end the numerical treatment used in the simulations is explained.

The experimental basis is outlined in chapter four, including infrared thermography and Langmuir probes to deduce target heat load, temperature and density profiles. Data acquire with these diagnostics is the basis for the numerical simulation. The discrepancy between a 1D model and experiments is shown, motivating the performed investigation.

Chapter five is dedicated to the evaluation of the gathered data. Two geometric configurations are compared. The applicability of the two point model is assessed by comparison to the 2D heat diffusion equation, leading to an approximation of the divertor spreading S for target separatrix temperature and parallel heat flux. The point spread function of the divertor to the parallel heat flux profile is analysed. A deviation to the Gaussian described by the 1D model is found. Alternative fit functions are therefore introduced and their applicability is evaluated.

The results are summarised and conclusions are presented in chapter 6.

2.Theory

This chapter is focused on the theoretical background of heat transport models in the scrape off layer (SOL) and resulting heat load patterns on the divertor target. First heat transport in general is introduced, with focus on diffusive transport in the SOL. The chapter continues with the heat flux pattern on the target, resulting from perpendicular heat transport based on diffusive processes. The presentation of the two point model is followed by the geometry and nomenclature used in the remaining parts of this thesis.

2.1. Heat Transport

The following outlines the three basic mechanisms of transferring heat. While radiation is carried by electromagnetic processess, diffusive and convective transport results from particle interaction and movement. Diffusion is able to transfer heat in solids with quasi-static atoms, whereas convection describes moving particles.

Diffusion is found in all phases of matter, where heat is transported by particle collisions, reducing temperature gradients. It is the dominant transport in the SOL in the conduction limited regime, while it can be neglected in the sheath limited regime, where convection dominates.

Convection describes heat flux carried by particle motion. This can build up temperature gradients and can be in equilibrium with diffusive processes. It is dominant in the convection limited regime in the SOL, when a net particle flow carries heat without the presence of a parallel temperature gradient.

Radiation is emitted by several mechanisms, with thermal radiation being the most important in this thesis. Objects with finite temperature radiate *thermal radiation* according to Planck's Law, further explained in section 4.1. Thermal radiation is used to determine the temperature of surfaces, for example the divertor plates.

Other kinds of radiation are line radiation, bremsstrahlung and cyclotron radiation. Bremsstrahlung is dominant in the confined plasma, acting as heat sink. Line radiation is emitted by excited atoms and is dominant in the divertor region. Cyclotron radiation is emitted and absorbed by gyrating,

charged particles. These mechanisms are out of the scope of this thesis and therefore are not further discussed.

2.1.1. Diffusion

Diffusion in general is based on particle interaction on the scale of the average particle distance, leading to a transport of particles or energy in a quasi-static medium. Gradients of quantities like particle density, concentration or temperature are spatially equalised by diffusive processes. Particle transport is used to introduce basic properties, which are then applied to heat diffusion.

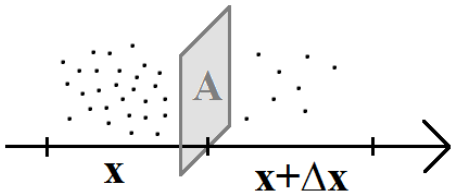

Figure 2.1.: Sketch for particle diffusion used for Fick's Law. In this example the result is a net flux to the right, equalising the particle density.

The flux of particles across an area A, see figure 2.1, can be expressed by the flux of particles from the left to the right minus the flux from the right to the left. Assumption is an unbiased random walk, where particles have the same probability of moving to the left or to the right, with step sizes Δt and step length Δx. The length with extent Δx along the x axis to the left of A is denoted x and the length to the right $x + \Delta x$. In the associated volumes $A \cdot \Delta x$ the particle numbers are denoted $N(x)$ and $N(x + \Delta x)$. The flux through A is found to be

$$J(x,t) = -\frac{1}{2}\left(\frac{N(x+\Delta x,t)}{A\Delta t} - \frac{N(x,t)}{A\Delta t}\right) \tag{2.1}$$

Expanding by the square of the step width $(\Delta x)^2$ and introducing the particle density

$$n(x,t) = \frac{N(x,t)}{V} = \frac{N(x,t)}{\Delta x \cdot A} \tag{2.2}$$

leads to:

$$J(x,t) = -\frac{(\Delta x)^2}{2\Delta t}\left(\frac{n(x+\Delta x,t) - n(x,t)}{\Delta x}\right) \tag{2.3}$$

For infinitesimal step width we find the derivative of n with respect to x on the right hand side and define the diffusivity

$$D = \frac{(\Delta x)^2}{2\Delta t} \tag{2.4}$$

yielding

$$J(x,t) = -D\frac{\partial n(x,t)}{\partial x} \tag{2.5}$$

known as Fick's first law. It can be generalised to more than 1 Dimension by using the corresponding differential operator:

$$\boldsymbol{J}(x,t) = -D\,\nabla n(x,t) \tag{2.6}$$

This derivation is also valid for other quantities like heat instead of particle density. The corresponding solution for the heat flux density is called Fourier's law

$$\boldsymbol{q} = -\kappa \nabla T \tag{2.7}$$

with heat conductivity κ being related to the diffusivity through the specific heat capacity and mass density.

To deduce the specific heat capacity – for point like particles treated as ideal gas with $f = 3$ degrees of freedom – we use

$$c_p = \frac{f+2}{2} \cdot \frac{k_B}{m} = \frac{5}{2}\frac{k_B}{m} \tag{2.8}$$

with the Boltzmann constant

$$k_B = 8.617 \cdot 10^{-5}\,\mathrm{eV\,K^{-1}} \tag{2.9}$$

which will be dropped in further calculations as we will use the energy in eV as unit for the temperature, related by:

$$T[\,\mathrm{eV}] = k_B \cdot T[\,\mathrm{K}] \tag{2.10}$$

This allows to write the product

$$\rho \cdot c_p = \frac{Nm}{V} \cdot \frac{5}{2m} = \frac{5}{2}n \tag{2.11}$$

for each species with its corresponding particle density $n = \frac{N}{V}$. The heat diffusivity is thus linked to the conductivity by

$$\chi = \frac{\kappa}{\rho c_p} \propto \frac{\kappa}{n_e} \tag{2.12}$$

depending on the particle density [12]. As simplification we will drop the pre factor $\frac{5}{2}$ in the further calculations and define the heat diffusivity:

$$\chi \equiv \frac{\kappa}{n_e} \tag{2.13}$$

Applying the continuity equation for the thermal energy to Fourier's Law

$$\nabla q \ + \rho c_p \frac{\partial T}{\partial t} = 0 \tag{2.14}$$

leads to the heat diffusion equation:

$$\frac{\partial T}{\partial t} = \frac{1}{\rho c_p} \nabla \Big(\kappa(T) \nabla T \Big) \tag{2.15}$$

This partial differential equation (PDE) exhibits a non-linearity if κ is a function of T.

This equation is simplified by introduction of the heat potential

$$u := \int_0^T \kappa(T') dT' \tag{2.16}$$

showing the properties

$$\frac{\partial u}{\partial t} = \frac{\partial u}{\partial T} \frac{\partial T}{\partial t} = \kappa \frac{\partial T}{\partial t} \tag{2.17}$$

$$\frac{\partial u}{\partial x} = \frac{\partial u}{\partial T} \frac{\partial T}{\partial x} = \kappa \frac{\partial T}{\partial x} \tag{2.18}$$

$$\frac{\partial^2 u}{\partial^2 x} = \frac{\partial}{\partial x} \left(\kappa \frac{\partial T}{\partial x} \right) \tag{2.19}$$

leading to

$$\boldsymbol{q} = -\nabla u \tag{2.20}$$

and

$$\frac{\partial u}{\partial t} = \chi \Delta u \tag{2.21}$$

Changing the representation of the temperature, we end up with a linear PDE. This is beneficial for numerical codes, as linearity allows to use faster algorithms. It is for example solved in codes like THEODOR (*THermal Energy Onto DivertOR*) [13], calculating the heat flux onto a surface by a measured surface temperature profile and known back side temperature given by a coolant. This formulation of the heat diffusion equation is also applicable to the diffusive transport in the SOL, neglecting other transport channels.

2.1.2. Diffusion Models

We will see that diffusion of heat in plasma is not adequately described by a single model, but especially transport along and perpendicular to the magnetic field differs by several orders of magnitude [1, 3]. Classic diffusion and two empirical scaling laws for perpendicular transport are presented and compared in this section.

Classic Diffusion

Classic diffusion is described by using a kinetic description, introducing a collision operator and calculating associated moments. For a single particle description the distribution function f' describes position and velocity for each particle in the six dimensional phase space. An averaged distribution function f is defined on a mesoscopic volume $\Delta r \Delta v$:

$$f(\boldsymbol{r}, \boldsymbol{v}, t) = \frac{1}{\Delta r \, \Delta v} \int_{\Delta r} \int_{\Delta v} f' \, \mathrm{d}^3 v \, \mathrm{d}^3 r \tag{2.22}$$

The extent of the volume is chosen so that enough particles are contained for f to be independent of microscopic fluctuations, while the volume is small enough to be local with respect to relevant gradients.

The continuity equation applied to the averaged distribution function f results in the so called Vlasov equation

$$\nabla_{\boldsymbol{r},\boldsymbol{v}} \left[(\boldsymbol{v}, \boldsymbol{a}) f \right] + \frac{\partial f}{\partial t} = 0 \tag{2.23}$$

$$\iff f \left(\frac{\partial \boldsymbol{v}}{\partial \boldsymbol{r}} + \frac{\partial \boldsymbol{a}}{\partial \boldsymbol{v}} \right) + \boldsymbol{v} \frac{\partial f}{\partial \boldsymbol{r}} + \boldsymbol{a} \frac{\partial f}{\partial \boldsymbol{v}} + \frac{\partial f}{\partial t} = 0 \tag{2.24}$$

where $\nabla_{\boldsymbol{r},\boldsymbol{v}}$ represents the divergence with respect to location and velocity of the particles. Acceleration $\boldsymbol{a}$ is expressed by force $\boldsymbol{F}$ and particle mass m:

$$\boldsymbol{a} = \frac{\boldsymbol{F}}{m} \tag{2.25}$$

Force $\boldsymbol{F}$ is split into a term containing internal forces $\boldsymbol{F}^{int}$ from within $\Delta r \Delta v$, represented by a collision operator

$$\left.\frac{\partial f}{\partial t}\right|_{coll} \equiv -\boldsymbol{F}^{int} \tag{2.26}$$

and a term describing external forces $\boldsymbol{F}^{ext}$ not included in $\boldsymbol{F}^{int}$, acting at each particle in the volume.

Neglecting internal forces, $\boldsymbol{v}$ and $\boldsymbol{a}$ are expressed by the Hamiltonian equations:

$$\boldsymbol{v} = \frac{\partial H}{\partial \boldsymbol{p}} = \frac{1}{m}\frac{\partial H}{\partial \boldsymbol{v}} \tag{2.27}$$

$$\boldsymbol{a} = \frac{\boldsymbol{F}^{ext}}{m} = -\frac{1}{m}\frac{\partial H}{\partial \boldsymbol{r}} \tag{2.28}$$

Using this expressions, the sum in the first term in equation 2.24 is cancelling:

$$\frac{\partial \boldsymbol{v}}{\partial \boldsymbol{r}} + \frac{\partial \boldsymbol{a}}{\partial \boldsymbol{v}} = \frac{1}{m}\left(\frac{\partial^2 H}{\partial \boldsymbol{r}\partial \boldsymbol{v}} - \frac{\partial^2 H}{\partial \boldsymbol{v}\partial \boldsymbol{r}}\right) = 0 \tag{2.29}$$

The result, taking internal forces by collisions into account, is called Boltzmann equation:

$$\frac{\partial f}{\partial t} + \boldsymbol{v}\frac{\partial f}{\partial \boldsymbol{r}} + \frac{\boldsymbol{F}^{ext}}{m}\frac{\partial f}{\partial \boldsymbol{v}} = \left.\frac{\partial f}{\partial t}\right|_{coll} \tag{2.30}$$

To calculate the heat flux density $\boldsymbol{q}$ we further assume an inhomogeneous ($n = n(\boldsymbol{r})$), stationary (average velocity $\boldsymbol{u} = 0$) plasma and introduce the Bhatnagar–Gross–Krook (BGK) collision operator [14]:

$$\left.\frac{\partial f}{\partial t}\right|_{coll} = -\nu(f - f_0) \tag{2.31}$$

with collision frequency ν, restoring a Maxwellian distribution:

$$f_0 = n(\boldsymbol{r},\boldsymbol{t})\left(\frac{m}{2\pi k_B T(\boldsymbol{r},t)}\right)^{3/2} \exp\left(\frac{m\boldsymbol{v}^2}{2k_B T(\boldsymbol{r},t)}\right) \tag{2.32}$$

The heat flux density $\boldsymbol{q}$ is given as third moment of the distribution function:

$$\boldsymbol{q} = \frac{m}{2} \int (\boldsymbol{v} - \boldsymbol{u})^3 f d^3v \tag{2.33}$$

The result is:

$$\boldsymbol{q} = -\frac{5nk_B^2 T}{2m\nu} \cdot \nabla T \tag{2.34}$$

From comparison to Fourier's law we deduce

$$\kappa = \frac{5nk_B^2 T}{2m\nu} \tag{2.35}$$

as function of collision frequency ν and temperature T. The denominator scales explicit with m, while the collision frequency scales with $\sqrt{\frac{1}{m}}$. For mass dependency we find:

$$\kappa \propto \sqrt{\frac{1}{m}} \tag{2.36}$$

The collision frequencies between same species scales with the temperature given by:

$$\nu_{ee/ii} \propto T_{e/i}^{-3/2} \tag{2.37}$$

Therefore the electron conduction dominates and κ scales with $T^{5/2}$.

Further calculations show

$$\kappa_{\parallel}^{e} = 4.142 \sqrt{\frac{\pi}{2m_e}} \frac{12\pi\epsilon_0^2}{Z^2 \ln\Lambda\, e} T_e^{5/2} \tag{2.38}$$

for the electrons and

$$\kappa_{\parallel}^{i} = 5.53 \sqrt{\frac{\pi}{2m_i}} \frac{12\pi\epsilon_0^2}{Z^4 \ln\Lambda\, e} T_i^{5/2} \tag{2.39}$$

for the ions [15]. The so called Coulomb logarithm $\ln\Lambda$ expresses the dominant small angle scattering by Coulomb collisions of two particles and is larger than one for a tokamak plasma. The ratio

$$\frac{\kappa_{\parallel}^{e}}{\kappa_{\parallel}^{i}} = 0.749 \sqrt{\frac{m_i}{m_e}} \simeq 45 \tag{2.40}$$

shows the dominance of the electron transport, assuming $T_e = T_i$ and deuterium ions.

The parallel transport does not depend on the magnet field, whereas the characteristic

scale for perpendicular diffusion is reduced from the mean free path to the gyro radius. The perpendicular diffusivity is thus expressed by

$$\kappa_\perp = \kappa_\parallel \frac{\nu^2}{\nu^2 + \Omega^2} \tag{2.41}$$

with gyro frequency:

$$\Omega = \frac{qB}{m} \tag{2.42}$$

Applying the introduced quantities shows that the ion transport is dominant in the perpendicular direction, seen in the ratio of

$$\kappa_\perp^e = 6.6\sqrt{\frac{m_e}{\pi}} \frac{\ln\Lambda\, n_e^2 e^3}{12\pi\epsilon_0^2 B^2} T_e^{-1/2} \tag{2.43}$$

and

$$\kappa_\perp^i = 2\sqrt{\frac{m_i}{\pi}} \frac{\ln\Lambda\, n_i^2 e^3}{12\pi\epsilon_0^2 B^2} T_i^{-1/2} \tag{2.44}$$

yielding:

$$\frac{\kappa_\perp^i}{\kappa_\perp^e} = 0.3\sqrt{\frac{m_i}{m_e}} \simeq 18 \tag{2.45}$$

This ratio is based on $T_e = T_i$ and quasi-neutrality $n_e = n_i$ for single ionised particles. The mass of deuterium is used as ion mass.

The equation found for conduction parallel to the magnetic field is called Spitzer-Härm conductivity, describing experiments well with the simplified equation

$$q_\parallel = \kappa_{\parallel,0}\, T^{5/2} \frac{\partial T}{\partial y} \tag{2.46}$$

and constant factor:

$$\kappa_{\parallel,0} \simeq 2000 \frac{\mathrm{W}}{\mathrm{m\,eV}^{7/2}} \tag{2.47}$$

The perpendicular transport coefficients found in experiments are about one order of magnitude larger and scale differently with T and B as compared to classic diffusion, giving rise to the use of empirical scaling laws.

Bohm Diffusion

Bohm Diffusion is an empirical scaling law, introduced in 1949 [16]. It is based on observations of arcs in magnetic fields and describes the perpendicular heat transport

in a tokamak better than the classic calculation [16]:

$$\chi_{\perp,Bohm} = \frac{1}{16}\frac{T}{eB} \propto \frac{T_e}{B} \tag{2.48}$$

Essential are the different scaling behaviours compared to the classic diffusion: a linear increase with temperature instead of a decrease with its square root and only a linear dependence on the inverse magnetic field, instead of a quadratic one. The factor $\frac{1}{16}$ is an approximation introduced by Bohm.

Gyro-Bohm Diffusion

Bohm diffusion was extended at JET to the Gyro-Bohm-Model [17], introducing a new term. It describes a scaling found in JET [18], the largest tokamak in operation today. It introduces the ratio between ion gyro radius $r_g = \frac{mv_\perp}{qB}$ and the length for the typical radial electron temperature gradient $L_{T_e} = \frac{T_e}{|\nabla T_e|}$ as dimensionless scaling factor

$$\chi_{GB} = \alpha\frac{T}{eB}\frac{r_g}{L_{T_e}} \propto \frac{T_e^{3/2}}{B^2} \tag{2.49}$$

where α represents a fitting parameter.

These two empirical models describe the perpendicular transport in a tokamak better than classic diffusion [11].

2.2. Geometric Aspects

This section treats the geometric aspects of field lines in the SOL called flux expansion and pitch angle based on the magnetic conditions in a tokamak.

2.2.1. Flux expansion

The so called flux expansion f_x is a quantity reducing the heat flux onto the divertor (div) compared to the midplane (mp). It is composed of a magnetic and a geometric component.

Figure 2.2 a) shows the magnetic flux expansion $f_{x,mag}$ caused by the geometric properties of the magnetic quadrupole in a X-point configuration with respect to the mid plane. This widens the flux tubes [19] by a factor

$$f_{x,mag}^{div} = \frac{R^{mp}}{R^{div}}\frac{B_{pol}^{mp}}{B_{pol}^{div}} \tag{2.50}$$

in the divertor and thereby alters the target heat flux density. Dependencies are the major radii R^{mp} at the midplane and R^{div} at the divertor and the poloidal magnetic fields B_{pol}^{mp} and B_{pol}^{div} at the corresponding locations. For the ASDEX Upgrade divertor the major radius to the outer strike point $R^{div,o}$ is smaller than the major radius of the outer midplane R^{omp}. For the inward side this relation does not hold, see figure 3.1 a). As the poloidal field is decreasing from midplane to X-point, the flux expansion is larger than one. Towards the target the increasing proximity to the toroidal divertor coil, which is responsible for the magnetic X-point geometry, the poloidal field increases. B_{pol} at the target is lower than at the outer midplane in ASDEX Upgrade, leading to a beneficial flux expansion ($f_{x,mag}^{div} > 1$).

Figure 2.2 b) shows the relative increase of the exposed target width to the fixed width of an incident flux for three incident angles α_{pol} of the magnetic field in the poloidal cross section. This geometric property is used to reduce the heat load on the target and is called geometric flux expansion:

$$f_{x,geo} = \frac{1}{\cos(\alpha_{pol})} \tag{2.51}$$

The product of the introduced expansions

$$f_x = f_{x,mag} \cdot f_{x,geo} \tag{2.52}$$

is around 4 to 6 in ASDEX Upgrade for the outer and around 10 for the inner divertor.

2.2.2. Pitch Angle

As the toroidal magnetic field is superimposed by a poloidal field, the field lines are inclined with respect to the toroidal component. The resulting pitch angle α_{pitch} is defined as

$$\alpha_{pitch} \equiv \arctan\left(\frac{B_{pol}}{B_{tor}}\right) \simeq \frac{B_{pol}}{B_{tor}} \simeq \frac{B_{pol}}{B} \tag{2.53}$$

with the toroidal field component $B_{tor} \gg B_{pol}$. The heat flux density measured on the target – assuming no tilting with respect to the toroidal field – is lower than the heat flux parallel to the field lines:

$$q_t = q_{\parallel} \cdot \frac{\sin(\alpha_{pitch})}{f_{x,geo}} \simeq q_{\parallel} \cdot \frac{\alpha_{pitch}}{f_{x,geo}} \tag{2.54}$$

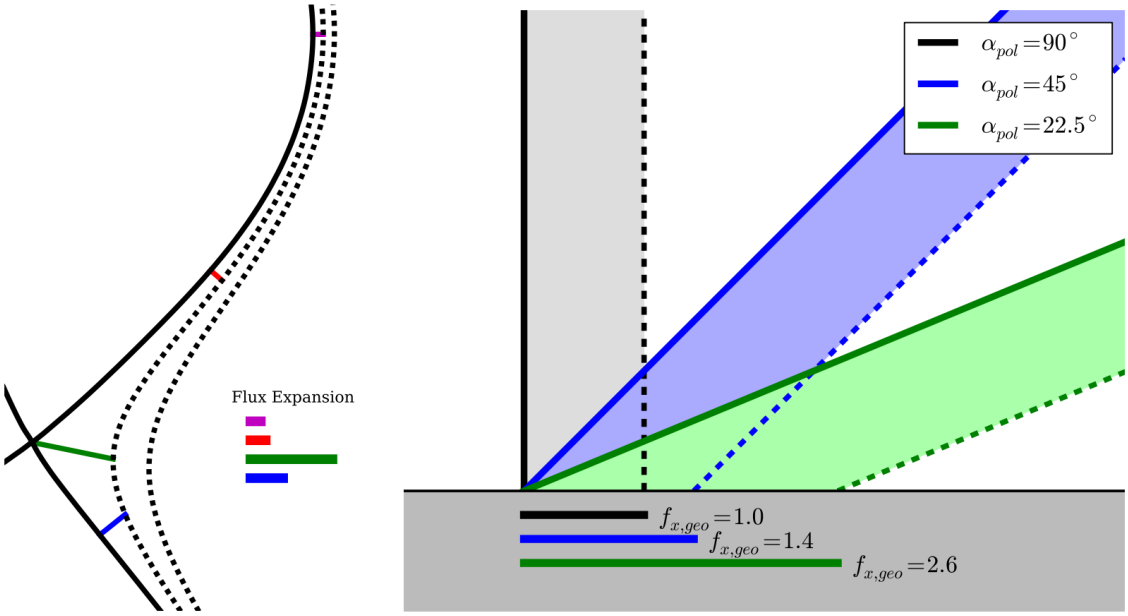

a) Magnetic flux expansion of the flux surfaces in the SOL.

b) Geometric flux expansion for different target inclination angles.

Figure 2.2.: a) magnetic flux expansion, b) geometric flux expansion [11].

At the outer target in ASDEX Upgrade α_{pitch} is around 3° resulting in $\sin(\alpha_{pitch}) \simeq \frac{1}{19}$.

2.2.3. Correlation between α_{pitch} and $f_{x,mag}$

This section explains the correlation between flux expansion and pitch angle at the example of outer midplane (omp) and outer divertor.

Expressing the toroidal field at an arbitrary location in the torus

$$B_{tor} = B_{tor}^{omp} \frac{R^{omp}}{R} \propto \frac{1}{R} \tag{2.55}$$

for B_{tor}^{omp} measured at the outer midplane, the pitch angle is expressed as:

$$\alpha_{pitch} = \frac{R}{R^{omp}} \frac{B_{pol}}{B_{tor}^{omp}} \tag{2.56}$$

The product of magnetic flux expansion and pitch angle is found to be constant:

$$f_{x,mag} \cdot \alpha_{pitch} = \frac{R^{omp}}{R} \frac{B_{pol}^{omp}}{B_{pol}} \cdot \frac{R}{R^{omp}} \frac{B_{pol}}{B_{tor}^{omp}} = \frac{B_{pol}^{omp}}{B_{tor}^{omp}} = \alpha_{pitch}^{omp} \tag{2.57}$$

with the flux expansion being defined as one at the outer midplane.

2.3. Target Heat Flux Pattern

To describe the poloidal heat flux profile on the target based on the profile at the X-point, a diffusive model is used, neglecting convection and dissipation [8]. Assuming conduction in parallel and perpendicular direction, the heat equation is solved for the perpendicular orientation. The solution for the diffusion of a delta function is a Gaussian with width S, depending on the parallel diffusion time τ from X-point to target and the perpendicular diffusion coefficient $\chi_\perp$:

$$S = \sqrt{\chi_\perp \cdot \tau_\parallel} \tag{2.58}$$

Assuming a constant diffusion time for the parallel transport the target profile is described by convolution of the X-point profile with the Gaussian.

The X-point heat flux density profile is described by an exponential with peak value q_0 and decay length λ_q at the midplane with the radial coordinate x:

$$q(x) = q_0 \cdot \exp\left(-\frac{x}{\lambda_q}\right) : x > 0 \tag{2.59}$$

Note that λ_q is expressed as quantity mapped to the midplane for comparing different geometries and machines. The width measured on the target is therefore higher by factor f_x introduced in the previous section. The same applies for the spreading factor S. The target coordinate is called s with separatrix position s_0.

Solution of the convolution in target coordinate s is

$$\begin{aligned} q_\parallel(s) &= \int_0^\infty q_0 \, \exp\left(\frac{-s'}{f_x \lambda_q}\right) \cdot \frac{1}{\sqrt{\pi}\, f_x \, S} \exp\left(-\left(\frac{s'-s}{f_x S}\right)^2\right) \mathrm{d}s' \\ &= \frac{q_0}{2} \exp\left(\left(\frac{S}{2\lambda_q}\right)^2 - \left(\frac{s-s_0}{f_x \lambda_q}\right)\right) \cdot \operatorname{erfc}\left(\frac{S}{2\lambda_q} - \frac{s-s_0}{f_x S}\right) \end{aligned} \tag{2.60}$$

Figure 2.3 shows an exponentially decaying profile in blue ($S = 0$) and the profiles described by convolution with a Gaussian for three values of $S > 0$. The location on the target is called s, with separatrix position s_0. A homogeneous heat flux density offset $q_{off} = 1\,\mathrm{MW\,m^{-2}}$ and a peak heat flux density of the exponential profile $q_0 = 10\,\mathrm{MW\,m^{-2}}$ are used for illustration.

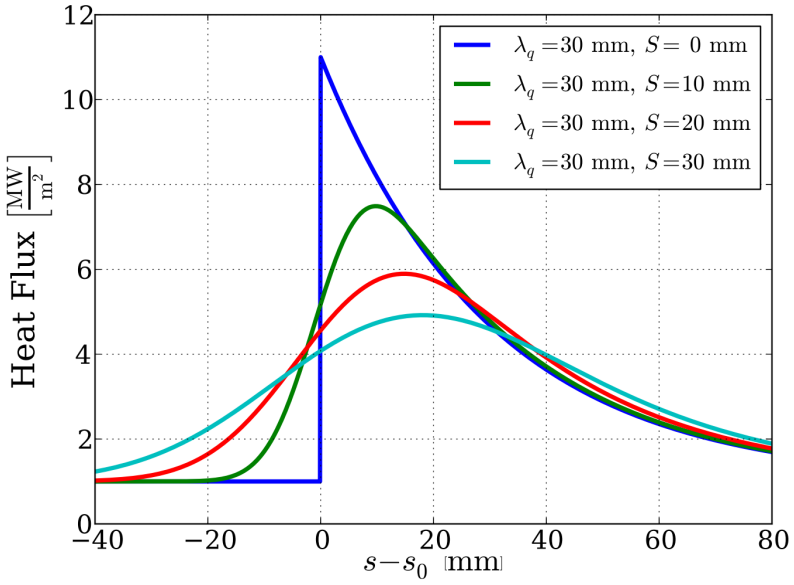

Figure 2.3.: Spreading of an exponential decaying heat flux profile at the X-point to the target by diffusion for different spreading factors S [11].

S is further expressed assuming a constant parallel diffusion time

$$\tau_{\parallel} = \frac{L^2}{\chi_{\parallel}} \tag{2.61}$$

as

$$S \simeq L\sqrt{\frac{\chi_{\perp}}{\chi_{\parallel}}} \tag{2.62}$$

with the length L being measured from X-point to target along a field line.

This is an estimate, as the calculation does not include the geometry and the temperature distribution. The interaction of low and high field side is neglected, though the private flux region connects the inner and outer target. The connection length L is an estimate, as the poloidal field and therefore the pitch angle depends on the radial and poloidal position around the X-point.

Motivation to investigate the heat flux in the divertor region is the engineering limit of heat flux on the target. The integral power decay length

$$\lambda_{int} \equiv \int \frac{q(s)}{\hat{q}} \mathrm{d}s \tag{2.63}$$

describes the distribution of the heat flux density based on the peak heat flux $\hat{q}$, which is relevant for the thermal design. For an exponentially decaying profile without spreading this length is equivalent to the decay length ($\lambda_{int} \equiv \lambda_q$). For the divertor

spreading S described in this section, the benefit on λ_{int} can be approximated [20] by:

$$\lambda_{int} \simeq \lambda_q + 1.64 \cdot S \tag{2.64}$$

The spreading will be vital for ITER, as extrapolations find $\lambda_q \approx 1\,\mathrm{mm}$ [8].

Calculating S for Spitzer-Härm-Like Perpendicular Transport

A more specific expression for S is found, choosing a Spitzer-Härm-like perpendicular conduction with parameter α as temperature dependence:

$$\chi_\perp = \chi_{\perp,0} T^\alpha \tag{2.65}$$

The parallel transport is generalised from the exponent $\frac{5}{2}$ to β:

$$\chi_\parallel = \chi_{\parallel,0} T^\beta \tag{2.66}$$

The ratio of diffusivities then only depends on the temperature, leading to:

$$S = L\sqrt{\frac{\chi_{\perp,0}}{\chi_{\parallel,0}}} \cdot T^{\frac{\alpha-\beta}{2}} \tag{2.67}$$

Case $\alpha = 1$ is identified as Bohm-like temperature dependence, $\alpha = 1.5$ as Gyro-Bohm-like. Note that the exponent in equation (2.67) will be non-positive as the parameter range of interest is restricted to $\alpha \leqslant \beta$. While $\chi_\perp$ is not known in an experiment, it is a defined parameter for the 2D simulation, leaving only T as unknown value to find S. Solving the equation for the temperature and calling it T_S – as it will yield the relevant T for known S – leads to

$$T_S = \left(\left(\frac{S}{L} \right)^2 \cdot \frac{\chi_{\parallel,0}}{\chi_{\perp,0}} \right)^{\frac{1}{\alpha-\beta}} \tag{2.68}$$

for $\alpha \neq \beta$. If $\alpha \equiv \beta$ there is no temperature dependence. For $\alpha < \beta$ the dependence is reduced as α increases.

Approximating teh magnetic field B as a constant in the divertor region, the magnetic field dependence is dropped. Therefore the Spitzer-Härm-like perpendicular transport is analogue to the Bohm and Gyro-Bohm model.

Note the implicit density scaling in $\chi_{\parallel,0}$ and $\chi_{\perp,0}$, expressed by equation (2.13),

leading to:

$$\chi_{\parallel} = \frac{\kappa_{\parallel,0}}{n} T^{\beta} \tag{2.69}$$

$$\chi_{\perp} = \frac{\kappa_{\perp,0}}{n} T^{\alpha} \tag{2.70}$$

As the density cancels in the ratio of diffusivities, no attempt is made to draw conclusion about $S(n)$.

2.4. Simple and Complex SOL

Descriptions for two conditions with distinct properties of the SOL are common, namely the simple SOL and the complex SOL. They are used to describe the sheath-limited and the conduction-limited regime respectively. The simple SOL describes the confined region as the sole particle and heat source. The particles enter the SOL at the *stagnation plane* by perpendicular diffusion, centre of figure 2.4. Their parallel movement is described by a Maxwellian velocity distribution, with parallel mean velocity $u = 0$. No particle or heat sinks and sources are assumed in the SOL, while the target acts as perfect sink. The particles are accelerated by an electric potential drop to the sides, reaching the ion sound speed

$$c_s = \sqrt{\frac{k_B T}{m_i}} \tag{2.71}$$

at the target, according to the Bohm-criterion [15]. The particles keep their thermal

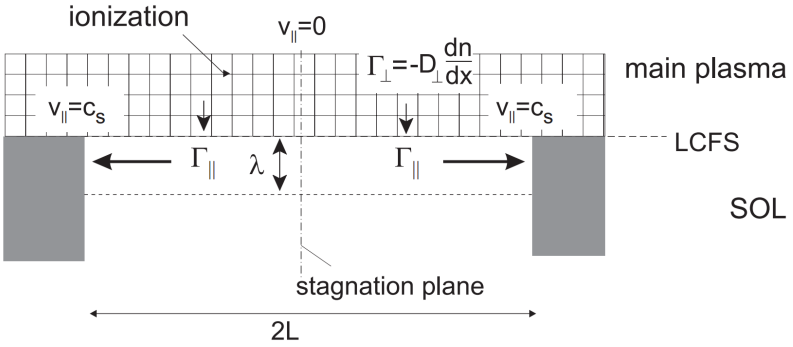

Figure 2.4.: Basic picture of the simple SOL model, showing the confined region of the main plasma as only particle source and the SOL below. Power is conducted from the stagnation plane, at which particles enter the SOL, to the inner and outer targets.

energy until they reach the wall, so the temperature profile is constant and density

reduces from n_0 at the stagnation plane to

$$n_t = n_0/2 \tag{2.72}$$

at the target [15].

Experimental observations are close to this model for mean free path being large compared to the connection length L from stagnation plane – also called upstream – to target – also referred to as downstream. This is found for high temperature and low density in the SOL.

The second description is called complex SOL and assumes a recycling zone near the targets as sole particle source (figure 2.5). Heat diffuses from the main plasma to the SOL and is conducted from the *stagnation plane* to the targets, so a temperature gradient develops as depicted in figure 2.6. This model is further explained in the next section, as the two point model is based on the stagnant SOL condition.

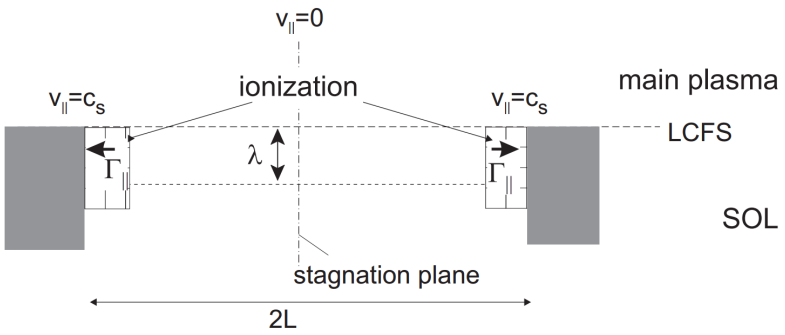

Figure 2.5.: Basic picture of the complex SOL model. Only heat is transported from the main plasma to the SOL at the stagnation plane. Heat is then conducted in the mainly stagnant SOL to the recycling and ionisation region in front of the targets, where particles flows occur.

The conduction limited regime is found for a high density and is therefore also called *high density regime*, where the mean free path is smaller than the extension of the SOL. The temperature gradient is beneficial for the target conditions, delivering lower temperatures in front of the target, allowing dissipation – radiation, ionisation, charge exchange collisions and recombination – processes to lower the heat load to the target.

2.5. Two Point Model

The so called two point model (tpm) describes the temperature and density profile in the SOL along single field lines for a given parallel heat flux $q_\parallel$ [21]. The parallel heat transport is described by Spitzer-Härm conduction for the conduction limited regime. The consequence is a diffusive transport of heat from upstream, where the heat enters the SOL, to the target. No particle flux from upstream to down stream is assumed, as the main particle source is given by recycling – ionisation of neutral particles – in front of the target. This is depicted in figure 2.6. In this case, Fourier's law (equation (2.7)) is integrated in one dimension from target to upstream, yielding:

$$\int_0^L q_\parallel \mathrm{d}l = \kappa_{\parallel,0} \int_0^L T^{5/2}\,\mathrm{d}T = \kappa_{\parallel,0} \int_{T_D}^{T_U} T^{5/2}\mathrm{d}T \tag{2.73}$$

The minus sign from Fourier's law cancels with the negative heat flux, being oriented anti parallel to the integration path. If perpendicular transport and radiation are neglected, the parallel heat flux $q_\parallel$ is constant and the solution of the integral is:

$$T_U = \left(T_D^{7/2} + \frac{7q_\parallel L}{2\kappa_{\parallel,0}}\right)^{2/7} \tag{2.74}$$

T_U and T_D are the temperatures at the upstream and the downstream position respectively. The resulting temperature profile is shown in the conduction region in figure 2.6, where the density assumes pressure conservation along the flux tube. For a sufficiently small downstream temperature the approximation

$$T_U \simeq \left(\frac{7q_\parallel L}{2\kappa_{\parallel,0}}\right)^{2/7} \tag{2.75}$$

can be used. Equation (2.74) is not valid for the divertor region, as the heat flux density profile is degraded by perpendicular diffusion, as introduced in section 2.3. In this case, the heat flux $q_\parallel(l)$ has to be integrated, delivering the correct temperature profile.

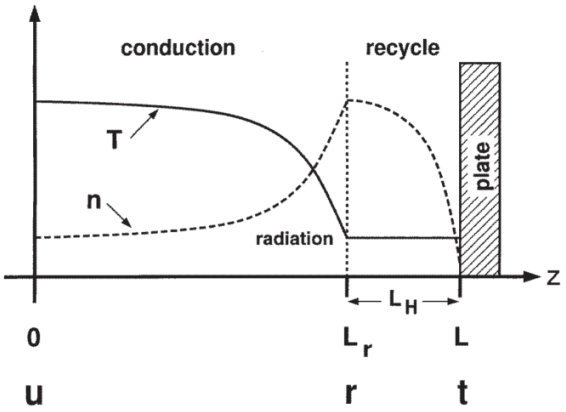

Figure 2.6.: Temperature and density profile in the conduction zone, given by the two point model. Power is conducted from upstream, without convection or particle sources and sinks. The shown recycling zone – not treated in this work – assumes convection to the target with volumetric particle sinks.

2.6. Nomenclature of Common Quantities

This section introduces the nomenclature of quantities used in this work.

The electron and ion temperature can differ in the SOL, but as shown in section 2.1.1 electrons dominate the diffusive heat transport in this region. Thus the electron temperature T_e is the relevant quantity and is addressed with temperature T for simplicity. It is distinguished at different places like the upstream temperature T_U, with the upstream point as defined by the two point model. The temperature at the X-point is called T_X and the target Temperature T_t.

The same applies for the density by assuming quasi neutrality inside the SOL, $Z = 1$ and steady state conditions. We use $n = n_e = n_i$. If we address the density at the target, we write n_t, correspondingly meaning the electron density if not explicitly stated otherwise.

The heat flux q is treated in a similar way, distinguishing between parallel and perpendicular direction as $q_\parallel$ and $q_\perp$. The heat flux onto the target q_t is connected to $q_\parallel$ in front of the target by the pitch angle.

Measurements on the target use target coordinate s, which is connected to the radial upstream coordinate x by the flux expansion f_x. Width measured on the target are mapped to the corresponding upstream width to have a general notation and for comparison to simulations and other devises.

3.Simulation

In this chapter the geometry used in the simulation and the numerical treatment of heat transport in the SOL is discussed. Different configurations and boundary conditions are introduced and the initial conditions used are explained. The code solves the 2D heat diffusion equation for the heat potential

$$\frac{\partial u}{\partial t} = \chi \Delta u \tag{3.1}$$

introduced in section 2.1.1. It is developed to study the target heat flux pattern for different diffusion models and boundary conditions in the divertor region.

3.1. Geometry for Simulations

The geometric setup used in the simulation is the so called *slab geometry*. The actual geometry of the plasma in the machine – shown in figure 3.1 a) – is presented by a simplified sketch in figure 3.1 b). Three areas are distinguished: the confined area *I*, the SOL *II* and the private flux region (PFR) *III*.

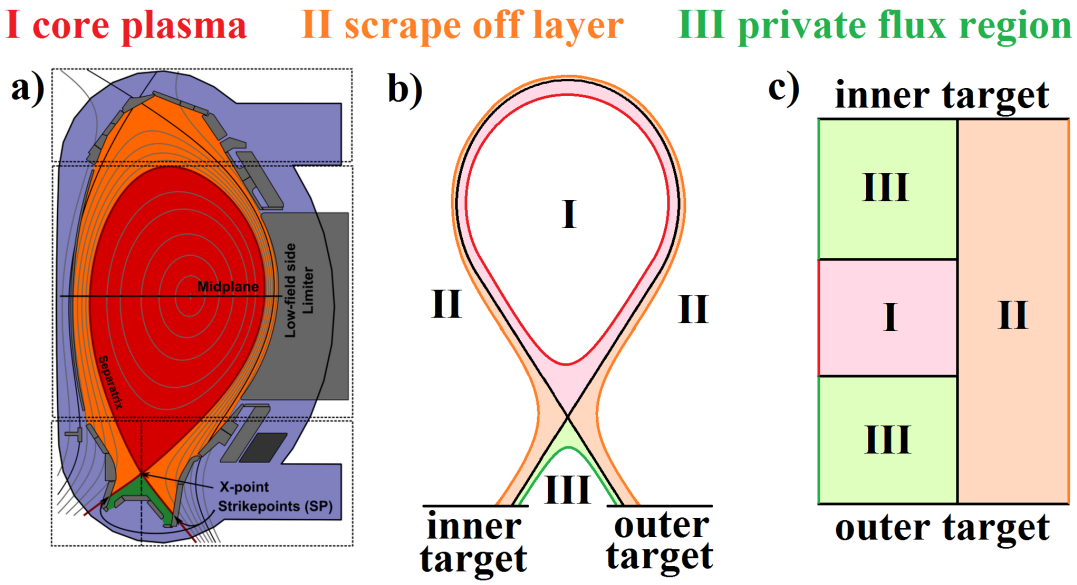

Figure 3.1.: Computational domains in poloidal cross section and slab geometry. a) Actual geometry for Div II-d in ASDEX Upgrade, based on [6]; b) simplified poloidal cross section; c) Slab geometry based on b).

Performing simulations in a 2D grid based on this geometry is an issue, because the

transport mechanisms depend on the orientation of the magnetic field, as shown in section 2.1.2. An orthogonal system is found by straightening the parallel field lines, leading to a configuration shown in figure 3.1 c). The path parallel to the magnetic field lines is called y-axis and the path perpendicular to the field lines x-axis. The slab geometry is a valid approximation to describe an area with small radial extent, as the error due to bending is small. This does not hold for the X-point, as explained later in this section. The SOL from inner target to outer target in ASDEX Upgrade has a connection lengths of around 60 m. The radial extent is in the order of few centimetres. For ASDEX Upgrade the length of the so called divertor leg – the area from X-point to strike line – is 7 m and the length from the X-point to the stagnation plane (section 2.5) for the low field side 20 m. At the high field side the length from X-point to stagnation plane is 26 m, summing up to 60 m from inner to outer target. This length depends on the safety factor

$$q = \frac{rB_{tor}}{RB_{pol}} \tag{3.2}$$

being expressed by the minor radius r, major radius R and the ratio of the toroidal to the poloidal magnetic field, B_{tor} respective B_{pol}. q represents the toroidal turns of a field line to finish one poloidal turn. The average q on a field line allows to approximate the connection length

$$L \simeq \pi R q \tag{3.3}$$

from the stagnation plane to the target.

The computational areas for treating a single target are shown in figure 3.2, where only a part of the plasma is modelled. In the two point model (section 2.5) the upstream plane is the only heat source in the SOL. This assumption is transferred to the slab geometry, neglecting the heat flux from the confined area to the SOL. This mechanism is not described by diffusion but more sophisticated models, for example [22]. A further simplification is to assume a heat flux profile at the height of the X-point and simulate only the divertor region.

The toroidal direction, called z, is not treated in this work, focusing on the poloidal projection of the transport in an axis symmetric system. This is valid if there is no toroidal variation of transport relevant quantities.

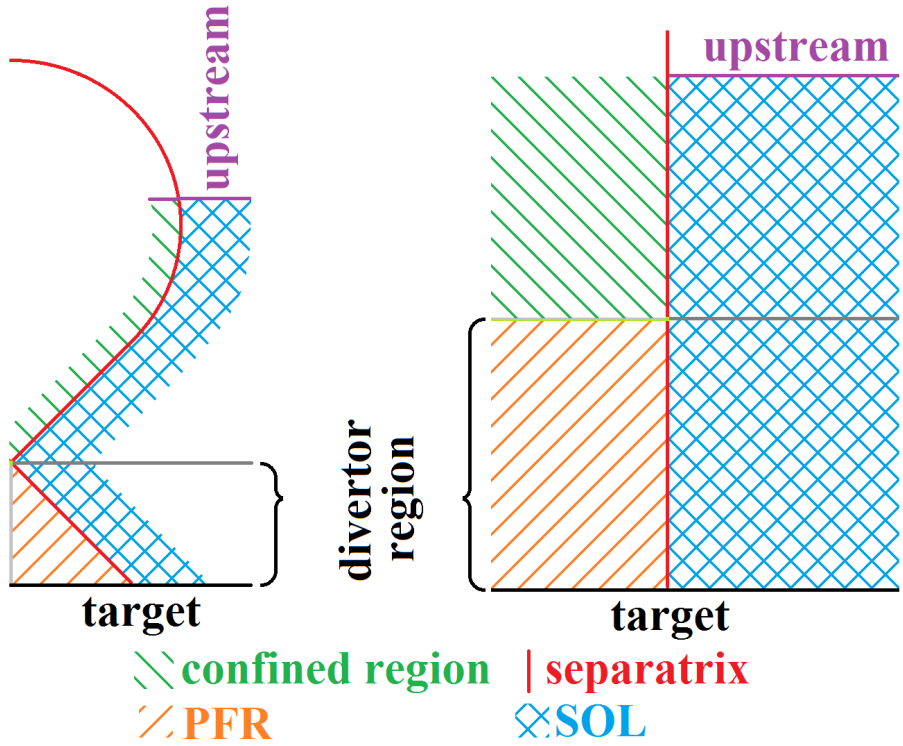

Figure 3.2.: Computational domains in poloidal cross section and slab geometry.

Safety Factor q and Poloidal Projection

A general problem for simulations treating transport around the X-point is the diverging safety factor. It scales with the poloidal magnetic field B_{pol}, which is zero at the X-point by definition. The field line at the X-point is purely toroidal without poloidal component and thus not connected to the surrounding wall. In addition, the applicability of the slab geometry is questionable as the radial distance of field lines scales with the magnetic flux expansion, which also diverges at the X-point:

$$f_m \propto \frac{1}{B_{pol}} \tag{3.4}$$

Projecting the 3D field lines into the 2D poloidal cross section, a transformation from parallel coordinate l to poloidal coordinate y is performed. This is done using the pitch angle introduced in section 2.2.2:

$$\alpha \simeq \frac{B_{pol}}{B_{tor}} \tag{3.5}$$

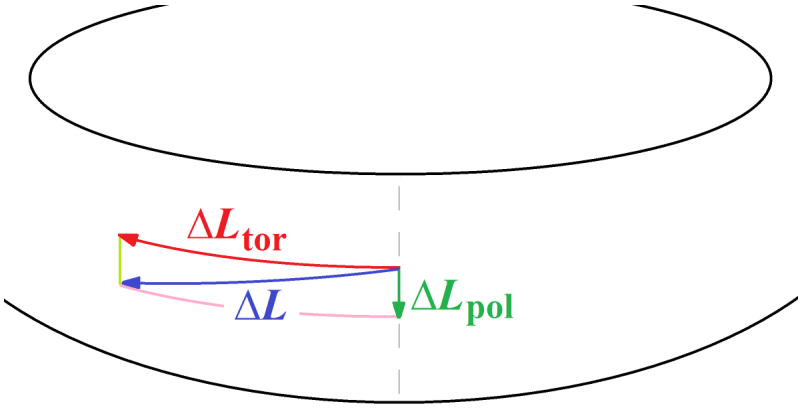

Figure 3.3.: Separation of parallel length L into the poloidal component L_{pol} and the toroidal component L_{tor}.

For a parallel distance ΔL the relation to its projection Δy is

$$\Delta y = \arcsin\alpha \cdot \Delta L \simeq \alpha\,\Delta L \tag{3.6}$$

as depicted in figure 3.3 with $\Delta y \equiv \Delta L_{pol}$. The same applies for the projection of the heat flux:

$$q'_{\parallel} = q_{\parallel} \cdot \alpha \tag{3.7}$$

In the rectangular slab geometry a radial distance Δr is transformed to Δx, by compensating the magnetic flux expansion f_m:

$$\Delta x = \frac{\Delta r}{f_m} \tag{3.8}$$

Note the scaling to the poloidal field:

$$y \propto l\,B_{pol} \tag{3.9}$$

$$x \propto r\,B_{pol} \tag{3.10}$$

$$q'_{\parallel} \propto q_{\parallel} B_{pol} \tag{3.11}$$

The transport coefficients are rescaled according to this transformation, to keep the diffusion time τ between two locations independent of the coordinate system. For a distance ϵ in the 3D geometry small compared to r and R transformed to ϵ' in the

projected slab geometry this is expressed:

$$\tau = \frac{(\epsilon)^2}{\chi} \stackrel{!}{=} \frac{(\epsilon')^2}{\chi'} \tag{3.12}$$

$$\Longleftrightarrow \chi' = \chi \cdot \left(\frac{\epsilon'}{\epsilon}\right)^2 \tag{3.13}$$

Applied to the parallel orientation this yields

$$\chi'_{\parallel} = \chi_{\parallel} \left(\frac{\Delta y}{\Delta l}\right)^2 = \chi_{\parallel} \alpha^2 \tag{3.14}$$

and the perpendicular diffusivity is adjusted to

$$\chi'_{\perp} = \chi_{\perp} \left(\frac{\Delta x}{\Delta r}\right)^2 = \chi_{\perp} \left(\frac{1}{f_m}\right)^2 \tag{3.15}$$

Using relation (2.57)

$$\alpha \cdot f_m = \alpha^{omp} \tag{3.16}$$

the ratio

$$\sqrt{\frac{\chi'_{\perp}}{\chi'_{\parallel}}} = \sqrt{\frac{\chi_{\perp}}{\chi_{\parallel}} \left(\frac{1/f_m}{\alpha}\right)^2} = \sqrt{\frac{\chi_{\perp}}{\chi_{\parallel}}} \left(\frac{1}{\alpha^{omp}}\right) \tag{3.17}$$

is constant in the SOL. The local transport is therefore independent of spatial variations of B_{pol} and R in the simplified geometry.

For a heat flux $\dot{Q}$ through the area given by $\Delta r \cdot \Delta h$ the expression

$$q_{\parallel}(B_{pol}) = \frac{\dot{Q}}{\Delta r \cdot \Delta h} \propto \frac{1}{f_m \cdot \alpha} = \text{const} \tag{3.18}$$

is found. The height Δh of the flux channel, given by the poloidal distance of two field lines, scales with α and the width Δr with f_m. The parallel heat flux density is thus independent of the poloidal field: a higher flux expansion widens the flux channel and lowers the heat flux density, while a smaller pitch angle compresses the field lines and increases the heat flux density.

Keeping the particle density n independent of the projection, the conductivity scales

analogously to the diffusivity:

$$\kappa'_{\parallel} = \frac{\chi'_{\parallel}}{n} = \frac{\chi_{\parallel}}{n}\alpha^2 = \kappa_{\parallel}\,\alpha^2 \tag{3.19}$$

$$\kappa'_{\perp} = \frac{\chi'_{\perp}}{n} = \frac{\chi_{\perp}}{n}\frac{1}{f_m^2} = \kappa_{\perp}\,\frac{1}{f_m^2} \tag{3.20}$$

For the parallel orientation and Spitzer-Härm conductivity the transformation yields

$$\frac{\mathrm{d}T}{\mathrm{d}l} = -\frac{q_{\parallel}}{\kappa_{\parallel,0}T^{5/2}} \tag{3.21}$$

$$\iff \frac{\mathrm{d}T}{\mathrm{d}y}\alpha = -\frac{q'_{\parallel}/\alpha}{\kappa'_{\parallel,0}/\alpha^2 \cdot T^{5/2}} = -\frac{q'_{\parallel}}{\kappa'_{\parallel,0}T^{5/2}}\alpha \tag{3.22}$$

$$\iff \frac{\mathrm{d}T}{\mathrm{d}y} = -\frac{q'_{\parallel}}{\kappa'_{\parallel,0}T^{5/2}} \tag{3.23}$$

For the perpendicular orientation the calculation is analogue. The temperature gradient is described correctly within the 2D slab geometry and the rescaled diffusivities.

Using the rectangular slab geometry and neglecting the scaling of the diffusivities with B_{pol} results in a calculation independent of the actual machine geometry. While the ratio of the perpendicular to the parallel transport, characteristic for the spreading S, is unchanged, the temperature profile is not described correctly. This error is estimated by using Fourier's Law

$$\frac{\mathrm{d}T}{\mathrm{d}y} = -\frac{q'_{\parallel}}{\kappa'_{\parallel,0}T^{5/2}} \tag{3.24}$$

and replacing $\kappa'_{\parallel,0}$ with $\kappa_{\parallel,0}/\alpha^2$:

$$\frac{\mathrm{d}T}{\mathrm{d}y} = -\frac{q'_{\parallel}}{\kappa_{\parallel,0}T^{5/2}}\alpha^2 \tag{3.25}$$

The gradient therefore scales with α^2, implying large errors near the X-point. The relative error for the integrated profile is smaller due to the temperature dependence of the conductivity:

$$T(Y+\Delta Y) = \left(T(Y)^{7/2} - \frac{7q'_{\parallel}\Delta Y}{2\kappa_{\parallel}}\alpha^2\right)^{2/7} \tag{3.26}$$

The analogue is valid for the perpendicular direction. The underestimated parallel and radial gradients do not change the local transport, as both scale with B_{pol}.

Mapping the actual poloidal field of an experiment to the slab geometry and calculating the spatial correction for the diffusivities is possible, but not used in this thesis.

3.2. Geometric Configurations

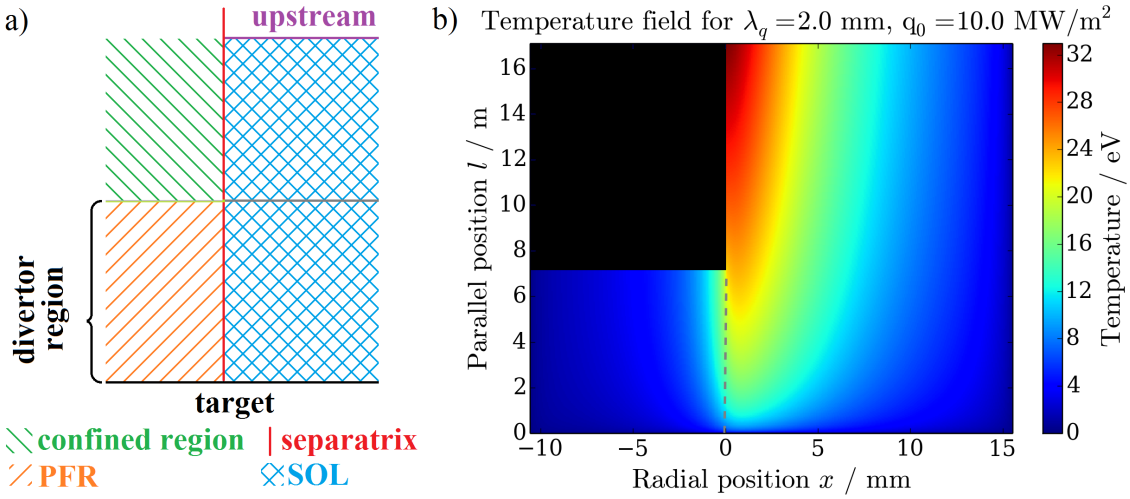

Figure 3.4.: a) Sketch of the orthogonal slab geometry. b) Computational grid and steady state temperature field for $q_{\parallel} = 1\,\mathrm{MW\,m^{-2}}$, $\lambda_q = 2\,\mathrm{mm}$. The dotted line marks the separatrix. The temperature at the target is set to $T_t = 0\,\mathrm{eV}$. The heat flux from the confined area – where no calculations are performed – to the SOL is set to zero.

Figure 3.4 shows a comparison between the structure of the slab geometry and the computational grid with a steady state temperature field. A column of the array represents the path along the magnetic field, a row represents the direction perpendicular to it. The divertor target is at the bottom and the confined region is shown as black block, as it is excluded from the calculations. Upstream – at the top – an exponentially decaying heat flux density in x-direction is used as boundary condition. Downstream a fixed temperature $T_t = 0$ is applied. It is assumed that no heat crosses the separatrix between SOL and confined region. For the example shown the length of the divertor leg is set to 7 m – based on ASDEX Upgrade – and towards the midplane it is 10 m.

Drawback of including the area above the X-point is the flattening of the radial heat flux profile towards the X-point by perpendicular diffusion. This leads to an decrease of q_0 and an increase of λ_q according to the fit at the target with respect to the upstream boundary condition. This is further analysed in section 5.1. Figure 3.5

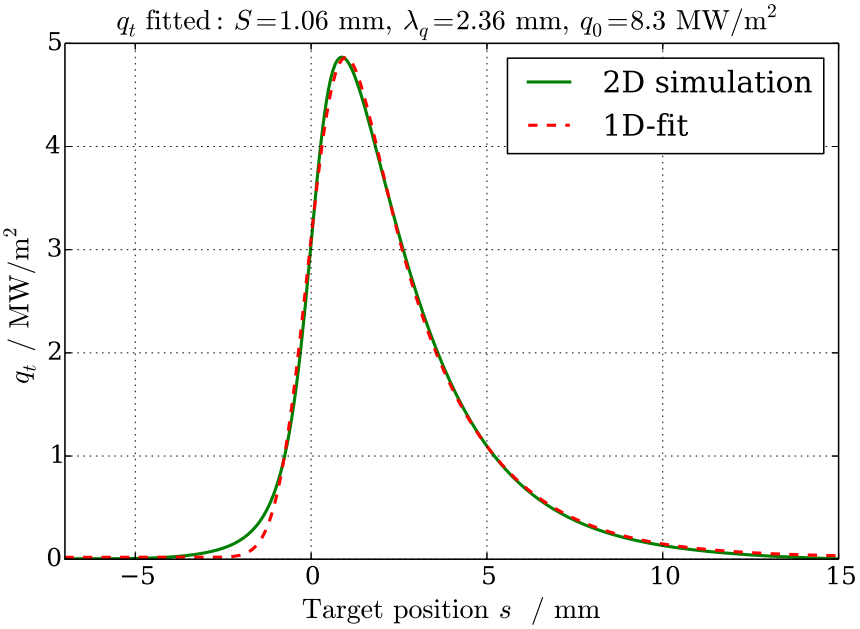

Figure 3.5.: Target heat flux profile for temperature field shown in figure 3.4. The geometry used includes 10 m of SOL above X-point.

shows the resulting heat flux density profile at the target with the 1D fit function applied. According to the fit λ_q widened from 2.00 mm upstream to 2.36 mm at the X-point. The further spreading below the X-point is described by S. The fit value $q_{0,fit} = 8.3\,\mathrm{MW\,m^{-2}}$ is below the upstream boundary condition of $q_0 = 10\,\mathrm{MW\,m^{-2}}$. This is explained by the perpendicular transport above the X-point and energy conservation. For an exponential decay the integrated heat flux equals:

$$\int_0^\infty q(x)\mathrm{d}x = \int_0^\infty q_0 \exp\left(\frac{-x}{\lambda_q}\right)\mathrm{d}x = q_0 \cdot \lambda_q \tag{3.27}$$

In the shown example the peak heat flux at the X-point described by the 1D model is

$$q_{0,X} = 10\,\mathrm{MW\,m^{-2}} \cdot \frac{2.00\mathrm{mm}}{2.36\mathrm{mm}} \simeq 8.5\,\mathrm{MW\,m^{-2}} \tag{3.28}$$

being in agreement with the fit value of $q_{0,fit} = 8.3\,\mathrm{MW\,m^{-2}}$.

The geometry most often used in this work reaches from the X-point to the outer target, including the SOL and PFR. Figure 3.6 shows this grid, with the X-point located at the top. This geometry is called divertor configuration. Figure 3.7 shows a characteristic heat flux profile at the target for this configuration. λ_q is set to 2.4 mm and $q_0 = 8.5\,\mathrm{MW\,m^{-2}}$, for comparison to figure 3.5. This behaviour is further

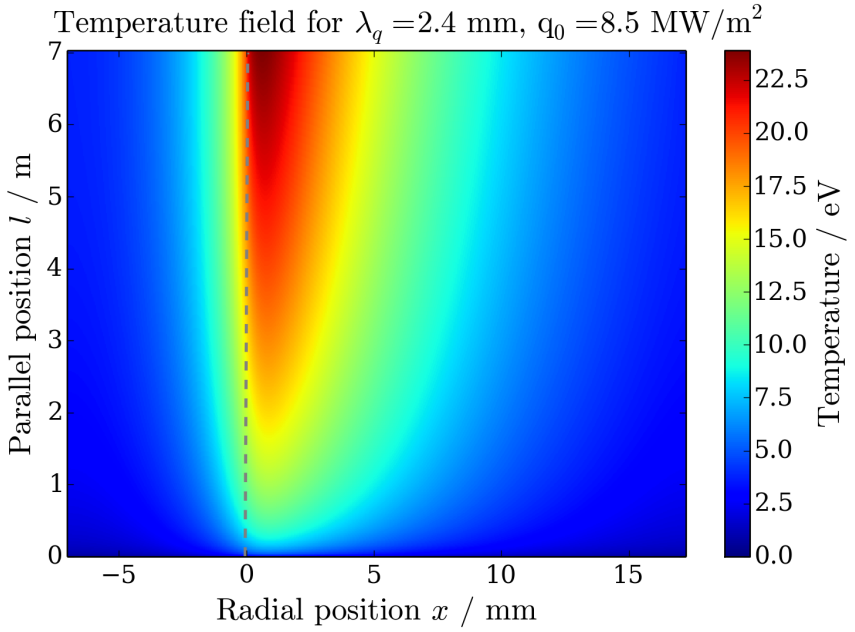

Figure 3.6.: Temperature field for parallel area from X-point – at the top – to the target – at the bottom. Parameters are $q_0 = 8.5\,\mathrm{MW\,m^{-2}}$, $\lambda_q = 2.4\,\mathrm{mm}$. The dotted line marks the separatrix. The target temperature is set to $T_t = 0\,\mathrm{eV}$.

analysed in section 5.1.

Comparing the two heat flux density profiles (figures 3.5 and 3.7) shows a similar deviation from the 1D model. Both simulations used the exponent $\alpha = 1$ for the scaling of the perpendicular diffusivity

$$\chi_\perp = \frac{\kappa_{\perp,0}}{n} T^\alpha \tag{3.29}$$

resembling Bohm diffusion as perpendicular transport mechanism. The values found by fitting the resulting heat flux pattern of the divertor configuration resemble the heat flux decay length and peak heat flux set at the X-point. This behaviour found for the divertor configuration is beneficial for parameter studies and thus used for most simulations.

Further differences between the two configurations are presented and discussed in section 5.1.

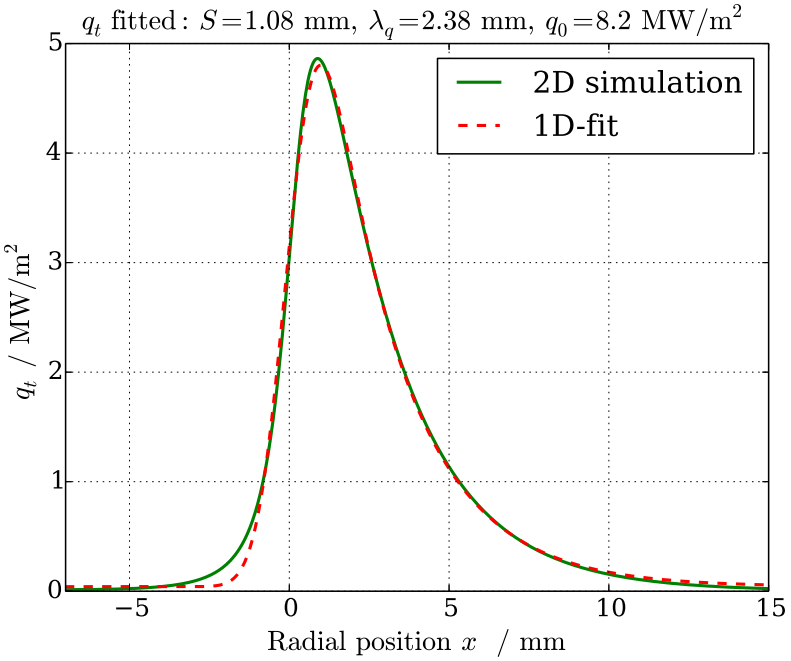

Figure 3.7.: Target heat flux profile for temperature field shown in figure 3.6. The divertor configuration is used.

3.3. Boundary Conditions

The boundary conditions at different locations can either be set to a heat flux or temperature.

The target temperature is set to a fixed constant value or a static profile for most simulations. An additional condition to vary the temperature at the target depending on the incident heat flux is implemented, as described at the end of this section.

The heat flux at the X-point – respective upstream if included in the geometry – is fixed according to an exponential decay:

$$q_{\parallel}(x) = q_0 \cdot \exp\left(-\frac{x}{\lambda_q}\right) \; \forall \; x > 0 \tag{3.30}$$

x denotes the radial coordinate in the slab geometry. For the divertor geometry this boundary condition implies no heat flux between inner and outer PFR.

Preferred boundary condition for the most inner and outer field line is to set the perpendicular heat flux to zero. An alternative is to fix the temperature to an approximated value, allowing to use the perpendicular loss of heat to quantify the influence and thus validate the applicability of the chosen width of the simulation area.

An educated guess is made by taking the fall-off widths of the heat flux in the SOL and PFR into account. The parallel heat flux density at the height of the X-point reduces to $10^{-3} \cdot q_0$ for a width of the SOL of 7 times the heat flux decay length λ_q at the X-point. The spreading of the heat flux is taken into account by weighting S less strong than λ_q, due to the squared argument in the exponential of the Gaussian. The width of the SOL is thus set to

$$w_{SOL} = \sqrt{(3.5S)^2 + (7\lambda_q)^2} \tag{3.31}$$

and the width of the PFR to:

$$w_{PFR} = \sqrt{(5S)^2 + (2\lambda_q)^2} \tag{3.32}$$

For the PFR the weight of S is chosen larger and an offset with respect to λ_q is added, as S is deduced by an empirical approximation and the 1D model underestimates the heat flux density in the PFR.

Depending on the geometric configuration and constraints for a specific simulation the values presented are varied, based on sensitivity studies.

Varying the Target Temperature depending on the Heat Flux Density

In addition to the previously discussed fixed boundary conditions a heat flux dependent variant for the target temperature is implemented. According to sheath theory [23] the heat flux density through the sheath to the target is described by

$$q_S = \Gamma_e \, \gamma \, T_e \tag{3.33}$$

for electron flux density Γ_e, sheath heat transmission factor γ and electron temperature T_e. For a given heat flux to the target, the temperature adjusts itself to fulfil this condition. Applying this condition demands to know the electron density profile, as the particle flux

$$\Gamma_e = c_s n_e \tag{3.34}$$

depends on it. The ion sound velocity at the sheath is described by the Bohm criterion:

$$c_s \geqslant \sqrt{\frac{Z\,T_e + \gamma_i T_i}{m_i}} \simeq \sqrt{\frac{T_e}{m_i}} \propto T_e^{1/2} \tag{3.35}$$

Assuming a constant pressure the relation

$$p = nT \tag{3.36}$$

$$\Longleftrightarrow n = \frac{p}{T} \tag{3.37}$$

is used, resulting in the scaling

$$q_S \propto T_e^{1/2} \tag{3.38}$$

respective:

$$T_e \propto q_S^2 \tag{3.39}$$

The pressure in the simulation is set as radial profile, assuming pressure conservation along field lines.

As first proxy in the simulation the temperature is related to q with

$$T = q \cdot \eta + T_0 \tag{3.40}$$

for a constant factor η and an offset temperature T_0.

Convergence is achieved, with around 50 to 100% additional computation time. Figure 3.8 shows the heat flux density for an offset temperature of $T_0 = 5\,\mathrm{eV}$ and an aim peak temperature of $\hat{T} = 10\,\mathrm{eV}$. For comparison the profile for the same parameters except the constant target temperature $T_t \equiv 0$ is shown as green, dashed line. The divertor spreading increases at about 25% (0.99 mm to 1.23 mm) by increasing the peak target temperature. As a consequence the peak heat flux density is lower, while the shape of the profile is described by the 1D function with the deviation in the PFR similar to the cases with $T_t = 0$. A peaked temperature profile in all assessed cases increases S, in contrast to a pure constant offset. Note that the X-point temperature for $q_0 = 1\,\mathrm{MW\,m^{-2}}$ is around 15 eV according to the two point model, therefore the temperature parameters in the example shown are a large perturbation.

The temperature profile found in experiments can be characterised by applying the 1D fit function, delivering an analogue fall-off length and spreading factor. This values are usually larger than for the heat flux density. A more detailed implementation of the sheath condition is expected to yield temperature profiles as benchmark to other codes.

Using a target temperature profile obtained by Langmuir probes at JET and setting the determined q_0 and λ_q as boundary conditions at the X-point does not reproduce

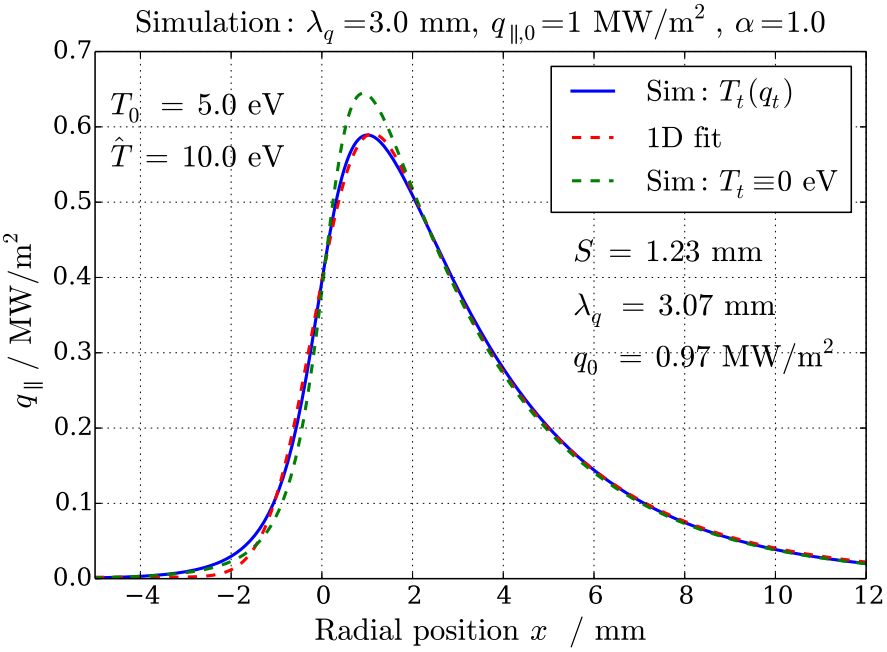

Figure 3.8.: Target heat flux density profile for the target temperature set to a profile scaling with the incoming heat flux and the 1D fit function. For comparison the target heat flux for equivalent simulation parameters except $T_t \equiv 0$ is shown.

the measured heat flux profile. It is found that the simulation is sensitive to a lateral offset of tenth of millimetres of the temperature profile described with λ_T, S_T and T_0. In addition, the heat flux deduced from Langmuir probes and IR measurements deviates.

3.4. Initial Conditions

It is found that the heat flux density profile at the target described by the 1D model

$$q_\parallel(x) = \frac{q_0}{2} \exp\left(\left(\frac{S}{2\lambda_q}\right)^2 - \left(\frac{x}{\lambda_q}\right)\right) \cdot \operatorname{erfc}\left(\frac{S}{2\lambda_q} - \frac{x}{S}\right) \tag{3.41}$$

with x the radial coordinate in the slab geometry with respect to the separatrix, serves well as initial condition for the temperature field for given λ_q and an approximated S. The initial temperature field is calculated from a given target temperature profile towards upstream. Based on the two point model (section 2.5) for

$$\kappa = \kappa_0 \cdot T^\beta \tag{3.42}$$

and constant heat flux $q_\parallel$ between location y and $y + \Delta y$

$$T(y + \Delta y) = \left(T(y)^{\beta+1} + (\beta + 1)\frac{q_\parallel \Delta y}{\kappa_{\parallel,0}} \right)^{\frac{1}{\beta+1}} \tag{3.43}$$

is found. $\beta + 1$ resembles the ratio $\frac{7}{2}$ for Spitzer-Härm conduction. y is measured from the target to upstream.

The 1D model yields $q(x)$ for a given λ_q, q_0 and S. Knowing

$$S = L\sqrt{\frac{\chi_\perp}{\chi_\parallel}} \tag{3.44}$$

a linear dependence from S to the parallel distance to the X-point $(L - y)$ is assumed

$$S'(y) = \frac{L - y}{L} \cdot S \tag{3.45}$$

to approximate $q_\parallel(x, y)$. The temperature at position (x, y) is expressed by:

$$T(x, y + \Delta y) = \left(T(x, y)^{\beta+1} + (\beta + 1)\frac{\Delta y \cdot q(x, y)}{\kappa_{\parallel,0}} \right)^{\frac{1}{\beta+1}} \tag{3.46}$$

For boundary condition $T_t \equiv 0$ temperatures in front of the target are small and with it the conductivity. The computational time to reach equilibrium is increased if S is estimated too low a priory for the method explained. A solution is to add an artificial heat flux, being small compared to q_0, to $q_\parallel$:

$$\hat{q}(y) = q_{0,\parallel} \cdot 10^{-3} \cdot \left(\frac{L - y}{L} \right)^{10} \tag{3.47}$$

Defining the relative distance to the X-point, respective the proximity to the target, as

$$d = \frac{L - y}{L} \tag{3.48}$$

the resulting heat flux density is described by:

$$q'(x, y) = q(x, y) + q_{0,\parallel} \cdot 10^{-3} \cdot d^{10} \tag{3.49}$$

Result is a steeper gradient in front of the target, mitigating the error made due to the approximated S. The effect to the temperature profile along a field line is

negligible, due to the temperature dependent conductivity and the fast decay of the offset.

3.5. Numerical Treatment

In the following section the numerical treatment of the heat diffusion equation is discussed in a comprehensive way, as the simulations are a central point for this thesis. The discretisation scheme and the solution method used for the numerical computation are shown. Boundary conditions and their implementation are explained.

3.5.1. Discretisation

To solve the heat equation

$$\frac{\partial u}{\partial t} = \chi \Delta u \tag{3.50}$$

as presented in section 2.1.1 numerically, a discrete system has to be used. Reason is the representation of the temperature field as 2D array whose elements are updated by solving the given equation with discrete time steps. We use the slab geometry as rectangular representation of the original curved system, allowing to use an orthogonal 2D grid. There one direction is oriented parallel and the other one perpendicular to the magnetic field. We write equation (3.50) accordingly:

$$\frac{\partial u}{\partial t} = \chi_{\parallel} \frac{\partial^2 u}{\partial y^2} + \chi_{\perp} \frac{\partial^2 u}{\partial x^2} \tag{3.51}$$

In the following discretisation schemes we denote the position along the y-axis with discretisation Δy as subscript $i \in [1, M]$ and $y = y_0 + i\Delta y$ and analogue with index $j \in [1, N]$ for the x-axis. The time step is denoted with superscript k and step width Δt:

$$t^k = t^0 + k \cdot \Delta t \tag{3.52}$$

3.5.2. Euler Explicit

Euler's forward method is an example for an explicit discretisation method. Giving the equation for the derivative of quantity u with initial value $u(t_0) = u_0$

$$u'(t) = f(u, t) \tag{3.53}$$

the temporal evolution of u is approximated within the discretisation scheme. For known u_i^k the unknown u_i^{k+1} is approximated by applying the derivative during the time step Δt:

$$u_i^{k+1} = u_i^k + \Delta t\, f(t^k, u_i^k) \tag{3.54}$$

which is exact, if the derivative is constant during the time step. This method is unstable for Δt chosen too large, resulting in growing oscillations and therefore limiting Δt.

Applying this method, the heat equation is written:

$$\frac{u_{i,j}^{k+1} - u_{i,j}^k}{\Delta t} = \chi_\parallel \frac{u_{i+1,j}^k - 2u_{i,j}^k + u_{i-1,j}^k}{2(\Delta y)^2} + \chi_\perp \frac{u_{i,j+1}^k - 2u_{i,j}^k + u_{i,j-1}^k}{2(\Delta x)^2}$$

Multiplying with Δt and adding $u_{i,j}^k$ yields an explicit equation for $u_{i,j}^{k+1}$, being only dependent on values at time step k.

For a system with $M \times N$ elements, the computational effort scales with $M \cdot N$. For a quadratic systems $M = N$ we find $\mathscr{O}(N^2)$.

In explicit discretisation schemes information – in the case described heat – is limited to travel one cell per iteration. The Courant-Friedrichs-Lewy-condition (CFL-condition) limits the step width according to the spatial resolution and the velocity. The diffusivity by definition relates the average squared step width Δh in the random walk process with the time step Δt:

$$\chi = \frac{\langle \Delta h^2 \rangle}{\Delta t} \tag{3.55}$$

The CFL condition applied to the 2D heat equation is thus:

$$\Delta t \leqslant \min\left(\frac{\Delta x^2}{\chi_\perp}, \frac{\Delta y^2}{\chi_\parallel}\right) \tag{3.56}$$

The computational time to simulate a given time in the simulated system therefore scales with $\mathscr{O}(N^4)$.

3.5.3. Euler Implicit

An unconditionally stable formulation is given by Eulers backward method, where the derivative is calculated at the next time step

$$u_i^{k+1} = u_i^k + \Delta t\, f(t^{k+1}, u_i^{k+1}) \tag{3.57}$$

resulting in an implicit formulation of the differential equation. The time steps can be chosen arbitrary, while lower values result in more precise solutions. The heat equation is written:

$$\frac{u_{i,j}^{k+1} - u_{i,j}^{k}}{\Delta t} = \chi_{\parallel} \frac{u_{i+1,j}^{k+1} - 2u_{i,j}^{k+1} + u_{i-1,j}^{k+1}}{2(\Delta y)^2} + \chi_{\perp} \frac{u_{i,j+1}^{k+1} - 2u_{i,j}^{k+1} + u_{i,j-1}^{k+1}}{2(\Delta x)^2}$$

$u_{i,j}^{k}$ is the only known quantity in this equation, the new temperature field is found by solving $M^2 \cdot N^2$ equations. For a quadratic system $M = N$ the time for one iteration scales with $\mathscr{O}(N^4)$. The discretisation width Δt leading to precise solutions is again the CFL-condition, though the initial time step can be chosen larger.

3.5.4. Crank-Nicolson Method

Another method called Crank-Nicolson (CN) can be thought as average of the forward and backward Euler method, formulated as:

$$u_i^{k+1} = u_i^k + \Delta t \left(\frac{f(t^{k+1}, u_{k+1}) + f(t^k, u^k)}{2} \right) \tag{3.58}$$

It is unconditionally stable and, in contrast to the first order accurate schemes above, second order accurate in time. Benefit is a higher accuracy, as the derivatives at t^k and t^{k+1} are averaged.

The 2D heat equation with this discretisation writes

$$\begin{aligned} \frac{u_{i,j}^{n+1} - u_{i,j}^{n}}{\Delta t} = \frac{\chi_{\parallel}}{2} \left[\frac{u_{i+1,j}^{n+1} - 2u_{i,j}^{n+1} + u_{i-1,j}^{n+1}}{(\Delta y)^2} + \frac{u_{i+1,j}^{n} - 2u_{i,j}^{n} + u_{i-1,j}^{n}}{(\Delta y)^2} \right] \\ + \frac{\chi_{\perp}}{2} \left[\frac{u_{i,j+1}^{n+1} - 2u_{i,j}^{n+1} + u_{i,j-1}^{n+1}}{(\Delta x)^2} + \frac{u_{i,j+1}^{n} - 2u_{i,j}^{n} + u_{i,j-1}^{n}}{(\Delta x)^2} \right] \end{aligned} \tag{3.59}$$

Scaling of iteration time with M and N is equivalent to the implicit Euler method.

This implicit approach allows to start with time steps around two to three orders of magnitude larger than given by the CFL-Condition. Towards convergence the time steps are reduced down to the CFL-Condition, to mitigate small scale oscillations and find an accurate steady state temperature field to the given boundary conditions.

3.5.5. Alternating Direction Implicit Method

By separating equation 3.51 for the perpendicular and the parallel transport, we find two 1D equations. They can be solved successively for each time step, representing

the so called alternating direction implicit method. It is applicable to independent operators and therefore also called operator splitting method. Time step Δt is split equidistantly for l alternating directions (operators) into:

$$\Delta t' = \frac{\Delta t}{l} \tag{3.60}$$

The calculation of the first operator uses time step k to $k + \frac{1}{l}$, the second $k + \frac{1}{l}$ to $k + \frac{2}{l}$ up to $k + \frac{l-1}{l}$ to $k + 1$. For convergence small time steps are needed, to avoid an influence of the order of executions.

For the Crank-Nicolson discretisation – splitting equation (3.59) for two directions – the effective time discretisation is

$$\Delta t' = \frac{\Delta t}{2} \tag{3.61}$$

and the 1D equations write:

$$\frac{u_{i,j}^{k+1/2} - u_{i,j}^{k}}{\Delta t'} = \frac{\chi_{\parallel}}{2}\left[\frac{u_{i+1,j}^{k+1/2} - 2u_{i,j}^{k+1/2} + u_{i-1,j}^{k+1/2}}{(\Delta y)^2} + \frac{u_{i+1,j}^{k} - 2u_{i,j}^{k} + u_{i-1,j}^{k}}{(\Delta y)^2}\right] \tag{3.62}$$

$$\frac{u_{i,j}^{k+1} - u_{i,j}^{k+1/2}}{\Delta t'} = \frac{\chi_{\perp}}{2}\left[\frac{u_{i,j+1}^{k+1} - 2u_{i,j}^{k+1} + u_{i,j-1}^{k+1}}{(\Delta x)^2} + \frac{u_{i,j+1}^{k+1/2} - 2u_{i,j}^{k+1/2} + u_{i,j-1}^{k+1/2}}{(\Delta x)^2}\right] \tag{3.63}$$

Both sides contain known and unknown quantities. As the two directions are treated analogously, the treatment for the parallel direction is further discussed. Introducing

$$\gamma = \gamma_{\parallel} = \frac{\chi_{\parallel}\Delta t}{2(\Delta y)^2} \tag{3.64}$$

and solving for the next time step $u^{k+1/2}$ – representing the unknowns – yields

$$-\gamma\, u_{i+1,j}^{k+1/2} + (1+2\gamma)u_{i,j}^{k+1/2} - \gamma u_{i-1,j}^{k+1/2} = \gamma u_{i+1,j}^{k} + (1-2\gamma)u_{i,j}^{k} + \gamma u_{i-1,j}^{k} \tag{3.65}$$

with the known quantities at time step k at the right hand side.

Note that $\chi(u)$ uses u_i^k, therefore γ refers to u^k within the current equation/line.

Using matrix presentation

$$\boldsymbol{A}\boldsymbol{u}^{k+1/2} = \boldsymbol{b}^{k} \tag{3.66}$$

the parameters on the left hand side are expressed by a tridiagonal matrix $\boldsymbol{A}$, connecting the unknown values $u^{k+1/2}$ in vector $\boldsymbol{u}$ with the known values u^k in vector $\boldsymbol{b}$. The actual matrix representation is presented in appendix A I.

In the case of different parallel and perpendicular diffusivities the introduction of two different heat potentials is necessary. Reason is the temperature dependence

$$\kappa = \kappa_0 \cdot T^{\phi} \tag{3.67}$$

where integration according to (2.16) yields:

$$u(T) = \kappa_0 \frac{T^{\phi+1}}{\phi+1} \tag{3.68}$$

For the special cases of perpendicular and parallel transport the heat potentials write:

$$u_{\perp}(T) = \kappa_{\perp,0} \frac{T^{\alpha+1}}{\alpha+1} \tag{3.69}$$

$$u_{\parallel}(T) = \kappa_{\parallel,0} \frac{T^{\beta+1}}{\beta+1} \tag{3.70}$$

Therefore the relation

$$u_{\parallel} = \kappa_{\perp,0} \cdot \left(\frac{u_{\perp}}{\kappa_{\parallel,0}} \right)^{\frac{\alpha+1}{\beta+1}} \tag{3.71}$$

has to be applied after the calculation for the perpendicular direction and

$$u_{\perp} = \kappa_{\parallel,0} \cdot \left(\frac{u_{\parallel}}{\kappa_{\perp,0}} \right)^{\frac{\beta+1}{\alpha+1}}$$

after the calculation of the parallel direction.

3.5.6. Linking χ and u

Temperature dependent diffusivities have to be taken into account to solve the heat diffusion equation (3.50). It is numerically costly to calculate χ if $\frac{\kappa}{n}$ is used as representation. Solving equation (3.68) for temperature T

$$T = \sqrt[\beta+1]{\frac{u\,(\beta+1)}{\kappa_0}} \tag{3.72}$$

the conductivity is given as:

$$\kappa(u) = \kappa_0 \cdot \left(\frac{(\beta+1)u}{\kappa_0} \right)^{\frac{\beta}{\beta+1}} \tag{3.73}$$

$\chi(u)$ is calculated from the conductivity and density:

$$\chi = \frac{\kappa}{n} = \frac{\kappa_0}{n} T^{\beta} = \frac{\kappa_0}{n} \left(\frac{(\beta+1)u}{\kappa_0} \right)^{\frac{\beta}{\beta+1}} \tag{3.74}$$

This is computationally demanding because of the rational exponent. Expressing the density according to the ideal gas equation $n = \frac{p}{T}$ yields

$$\chi = \frac{\kappa}{p} T = \frac{\kappa_0}{p} T^{\beta+1} = \frac{\kappa_0}{p} \left(\frac{(\beta+1)u}{\kappa_0} \right) = (\beta+1)\frac{u}{p} \tag{3.75}$$

The diffusivity is given by the heat potential over the pressure. Storing

$$p' = \frac{\beta+1}{p} \tag{3.76}$$

as constant yields χ as function of u with a single multiplication, saving computation time and reducing round-off errors.

3.5.7. Boundary Conditions

Up to now the heat diffusion equation inside the discrete system is considered, neglecting the boundaries of the grid. As boundary condition a temperature or heat flux is set. They represent Dirichlet and Neumann boundary conditions, fixing the quantity u or its first derivative ∇u respectively. The following explanations apply for the Crank-Nicolson method with alternating direction method.

The boundary conditions have to be chosen with care for several reasons. Fixing the heat flux at every boundary prevents systems which constantly gain or lose net heat to reach a steady state condition. A heat flux directed outwards of the system can result in a negative temperature next to the boundary. A fixed heat flux density upstream is preferred about a fixed temperature profile, as suggested by the physical model. Downstream a heat outflux is expected with the parallel conductivity scaling with $T^{5/2}$. To circumvent instabilities a fixed temperature is used.

Fixed Heat Flux Density

The heat potential derivative resembles the heat flux, for example from index $i-1$ to i, according to Fourier's law:

$$q = q_{i-1 \to i,\, j} = \frac{u_{i-1,j} - u_{i,j}}{\Delta y} \tag{3.77}$$

Equation (3.62) is thus written:

$$\frac{u_{i,j}^{k+1/2} - u_{i,j}^{k}}{\Delta t'} = \frac{\chi_{\parallel}}{2} \left[\frac{\frac{q_{i\to i+1,\,j}^{k+1/2}}{\Delta y} - \frac{q_{i-1\to i,\,j}^{k+1/2}}{\Delta y}}{\Delta y} + \frac{\frac{q_{i\to i+1,\,j}^{k}}{\Delta y} - \frac{q_{i-1\to i,\,j}^{k}}{\Delta y}}{\Delta y} \right] \tag{3.78}$$

Fixing the heat flux density from index $i-1$ to i and keeping the other heat potential expression leads to:

$$\frac{u_{i,j}^{k+1/2} - u_{i,j}^{k}}{\Delta t'} = \frac{\chi}{2} \left[\frac{\frac{-u_{i+1,j}^{k+1/2} + u_{i,j}^{k+1/2}}{\Delta y} - q}{\Delta y} + \frac{\frac{-u_{i+1,j}^{k} + u_{i,j}^{k}}{\Delta y} - q}{\Delta y} \right] \tag{3.79}$$

Setting $i = 1$ and solving for the unknown values at $k + 1/2$ yields:

$$(1+\gamma) u_{1,\,j}^{k+1/2} - \gamma \cdot u_{2,\,j}^{k+1/2} = \gamma' \cdot q + (1-\gamma)\, u_{1,\,j}^{k} + \gamma \cdot u_{2,\,j}^{k} \tag{3.80}$$

The temperature at the boundary is adjusted to maintain the fixed heat flux.

Fixed Temperature

A fixed temperature ($T = \text{const} \iff u = \text{const}$) can be implemented inside the matrix or outside, for example at index $i = M$ or $i = M + 1$ respectively. At boundary $i = M$, included in the matrix representation of the heat potential field, this is expressed writing

$$u_{M,j}^{k+1/2} = u_{M,j}^{k} \tag{3.81}$$

with equation at $i = M - 1$ unchanged. This leads to a constant value in the matrix and a trivial equation in the system of linear equations. Containing this value in the matrix can be beneficial for further calculations, but is not optimal from a computational point of view, enlarging M by one.

Setting the boundary at $i = M + 1$ equation (3.65) is written for $i = M$:

$$-\gamma\, u_{M-1,j}^{k+1/2} + (1+2\gamma) u_{M,j}^{k+1/2} = \gamma u_{M-1,j}^{k} + (1-2\gamma) u_{M,j}^{k} + 2\gamma u_{M+1,j} \tag{3.82}$$

the last term expresses the known boundary condition, not contained in the matrix representation, but given as parameter.

In both cases a heat flux forms to maintain the boundary condition, delivering a smooth solution.

4.Experimental Setup

In this chapter the experimental diagnostics used to obtain data as basis for the numerical simulation are explained. This includes infrared thermography and Langmuir probes. In the end, experimental heat flux profiles are compared to the 1D model.

4.1. Infrared Thermography

Thermography deduces the temperature of a surface by measuring its emitted thermal radiation. Basis is Planck's Law of radiation, describing the emission of electromagnetic radiation from an ideal black body with finite temperature. The spectral radiance M_e emitted by a black body of temperature T at wavelength λ and surface area dA is described by

$$M_e(T,\lambda)\,\mathrm{d}A\,\mathrm{d}\lambda = \frac{2\pi hc^2}{\lambda^5}\frac{1}{\exp\left(\frac{hc}{\lambda kT}\right)-1}\,\mathrm{d}A\,\mathrm{d}\lambda \qquad \left[\frac{\mathrm{W}}{\mathrm{m}^2\,\mu\mathrm{m}\,\mathrm{sr}}\right] \tag{4.1}$$

where k denotes the Boltzmann constant, h the Planck constant and c the speed of light.

The cameras used in the experiments measure the photon flux M_γ instead of the spectral radiance M_e. The rate of photons is expressed by taking the energy per photon at a certain wavelength

$$E_\gamma = \frac{hc}{\lambda} \tag{4.2}$$

into account:

$$M_\gamma(T,\lambda)\,\mathrm{d}A\,\mathrm{d}\lambda = \frac{2\pi c}{\lambda^4}\frac{1}{\exp\left(\frac{hc}{\lambda kT}\right)-1}\,\mathrm{d}A\,\mathrm{d}\lambda \qquad \left[\frac{1}{\mathrm{m}^2\,\mu\mathrm{m}\,\mathrm{sr}\,\mathrm{s}}\right] \tag{4.3}$$

Real surfaces are not ideal black bodies, but reflect part of the incident radiation, a ratio called reflectivity R. The grey body is a first approximation to real surfaces, where the emissivity is defined as:

$$\epsilon = 1 - R \tag{4.4}$$

The radiated fluxes for a grey body are $\epsilon < 1$ times the black body radiation:

$$M_{\gamma,gb}(T,\lambda)\,\mathrm{d}A\,\mathrm{d}\lambda = \frac{2\pi c\,\epsilon}{\lambda^4}\frac{1}{\exp\left(\frac{hc}{\lambda kT}\right)-1}\,\mathrm{d}A\,\mathrm{d}\lambda \qquad \left[\frac{1}{\mathrm{m}^2\,\mu\mathrm{m}\,\mathrm{sr}\,\mathrm{s}}\right] \tag{4.5}$$

The photon flux emitted by a surface into the half space is calculated by solving the integral

$$\Gamma(T) = \int\int \epsilon\frac{2\pi c}{\lambda^4}\frac{1}{\exp\left(\frac{hc}{\lambda kT}\right)-1}\,\mathrm{d}A\,\mathrm{d}\lambda \tag{4.6}$$

which can be approximated for the effective wavelength λ_{eff}:

$$\Gamma(T) \simeq c_0\frac{2\pi c\epsilon}{\lambda_{eff}^4}\frac{1}{\exp\left(\frac{hc}{\lambda_{eff}kT}\right)-1} \tag{4.7}$$

The calibration coefficient c_0 depends on the aperture and sensitivity of the camera and losses in the optical system. Solving this equation for the temperature yields:

$$T = \frac{hc}{\lambda_{eff}k}\frac{1}{\ln\left(\frac{2\pi c\epsilon}{\lambda_{eff}^4}\cdot\frac{c_0}{\Gamma}+1\right)} \tag{4.8}$$

IR cameras are used to determine the spatial temperature distribution of surfaces. They are suited for measurements on the divertor targets, as they don't suffer from the harsh conditions in the divertor region. The temperature evolution is used to calculate heat flux densities onto the surface. This is done by solving the $2D$ heat equation (2.20) with the THEODOR (thermal heat load onto divertor) code, to gain a heat flux profile [24]. Two examples for the resulting heat flux are shown in figures 4.1(a) and 4.1(b) for similar λ_q and q_0 and different S.

Sources of error are the incomplete knowledge of the temperature dependent emissivity $\epsilon(T)$ of the tungsten targets and reflections due to their high reflectivity ($\epsilon \simeq 0.2$). Treating the target plates of interest with sandblasting results in surfaces with higher emissivity, see figure 4.2, lowering both uncertainties.

The cameras used operate in the region of 4.7 µm, to get an appropriate increase of photon flux in the most relevant temperature region: from 300 K to 2500 K [11]. Error sources due to line radiation produced in the divertor region is mitigated, compared to measurements at lower wave lengths.

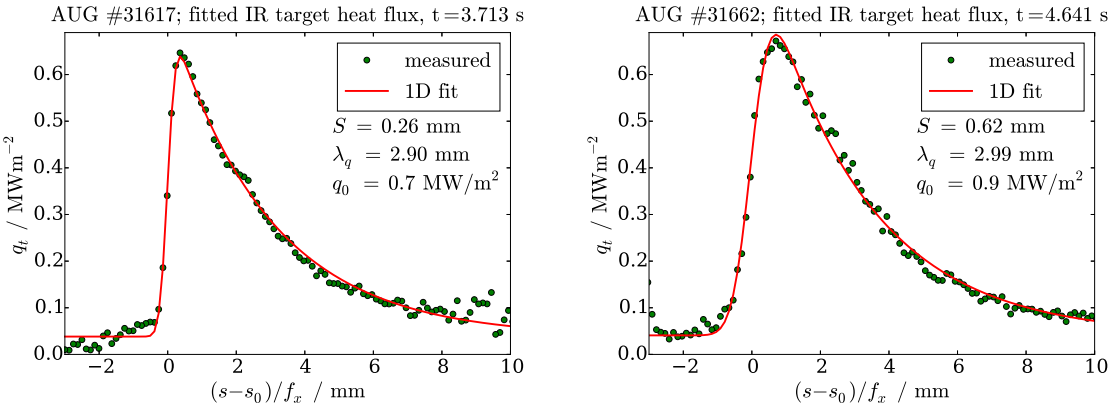

(a) Low density $n_e = 1.5 \cdot 10^{19}\,\mathrm{m}^3$. (b) Medium density $n_e = 3.0 \cdot 10^{19}\,\mathrm{m}^3$.

Figure 4.1.: Heat flux density profiles measured in ASDEX Upgrade in deuterium for different densities n_e. λ_q and q_0 are similar, showing the different shape and deviation to the 1D fit for different S.

Figure 4.2.: Lower Divertor in ASDEX Upgrade, showing the higher surface roughness – therefore lower reflectivity – of the sandblasted area on the tiles [2].

4.2. Langmuir-Probes

Langmuir probes (LP) are a common diagnostic to measure the density and temperature of the electrons and ions based on currents received by the LP. A basic sketch is shown in figure 4.3 with the probe consisting of an insulated wire with a small tip being in contact with the plasma.

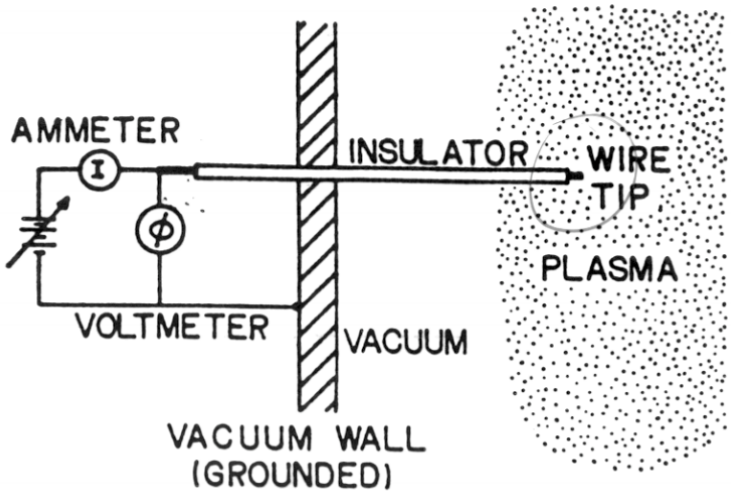

Figure 4.3.: Sketch for a Langmuir probe with current and voltage measurement. The probe consists of metal, usually tungsten or molybdenum.

A current I from the probe to a reference potential – in figure 4.3 given by the wall – is measured. The potential difference is measured as voltage U. An IU characteristic is measured by applying an offset voltage. Figure 4.4 shows the characteristic of such a voltage ramp as blue line. The total current is composed of an electron current, shown in red, and an ion current, shown in green. Negative voltages measured, from the probe to the plasma, repel electrons and attract ions, lowering the current. At the so called ion saturation voltage I_i^{sat} no electrons will reach the tip and the current is limited by the ion flow from the plasma to the probe surface. Positive voltages hinder ions from reaching the tip, while electrons are accelerated towards the tip, increasing the current until the electron saturation current I_e^{sat} is reached.

No current is measured for equal ion and electron flows to the tip, which is the case for the so called floating potential. This potential forms at insulated probes.

The probes used in ASDEX Upgrade are shown in graphic 4.5., with the baffle dome between the inner and outer divertor partially assembled. The probes are isolated against the target plates.

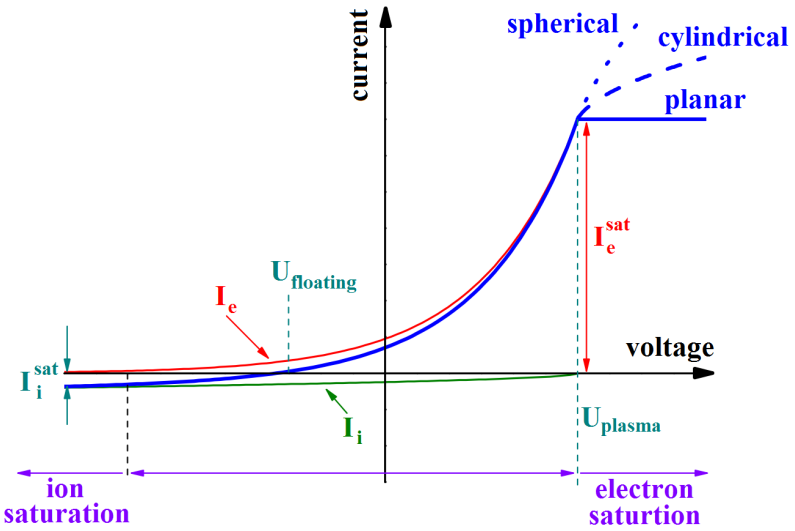

Figure 4.4.: Schematic IV diagram for a single Langmuir probe, based on [25].

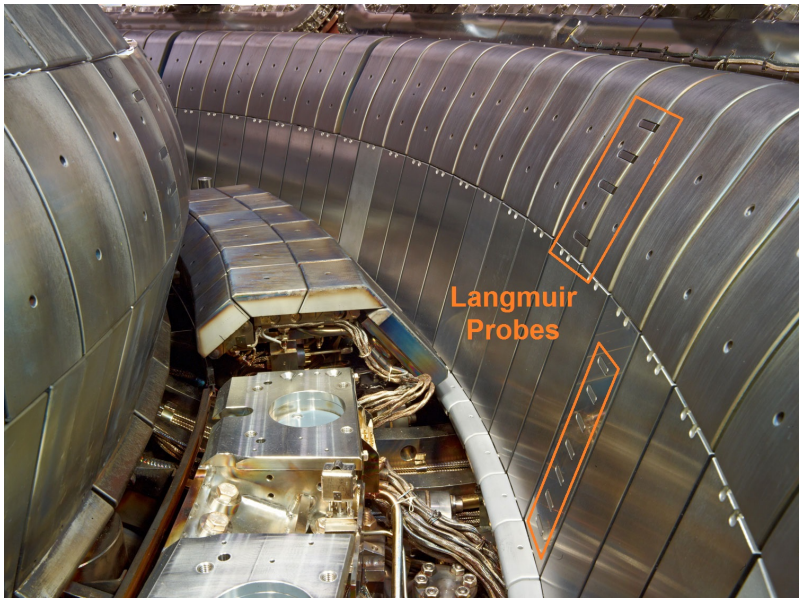

Figure 4.5.: Lower Divertor in ASDEX Upgrade, two tiles with Langmuir probes [2] are marked in orange.

Calculations

The ion sound velocity at the sheath is described by the Bohm criterion

$$c_s \geqslant \sqrt{\frac{Z\,T_e + \gamma_i T_i}{m_i}} \tag{4.9}$$

with ion charge number Z, electron temperature T_e, ion temperature T_i, adiabatic coefficient γ_i of the ions and ion mass m_i [11], [23]. This condition applies to the entry of the so called sheath, a volume where the plasma interacts with the surface. All temperatures and densities in the following refer to this location. Assuming quasi neutrality the charge density is expressed as product of the electron density n_e and the elementary charge e, resulting in the ion current density:

$$j_i^{sat} = c_s n_e e \tag{4.10}$$

Knowing the sheath surface S, the absolute ion saturation current is

$$I_i^{sat} = S \cdot j_i^{sat} = S\,c_s n_e e \tag{4.11}$$

For non planar probes the extent of this layer influences S with respect to the probe surface. The widening of the sheath for high positive voltages is the reason for the electron current rising after the ideal electron saturation voltage, at the right hand side of figure 4.4.

The electron current is found to be [15]

$$I_e = S n_e e \sqrt{\frac{T_e}{2\pi m_i}} \cdot \exp\left(\frac{e\,(\phi_p - U)}{T_e}\right) \tag{4.12}$$

with plasma potential ϕ_p. Setting the probe to ϕ_p the electron saturation current is found:

$$I_e^{sat} = S n_e e \sqrt{\frac{T_e}{2\pi m_i}} \tag{4.13}$$

The total current is defined by the sum of the ion and electron currents

$$I_{tot} = I_e + I_i \tag{4.14}$$

defining the floating potential with:

$$I_{tot}(U_{float}) \equiv 0 \tag{4.15}$$

Three voltages are defined by currents in the characteristic:

$$U_1 = U(I_{tot} = I_i^{sat}) \tag{4.16}$$

$$U_2 = U(I_{tot} = -I_i^{sat}) \tag{4.17}$$

$$U_3 = U(I_{tot} = 0) \tag{4.18}$$

Applying the introduced relations we can deduce the electron temperature and density:

$$T_e = \frac{e(U_2 - U_3)}{\ln(2)} \tag{4.19}$$

$$n_e = \frac{I_i^{sat}}{eSc_s} \tag{4.20}$$

the ion sound speed c_s given in equation (4.9) includes the ion and the electron temperature, so that further measurements or assumptions are needed to identify n_e.

Errors occur because the applied voltage alters the potential distribution in the plasma itself. In addition the magnetic field in a tokamak alters the behaviour of the plasma, as the magnetic pre sheath has to be taken into account [23].

Measurements

Measurements with Langmuir probes gain spatial resolution by performing a so called sweep. Therefore the plasma shape is altered to move the separatrix poloidal along the target. Figure 4.6(a) shows the positions of six Langmuir probes with respect to the separatrix during a sweep at JET (Joint European Torus). JET is a tokamak operated by the CCFE in Culham, England. The position is given in target coordinates s. The resulting profile for the electron temperature is shown in figure 4.6(b). Plotting the values from adjacent probes during the sweep results in a smooth profile, with the error known to increase for temperatures $< 5\,\text{eV}$. Figure 4.7(a) shows the electron density deduced from the same data set, showing a discontinuity between probe *S20A* and *S21B*. The spatial offset exhibits an uncertainty in s of up to 2 cm, caused by the magnetic reconstruction of the plasma shape. A possible correction is to apply the 1D fit to the heat flux profile as shown in figure 4.7(b).

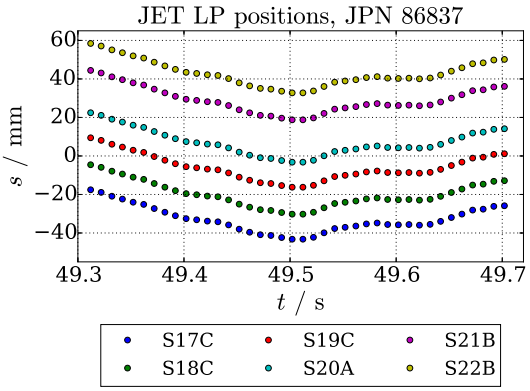

(a) Langmuir probe positions.

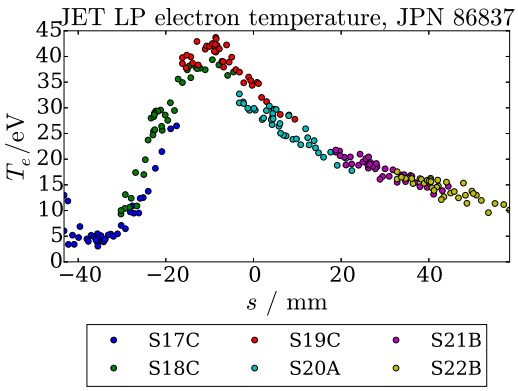

(b) Electron temperature.

Figure 4.6.: (a) Langmuir probe position and (b) corresponding electron temperature during a sweep in JET. The combined data of single probes form a profile with higher resolution than the probe distance.

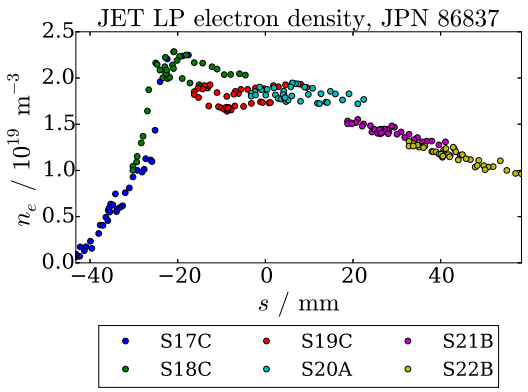

(a) Electron density.

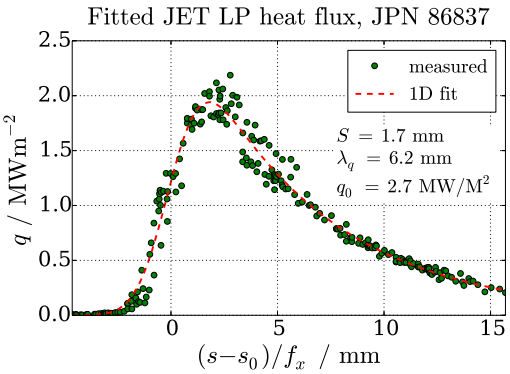

(b) 1D model fitted to heat flux density profile.

Figure 4.7.: (a) Electron density measured and heat flux calculated from Langmuir probe data at JET, corresponding to figure 4.6. For the heat flux density (b) the lateral offset is corrected according to 1D fit: $s_0 = -20.1\,\mathrm{mm}$. The fitted data and the resulting plot are in poloidal coordinates mapped upstream using the flux expansion $f_x = 5$.

4.3. Discrepancy to Fits and Simulations

Experimental heat flux profiles are characterised by the 1D-Model explained in section 2.3. A characteristic deviation in the heat flux profile for certain plasma conditions is observed. As R. Goldston has shown [26], a pure diffusive 2D Model results in heat flux profiles which are closer to the experimental results, allowing to study the errors made within the 1D approach.

A fitted heat flux density profile is shown in figure 4.8, with the decrease in the PFR being described too fast by the fitted 1D Model. A similar deviation is shown in figure 4.9 for a performed 2D simulation. Note that the profile in the simulation is independent of q_0 for target temperature $T_t = 0$.

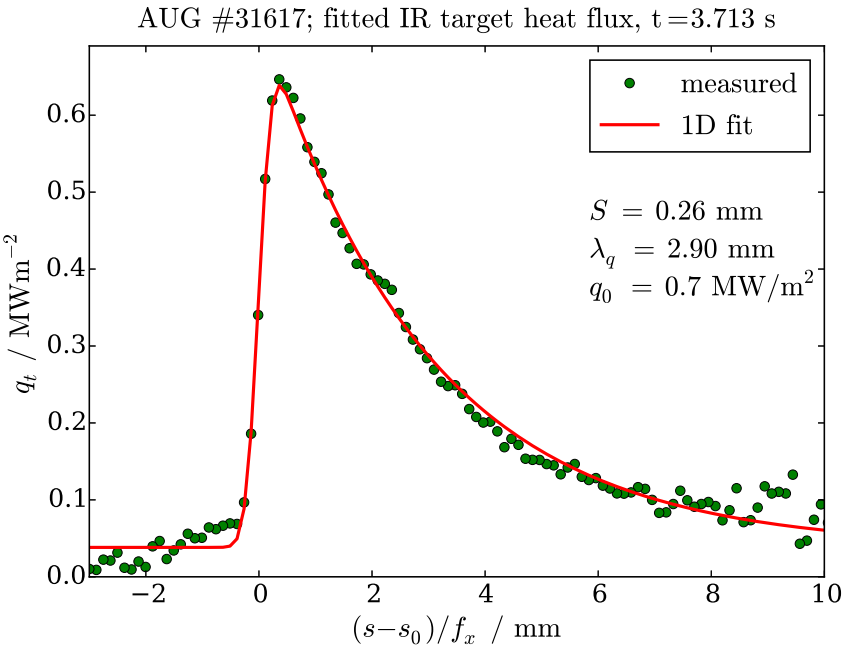

Figure 4.8.: Fitted heat flux density profile from ASDEX Upgrade with electron density $n_e = 1.5 \cdot 10^{19}\,\mathrm{m}^3$.

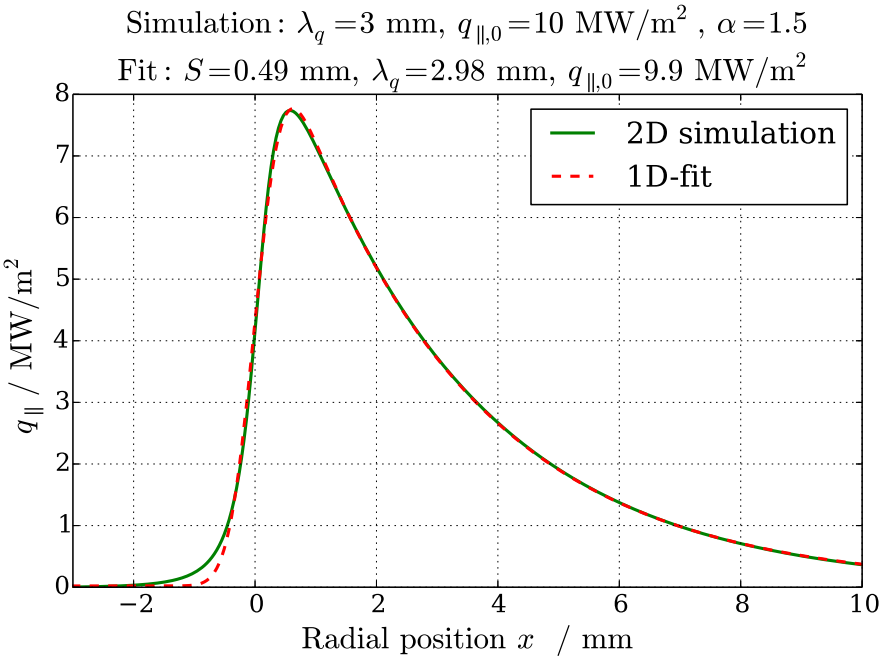

Figure 4.9.: Fitted heat flux density profile from 2D simulation.

5.Evaluation and Interpretation

In this chapter the simulations are evaluated, interpreted and compared to measured data and analytic approximations. The possibility to approximate S based on geometry and transport parameters is investigated and validated by 2D simulations.

In addition the picture of a Gaussian spreading function is extended and alternative fit functions for the target heat flux density profile are proposed. Potential quantities to identify the temperature dependence of the perpendicular transport are deduced and their applicability to experimental data is investigated.

5.1. Different Geometries

In this section the two geometries introduced in section 3.2, namely the upstream and the divertor configuration, are compared and the preferred geometry for further simulations is chosen.

For the upstream configuration (figure 3.4) the heat flux density profile decays radially towards the X-point due to perpendicular diffusion, shown in section 3.2. This is quantified by $\lambda_{q,fit}$ deduced by the 1D fit function (section 2.3) at the target being larger than the upstream boundary condition $\lambda_{q,U}$. Figure 5.1 shows the parallel heat flux density profile crossing the X-point for the upstream configuration and the X-point profile described by the 1D model. At the separatrix the profile shows a narrow peak larger than q_0 upstream. This additional heat flux is transported radially towards the separatrix above the X-point. The deviation with respect to the exponential profile depends on different parameters like the heat flux decay length λ_q and the temperature dependency of the perpendicular transport α, making this configuration unfavourable for further investigations. Figure 5.2 shows the parallel heat flux density along the field lines close to the separatrix in the simulation. The extent of the peak with $q_\parallel > q_0$ is narrow in radial and parallel direction. Due to the strong perpendicular heat transport below the X-point into the PFR, the parallel heat flux density and temperature do not have their peak at the separatrix, in the divertor region.

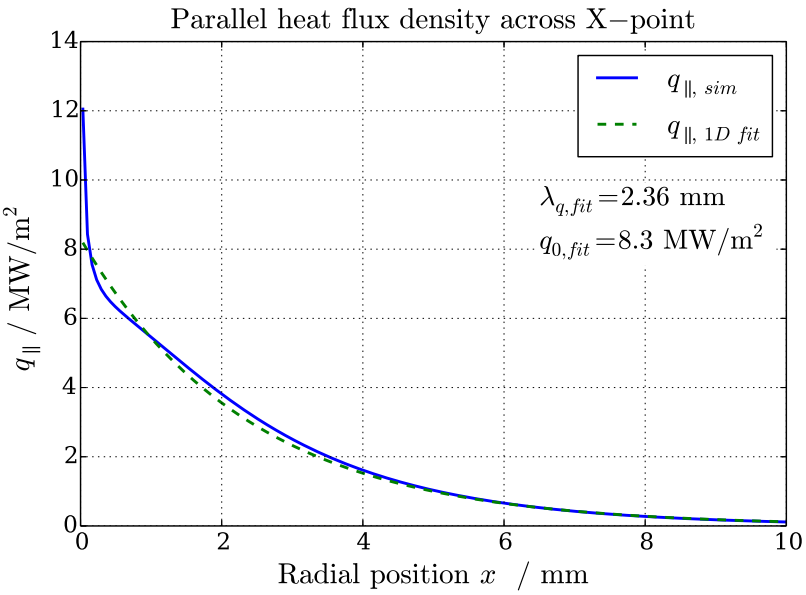

Figure 5.1.: Parallel heat flux density entering the divertor region in the upstream configuration. The profile deviates from the proposed exponential, with the fall-off length away from the separatrix being well reproduced by the 1D fit at the target.

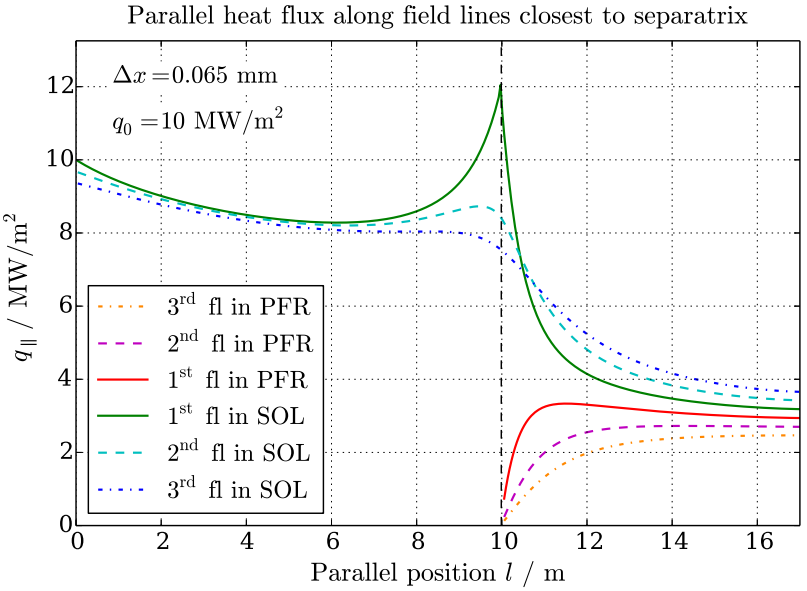

Figure 5.2.: Parallel heat flux density for the three field lines (fl) closest to the separatrix in the PFR and SOL. At the X-point, the differences in the parallel heat fluxes of adjacent field lines are large with respect to the radial discretisation of around $\frac{1}{30}\lambda_q$.

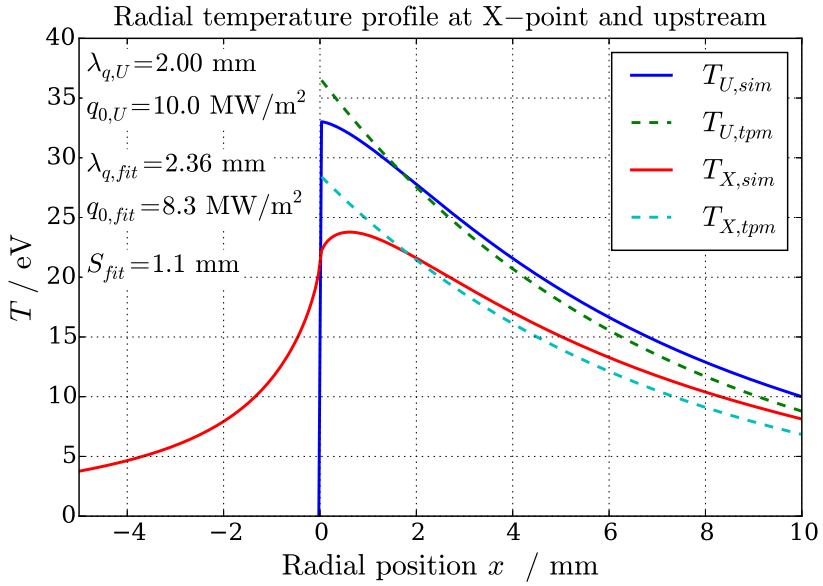

Figure 5.3.: Comparison of temperature profile upstream found in simulation and the X-point to the predictions of the two point model for constant $q_{\parallel}$.

Figure 5.3 compares the radial temperature profiles upstream and at the entrance of the divertor region to the prediction by the two point model, assuming a fixed parallel heat flux density

$$q(x) = q_0 \exp\left(-\frac{x}{\lambda_q}\right) : x > 0 \tag{5.1}$$

along the field lines. For the upstream configuration perpendicular transport increases the heat flux in the SOL away from the separatrix, so that the upstream temperature profile is underestimated by using q_0 and λ_q from upstream boundary conditions. Below the X-point the perpendicular temperature gradient transports heat from the SOL near the separatrix into the PFR. Therefore the temperature close to the separatrix is significantly underestimated and the radial temperature profile below the X-point does not have its peak at the separatrix but in the SOL. This holds true for both configurations. This behaviour raises the question if $\lambda_{q,U}$ of the upstream heat flux profile or the fitted target value $\lambda_{q,fit}$ is the proper quantity for parameter studies. The X-point temperature for the divertor configuration varies in the order of 1% compared to the profile found in the upstream configuration for similar λ_q and S.

It is found that the fitted $\lambda_{q,fit}$ for the divertor configuration is in agreement with the corresponding X-point value. Figure 5.4 shows the relative deviation from the

fit parameter $\lambda_{q,fit}$ to the boundary condition $\lambda_{q,sim}$ at the X-point with respect to the ratio $\frac{S_{fit}}{\lambda_q}$. This ratio expresses the perturbation of the parallel heat flux profile by perpendicular heat transport. This characteristic deviation implies that the spreading of the parallel heat flux is not sufficiently described by a convolution with a Gaussian. This finding gives rise to further investigations about the shape of the heat flux profiles, performed in section 5.5. Due to the geometry used in the following analysis the error in λ_q holds for each ratio $\frac{S}{\lambda_q}$. A regression for $\alpha = 1$ and $\alpha = 1.5$ describes the relative error

$$\Delta\lambda_q = (2.72 \pm 0.63) \cdot \frac{S_{fit}}{\lambda_q} + (7.98 \pm 0.77) \cdot \left(\frac{S_{fit}}{\lambda_q}\right)^2 \tag{5.2}$$

Note that the 1D fit applied to synthetic data with noise levels found in experiments exhibits an uncertainty in the order of 20% [11]. An increase of the error in λ_q with increasing S is expected, as the convolution with the Gaussian is getting dominant in the profile shape.

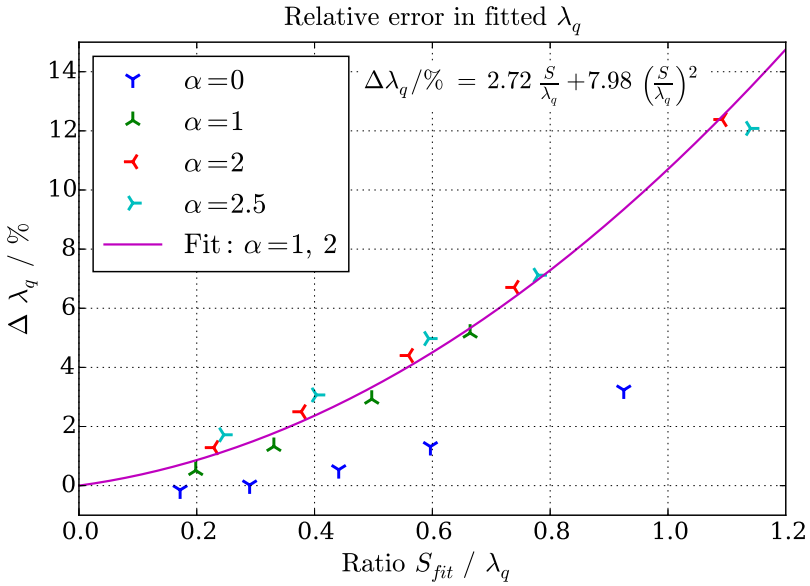

Figure 5.4.: Relative deviation of fitted $\lambda_{q,fit}$ in the divertor configuration with respect to the value $\lambda_{q,X}$ set at the X-point. The shown set utilises parameters $\lambda_{q,X} = 3\,\text{mm}$, $q_\parallel = 1\,\text{MW m}^{-2}$ and $L = 7\,\text{m}$.

The heat flux decay length λ_q refers to upstream coordinates. For the spreading in the divertor region the value at the divertor entrance is relevant. Therefore the divertor geometry is better suited for parameter studies comparing the 2D to the 1D model. Including parts of the SOL above the X-point on the other hand is better

suited for simulations with spatial dependent diffusivities, as they approach zero at the X-point in the slab geometry.

The question how λ_q evolves from the midplane to the X-point is not addressed in this thesis. [27] shows agreement between the temperature fall-off length at the outer midplane and λ_q deduced from target heat flux profiles according to the two point model, with the transport from the confined area to the SOL not governed by diffusion.

5.2. Applicability of the Two Point Model

In this section the applicability of the two point model (tpm) to approximate the parallel heat flux in the 2D diffusive heat transport is assessed. The parallel heat flux in the SOL near the separatrix is reduced by perpendicular heat transport, resulting in flatter temperature profiles compared to the two point model assuming a constant $q_\parallel$.

Perpendicular diffusion reduces the parallel heat flux density along the flux tubes close to the separatrix by transport into the private flux region (PFR). For the same λ_q, q_0 and S the profile shape of the perpendicular heat flux across the separatrix depends on α. Figure 5.5 shows parallel profiles of the perpendicular heat flux density across the separatrix for different exponents α, describing the temperature dependence of the perpendicular transport. The values are negative, because the PFR in the simulation is at the left hand side of the SOL and therefore the heat flux is oriented towards smaller x. The lower the temperature dependency α, the more heat passes the separatrix near the target, where the temperature is lowest. Note that the perpendicular heat flux density is forced towards zero at the target, because of the flat radial temperature profile used for these simulations. The integrated net heat flux across the separatrix is comparable for different α, quantified by the divertor spreading S. This raises the question, if the upstream temperature depends on α, as the perpendicular transport affects the parallel heat flux profile.

Figure 5.6 shows the ratio of the highest X-point temperature $T_{X,sim}$ found in the simulation to the temperature $T_{X,tpm}$ predicted by the two point model versus $\frac{S}{\lambda_q}$. No significant dependence on α is found. A higher divertor spreading affects the heat flux further in the SOL, reducing the highest temperature at the height of the X-point. In section 5.4 the X-point temperature is used to determine S.

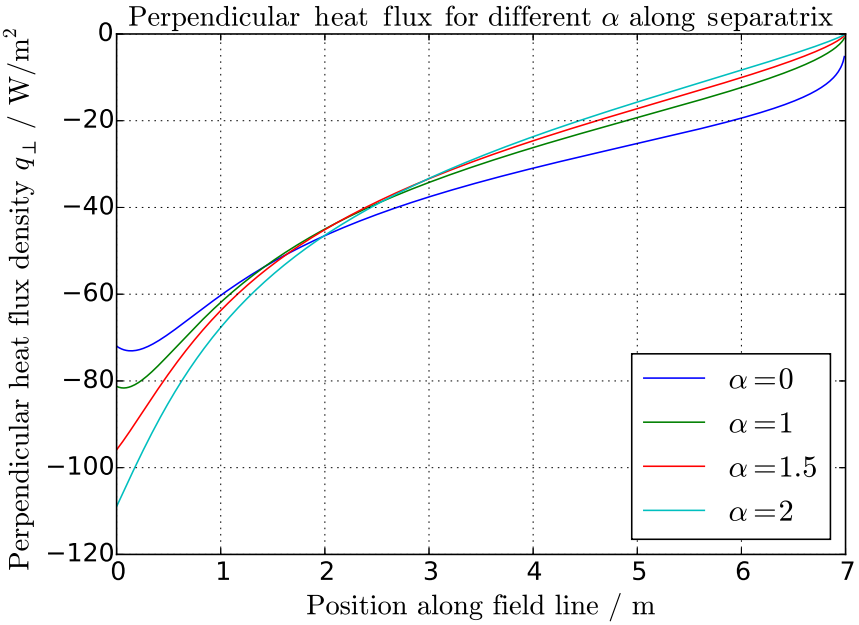

Figure 5.5.: Perpendicular heat flux density across separatrix for different temperature dependencies of the perpendicular transport.

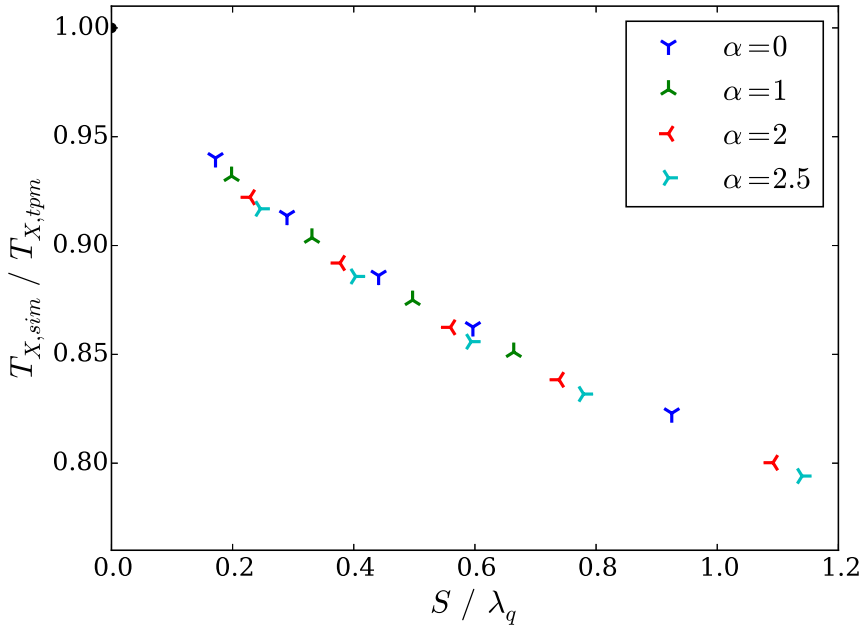

Figure 5.6.: Ratio of the highest X-point temperature found in the simulation to X-point temperature according to the two point model for constant $q_\parallel = q_0$.

The parallel heat flux is described by using the 1D model with an S depending on the parallel distance l to the X-point:

$$S(l) = S_{fit} \cdot \frac{l}{L} \tag{5.3}$$

The parallel temperature profile is found by integrating the resulting heat flux density $q(l)$ along a single field line:

$$T(l) = \left(T_t^{7/2} + \frac{7}{2\kappa_{\parallel,0}} \int_0^l q(l')\mathrm{d}l' \right)^{2/7} \tag{5.4}$$

Figure 5.7 shows the parallel temperature profile obtained by the numeric solution of the 2D heat diffusion equation and two analytic temperature profiles. The blue curves called TPM refer to the two point model for constant $q_\parallel = q_0$, resulting in the steepest profile and the highest X-point temperature. This temperature is not reached if perpendicular diffusion is taken into account. From the simulation the field line in the SOL next to the separatrix – itself not included in the simulation – and the field line with the highest X-point temperature are shown in green and red. Both are below the profile predicted by a constant heat flux density q_0. The cyan curve called $q(l)_{sep}$ resembles the integration result for the heat flux based on the 1D model at the separatrix $x = 0$. This curve describes the temperature profile found in the simulation better than integration for constant q_0 and therefore also the heat flux profile. The dependence of the temperature profiles in the simulations on α is small, despite the different temperature scaling of perpendicular transport discussed previously in this section. The highest X-point temperature in the simulation is not found at the separatrix, but due to the perpendicular heat transport into the PFR few tenth of millimetres into the SOL for all α. For the plots shown parameters $S_{fit} \simeq 1\,\mathrm{mm}$, $\lambda_q = 3\,\mathrm{mm}$ and $q_0 = 1\,\mathrm{MW\,m^{-2}}$ were used.

The introduced model assuming $S \propto l$ can be used as approximation of the diffusive heat transport. Figure 5.8 shows the parallel heat flux densities in the PFR, in the SOL and for the first field line in the SOL next to the separatrix. The dashed lines represent $q(l)$ for the corresponding radial positions. Due to the assumptions made for $q(l)$ the shape along a field line is not described correctly and is only an estimate, especially near the X-point. The heat flux in the SOL depends strongly on the radial position. The separatrix per definition separates the SOL from the PFR in the divertor region and receives no parallel heat flux at the X-point, to which it is connected.

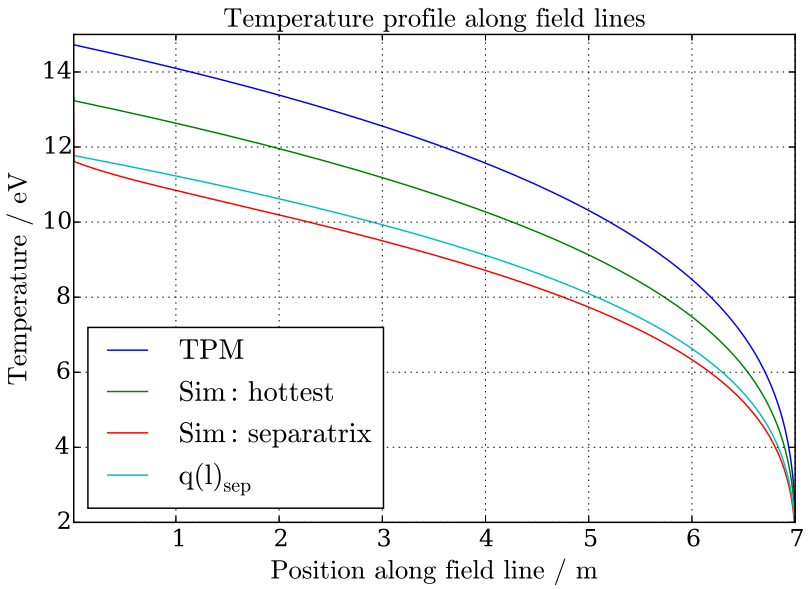

(a) $\alpha = 0.0$.

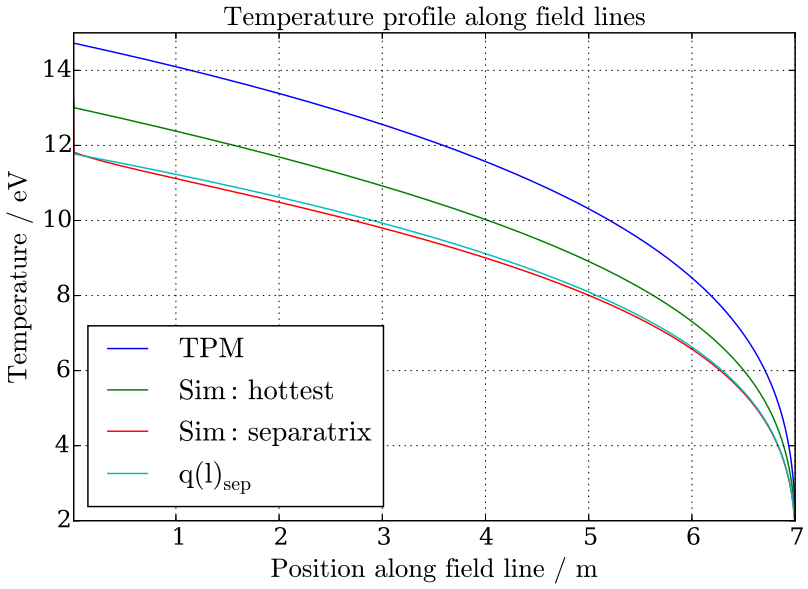

(b) $\alpha = 2.5$.

Figure 5.7.: Parallel temperature profiles for $\alpha = 0.0$ and $\alpha = 2.5$ for equal λ_q and q_0 and similar S_{fit}. From simulations the two profiles along the separatrix and for the hottest field line – with respect to the X-point – are shown in green and red. From theory profiles according to the two point model (TPM) for fixed $q = q_0$ in deep blue and using $q(l)$ given by the 1D Model for $S \propto l$ in cyan are shown for comparison.

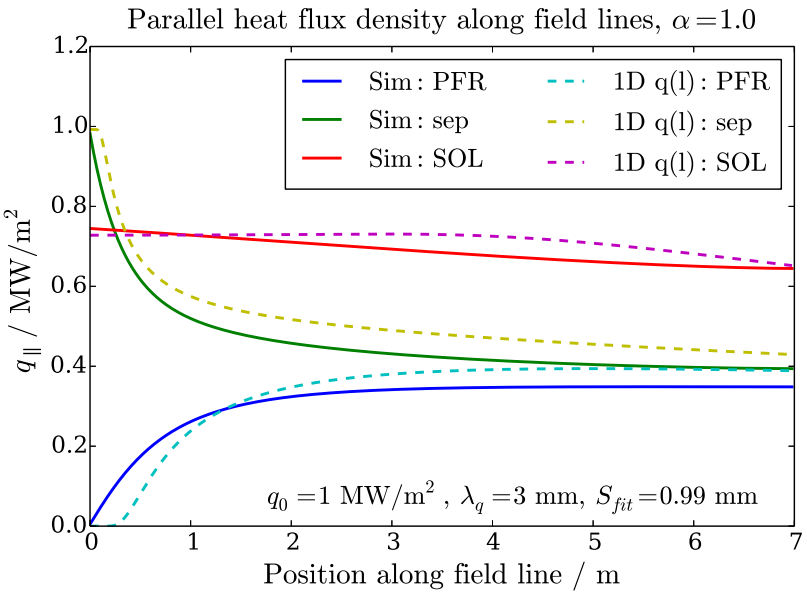

Figure 5.8.: Heat flux density along three field lines from the 2D simulation in comparison to the 1D model assuming linear dependence of S to L. Simulation results are shown as solid lines, 1D approximations as dashed lines.

Figure 5.9 shows the radial profile of the parallel heat flux 20 cm below the X-point. The 1D fit does describe the slope in the SOL correctly, but not the strong radial dependence around the separatrix. The value $S = 0.041\,\text{mm}$ at $l = 20\,\text{cm}$ below the X-point linearly extrapolated to the target yield $S = 1.4\,\text{mm}$, in contrast to $S = 1.0\,\text{mm}$ found at the target. This causes the deviation between simulation and the assumption $S \propto l$ shown in figure 5.8. The 1D model is not able do describe the heat flux profile near the X-point.

The underestimation of the heat flux density in the PFR leads to a deviation in the predicted X-point temperature. Figure 5.10 shows the temperature at the divertor entrance in the simulation and the profile predicted by the two point model integrating $q(l)$. The 1D function contains an offset q_{off} as parameter

$$q_\parallel(x) = \frac{q_0}{2} \exp\left(\left(\frac{S}{2\lambda_q}\right)^2 - \left(\frac{x - x_0}{\lambda_q}\right)\right) \cdot \operatorname{erfc}\left(\frac{S}{2\lambda_q} - \frac{x - x_0}{S}\right) + q_{off} \qquad (5.5)$$

to take a homogeneous background signal into account. This offset is found to be positive and small compared to q_0 for all simulations. Neglecting this offset results in a strong underestimation of the temperature profile at the divertor entrance, shown as blue dashed line in figure 5.10. Taking the offset in the integrating of $q(l)$ into

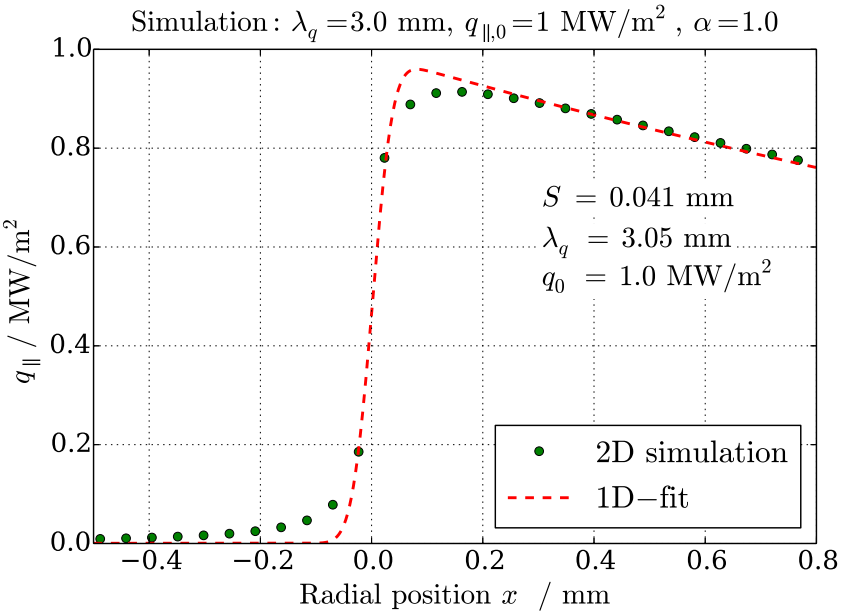

Figure 5.9.: 1D fit applied to the heat flux density profile at $l = 20\,\text{cm}$ below the X-point in divertor configuration. The separatrix is not included in the simulation.

account leads to a temperature offset, not describing the decay of the temperature profile in the PFR.

This result is of interest for the simulation, as an offset of $q_{off} \simeq q_0 10^{-3}$ results in a reduction of computation time for the initial temperature being determined via $q(l)$ as introduced in this section, see section 3.4.

The two point model in combination with the 1D model can be used for estimating the heat transport and temperature profile in the divertor region. However, the deviation is increasing for an increasing ratio of $\frac{S}{\lambda_q}$ and leads to a underestimation of the parallel heat flux in the PFR. The heat flux at the separatrix is well described with respect to the assumptions made.

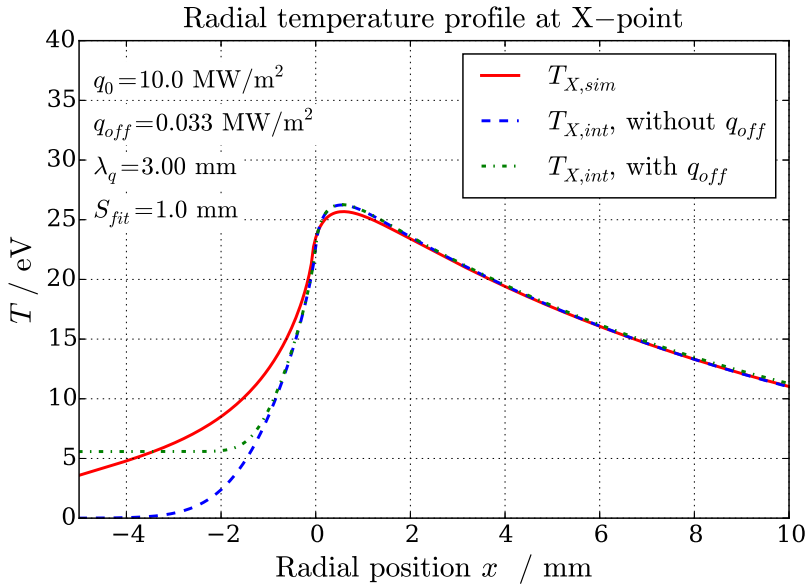

Figure 5.10.: X-point temperature profiles for $\alpha = 1$. The numerical solution as solid red line is compared to two profiles found by parallel integration assuming $S \propto l$.

5.3. Deriving S from Parallel Temperature Profile

In this section an approach to approximate S based on the parallel temperature profile given by the two point model (tpm) is introduced. The applicability of the two point model was assessed in the previous section.

The 1D model yields for the divertor spreading:

$$S = L\sqrt{\frac{\chi_\perp}{\chi_\parallel}} \tag{5.6}$$

Introducing the heat diffusivities

$$\chi_\parallel = \chi_{\parallel,0} T^\beta \tag{5.7}$$

$$\chi_\perp = \chi_{\perp,0} T^\alpha \tag{5.8}$$

with $\beta = \frac{5}{2}$ describing Spitzer-Härm conductivity for the parallel direction. $\alpha = 1$ describes a Bohm-like and $\alpha = 1.5$ a Gyro-Bohm-like temperature dependence. This allows to express the divertor spreading as

$$S = L\sqrt{\frac{\chi_{\perp,0}}{\chi_{\parallel,0}}} \cdot T_S^{\frac{\alpha-\beta}{2}} \tag{5.9}$$

with T_S being the relevant temperature to deduce S in this formulation. The dependence on the X-point temperature is analysed in section 5.4. As the ratio between the diffusivities in equation 5.6 expresses the ratio of the perpendicular to the parallel diffusion speed, the integral along a field line results in the expected radial spreading parameter

$$S = \int_0^L \sqrt{\frac{\chi_\perp}{\chi_\parallel}}\,\mathrm{d}l = \sqrt{\frac{\chi_{\perp,0}}{\chi_{\parallel,0}}} \int_0^L T(l)^{\frac{\alpha-\beta}{2}}\,\mathrm{d}l \tag{5.10}$$

with the temperature profile for constant $q_\parallel$ according to the two point model

$$T(l) = \left(T_t^{\beta+1} + (\beta+1)\frac{q_\parallel \cdot l}{\kappa_{\parallel,0}}\right)^{1/(\beta+1)} \tag{5.11}$$

depending on the target temperature T_t. For $T_t = 0$ we define the X-point temperature:

$$T_{X,0} = \left((\beta+1)\frac{q_\parallel \cdot L}{\kappa_{\parallel,0}}\right)^{1/(\beta+1)} \tag{5.12}$$

Equation (5.10) is rewritten using this temperature:

$$S = \sqrt{\frac{\chi_{\perp,0}}{\chi_{\parallel,0}}} \cdot \int_0^L \left(T_t^{\beta+1} + T_{X,0}^{\beta+1} \cdot \frac{l}{L}\right)^{\frac{\alpha-\beta}{2(\beta+1)}}\,\mathrm{d}l \tag{5.13}$$

With the solution

$$S = L \cdot \sqrt{\frac{\chi_{\perp,0}}{\chi_{\parallel,0}}} \cdot \frac{2(\beta+1)}{\alpha+\beta+2} \frac{\left(T_t^{\beta+1} + T_{X,0}^{\beta+1}\right)^{\frac{\alpha+\beta+2}{2(\beta+1)}} - T_t^{\frac{\alpha+\beta+2}{2}}}{T_{X,0}^{\beta+1}} \tag{5.14}$$

expressing S with $T_{X,0}$ – given by $q_\parallel$ – and T_t, both being measurable quantities in the experiment. Assuming $T_t = 0$ yields

$$S = L\sqrt{\frac{\chi_{\perp,0}}{\chi_{\parallel,0}}}\, T_X^{\frac{\alpha-\beta}{2}} \cdot \frac{2(\beta+1)}{\alpha+\beta+2} \tag{5.15}$$

where

$$\epsilon \equiv \frac{2(\beta+1)}{\alpha+\beta+2} \tag{5.16}$$

is identified as constant, connecting T_S with T_X in equation (5.9).

The relation

$$T_S^{\frac{\alpha-\beta}{2}} \stackrel{!}{=} T_X^{\frac{\alpha-\beta}{2}} \cdot \epsilon \tag{5.17}$$

leads to:

$$T_S = T_X \cdot \epsilon^{\frac{-2}{\beta-\alpha}} \tag{5.18}$$

The factor $(\frac{2(\beta+1)}{\alpha+\beta+2})^{\frac{-2}{\beta-\alpha}}$ for $\beta \equiv 2.5$ in dependence on α is shown in figure 5.11. Note that the temperature dependence of S vanishes for $\alpha = \beta$.

Finite target temperatures $T_t > 0$ alter the temperature profile and therefore affect T_S, being an integrated quantity. Figure 5.12 shows this correlation for three parallel heat fluxes $q_\parallel$. The higher the heat flux, the lower the impact of the target temperature on the temperature profile.

Figure 5.13 shows the dependence of S on the target temperature T_t relative to the

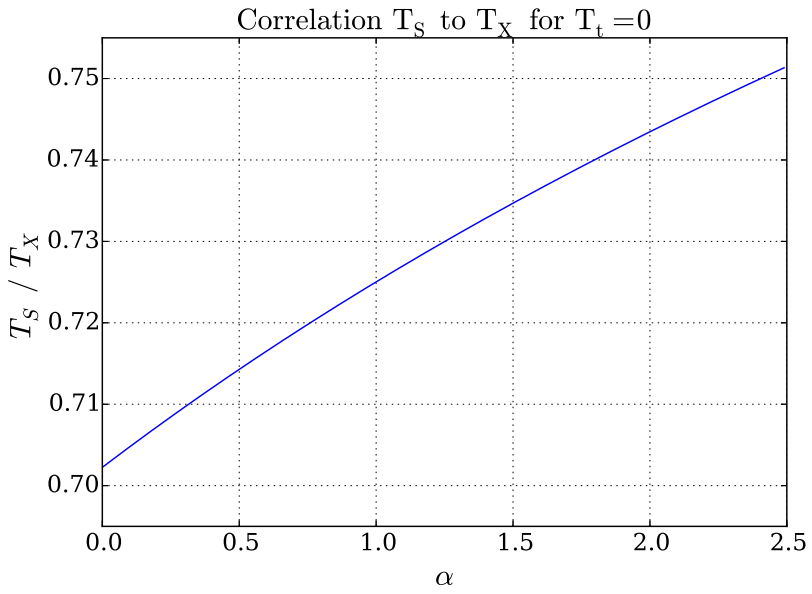

Figure 5.11.: Ratio T_S to T_X for $\beta \equiv \frac{5}{2}$, $0 \leqslant \alpha < 2.5$ and $T_t = 0$. This function is independent of $q_\parallel$ or L.

highest S value found for $T_t = 0$. The decrease of S with increasing temperature depends on $q_\parallel$. Higher target temperatures lower the divertor spreading, due to the higher temperature along the field line and the different temperature dependence of the perpendicular and parallel diffusivites with $\alpha < \beta$.

From this discussion it can be concluded that the estimation of S using equation 5.14 is not valid in presence of perpendicular heat transport in the divertor region. The temperature in a 2D calculation is below the two point model as shown in section 5.2. The actual values for S will be larger, while the trend for finite T_t found with this simple method holds, as shown in the following comparison to simulated and experimental data.

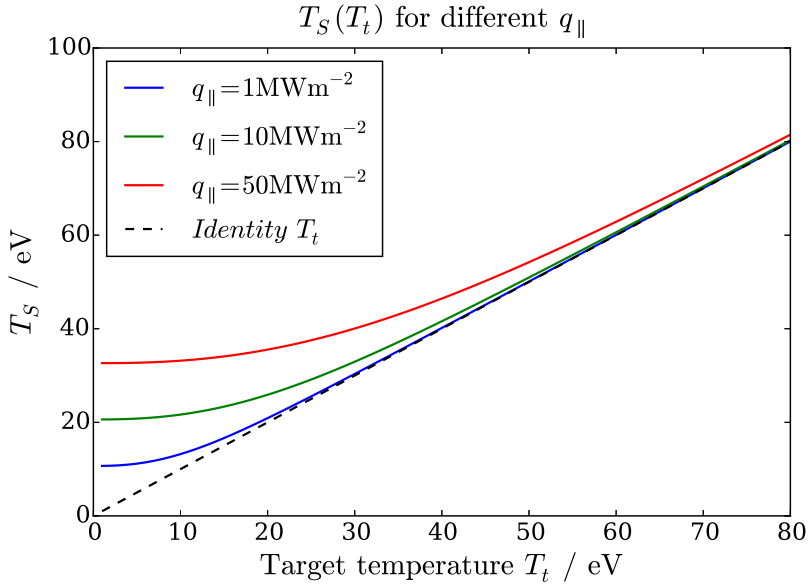

Figure 5.12.: T_S as function of T_t for different parallel heat fluxes $q_\parallel$.

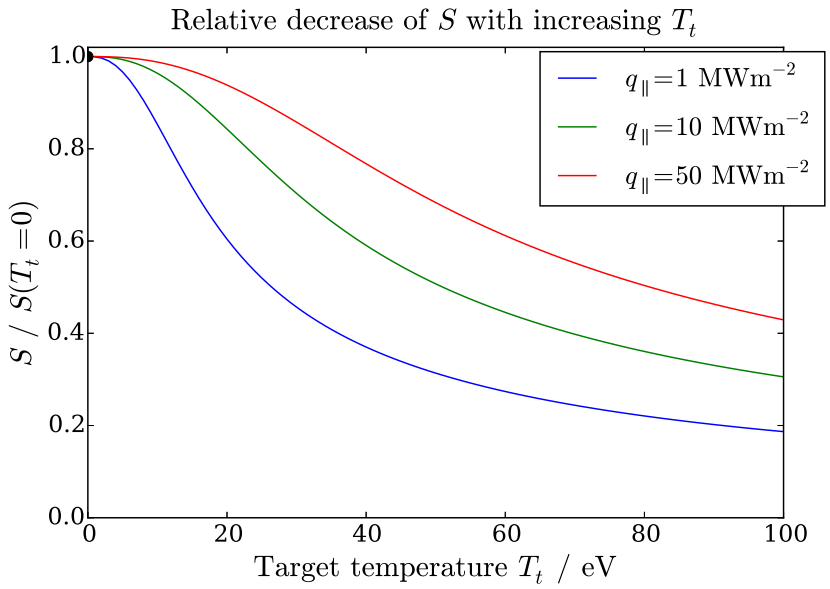

Figure 5.13.: $S(T_t)$ normalised for $T_t = 0$ for different parallel heat fluxes $q_\parallel$.

Comparison to Simulations and Experiments

The absolute values S predicted by equation (5.14) resulting from the above calculation exhibits a deviation with respect to those found by fitted profiles gained from simulations. The relative dependence of S on the target temperature is analysed in this section. The absolute correlation between T_S and T_X is further investigated in the next section.

Figure 5.14 shows the dependence of S on T_t shown in figure 5.13, normalised to the S found for $T_t = 20\,\text{eV}$. The same procedure is applied to values S_{fit} obtained by fitting heat flux profiles from the 2D diffusion simulation. For different values of α and ratios $\frac{S}{\lambda_q}$ the relative correlation of S to T_t is described well. The trend found by integrating along the separatrix and in the 2D simulation resembles the scaling found by A. Scarabosio et al. [28]. Figure 5.15 shows the S found in various experiments in ASDEX Upgrade and JET and simulations mapped upstream for a variety of target temperatures. It is found, that the separatrix temperature $T_{e,tar,sep}$ describes the data set well, with the scaling :

$$\frac{S}{f_x} = (2.3 \pm 0.2)\, T_{e,tar,sep}^{-0,36\pm0.03} \tag{5.19}$$

The deviation from the 1D approximation and 2D heat diffusion simulation to the experiments for temperatures below 20 eV in S is due to processes such as radiation and recombination, not included in the 2D diffusion simulation and the 1D integration. A dependence of the scaling on the exponent α is found. However, the dependence on $q_\parallel$ has to be taken into account and the dependence of S on target temperatures at which this procedure is expected to hold ($T_t > 20\,\text{eV}$) is weak, compared to the scatter of the data. Therefore no conclusions are drawn from this comparison.

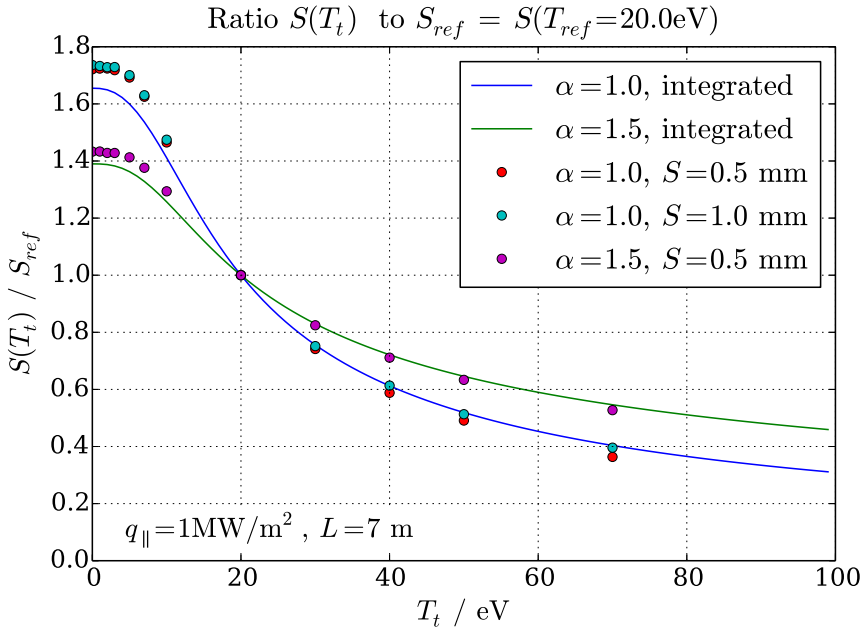

Figure 5.14.: Relative change of S for fixed transport coefficients and geometry with target temperature, using $T_t = 20\,\mathrm{eV}$ as reference for normalisation.

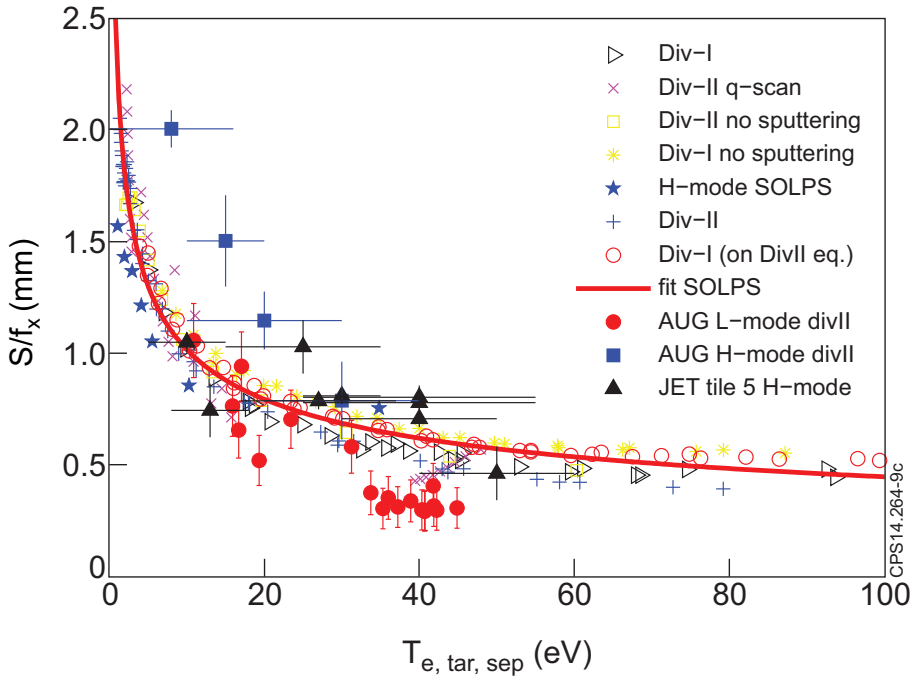

Figure 5.15.: Scaling of S with electron target separatrix temperature $T_{e,\,tar,\,sep}$ in experiments and simulations for two machines found by Scarabosio [28]. The scaling is also applicable for different divertor geometries in ASDEX Upgrade.

5.4. Parameter Study Determining T_S for $T_t = 0$

In this section a parameter study is performed to deduce T_S introduced in section 5.3 from target heat flux profiles obtained in 2D simulations. The correlation of S to the *relevant* temperature T_S in

$$S = L\sqrt{\frac{\chi_{\perp,0}}{\chi_{\parallel,0}}} \cdot T_S^{\frac{\alpha-\beta}{2}} \tag{5.20}$$

follows a trend found by integrating along the separatrix. The correlation

$$\frac{T_S}{T_X} = \left(\frac{2(\beta+1)}{\alpha+\beta+2}\right)^{\frac{-2}{\beta-\alpha}} \tag{5.21}$$

for $T_t = 0$ is checked against values obtained from simulations. The correlation factor according to the analytic approximation is between 0.70 and 0.75, shown in figure 5.11. Figure 5.16 (a) shows the ratio of T_{fit} deduced from S_{fit} and the transport coefficients known in the simulation to the X-point temperature predicted by the two point model and $q \equiv q_0$. Figure 5.16 (b) shows the ratio of T_{fit} to the highest X-point temperature found in the simulation. The latter is below the prediction of the two point model, therefore the ratio T_{fit}/T_X is higher for the X-point temperature being determined as highest temperature found than predicted by the two point model. Both correlation factors are below the range expected from the analytic analysis of 0.70 to 0.75 and show a stronger dependence on α. The increasing ratio for increasing S/λ_q in figure 5.16 (b) compared to 5.16 (a) is explained by the peak temperature decreasing with increasing S. For the case $\alpha = \beta$ no temperature dependency remains to determine T_{fit}. Due to this and because $T_{X,tpm}$ is given by T_t and q_0 this quantity is used in the further evaluation.

Figure 5.17 (a) shows $S(T_S)$ calculated with the zeroth order approximation

$$T_S = \frac{T_X}{2} \tag{5.22}$$

versus S_{fit}. This approximation is justified by the weak dependence of $\frac{T_{fit}}{T_{X,tpm}}$ on $\frac{S}{\lambda_q}$ for the experimental important range $\alpha \simeq 1$ shown in figure 5.16 (a). The exponent $\frac{\alpha-\beta}{2}$ in equation (5.20) approaches zero for increasing α and therefore mitigates the increasing error in T_S with increasing α due to this approximation in the calculation of S. Figure 5.16 (b) shows the error made using this zeroth order approximation versus $\frac{S_{fit}}{\lambda_q}$, being below 20% for the entire range of α and in the order of 1% for $\alpha = 1$, correlating to Bohm diffusion.

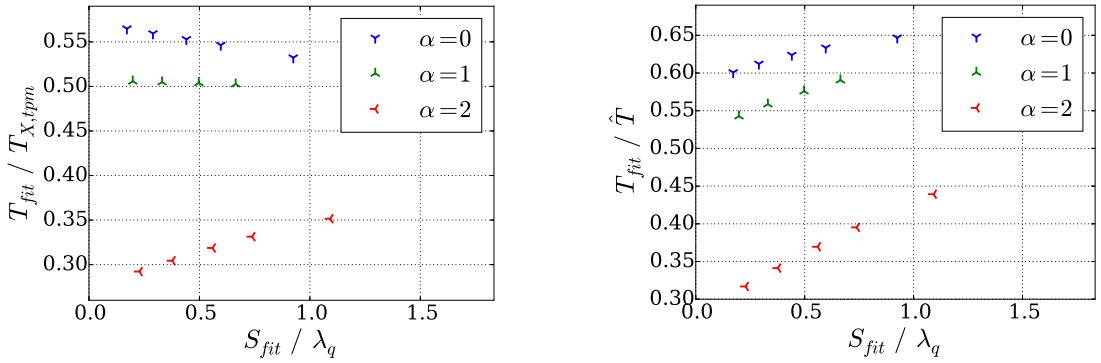

(a) $T_{X,tpm}$ using constant $q \equiv q_0$. (b) Highest X-point temperature $\hat{T}$.

Figure 5.16.: Ratio of T_{fit} to (a) temperature $T_{X,tpm}$ predicted at the X-point by the two point model for constant heat flux density using q_0 and (b) highest X-point temperature $\hat{T}$ found in simulation, plotted versus $\frac{S_{fit}}{\lambda_q}$.

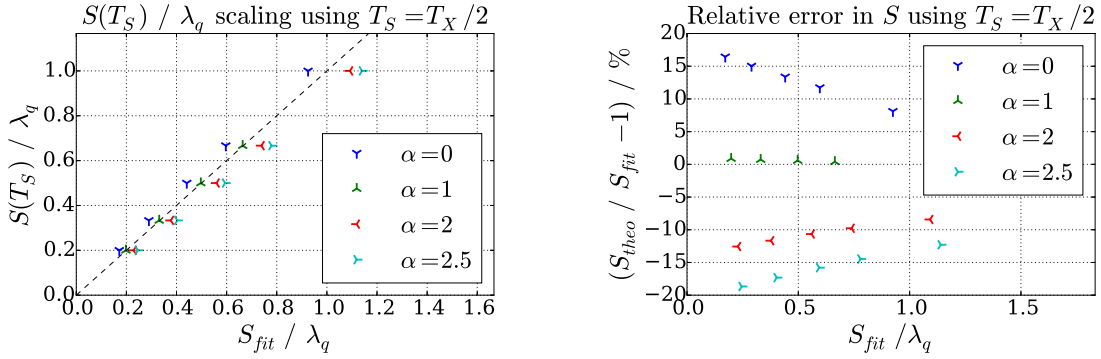

(a) Absolute values $S(T_S)$ to S_{fit}. (b) Erlative error $S(T_S)$ to S_{fit}.

Figure 5.17.: (a) $S(T_S)$ for $T_S = T_{X,tpm}/2$ compared to S_{fit} found by 1D fit function and (b) the relative error.

5.5. Divertor Point Spread Function

In this section the heat flux density profiles obtained by simulations at the target for known X-point profiles are deconvoluted to find a description of the point spread function of the divertor. In the 1D model this function is a symmetric Gaussian, exhibiting characteristic deviations to the point spread function found by deconvolution. This gives rise to question the Gaussian used as spreading function, which is investigated in this section.

The 1D model introduced by T. Eich, which corresponding function is furthermore referred to as Eich fit function, describes diffusion in the divertor region by convolution of the X-point heat flux profile with a symmetric Gaussian as point spreading function (PSF). Results from simulations have a negligible noise level, in contrast to measured data, and the achievable resolution of the heat diffusion code is higher. Therefore the inverse way is possible. Knowing the heat flux at the X-point and at the divertor, the function which represents the broadening by convolution can be deduced. Such an attempt has to be done with caution, because a deconvolution is formally simple, but not necessarily unique and sensible to noise.
Convolving function $f(x)$ with function $g(x)$ to $h(x)$ is denoted:

$$f(x) \otimes g(x) = h(x) \tag{5.23}$$

Applying the Fourier Transform $\mathscr{F}$ and using the convolution theorem yields:

$$\mathscr{F}(f \otimes g) = \mathscr{F}(h) \tag{5.24}$$

$$\mathscr{F}(f) \cdot \mathscr{F}(g) = \mathscr{F}(h) \tag{5.25}$$

Function $g(x)$ is deduced by dividing with $\mathscr{F}(f)$ and applying the inverse Fourier transform:

$$g = \mathscr{F}^{-1}\left(\frac{\mathscr{F}(h)}{\mathscr{F}(f)}\right) \tag{5.26}$$

In the picture of divertor spreading f represents the heat flux at the X-point, h the heat flux in front of the target and g the spreading function. Following the common nomenclature in optics, function g is called point spreading function (PSF) and represents a Gaussian of width S in the 1D model. Main problem of this treatment are high frequencies, with amplitudes in the order or below the noise level of the signal. Additionally, boundary effects have to be taken into account for finite signals.

5.5.1. Characterisation of the Deconvolution

The profiles obtained from the simulation show a negligible noise and the computational area can be chosen wide enough to neglect boundary effects. For $S \simeq 1\,\mathrm{mm}$, $\lambda_q = 3\,\mathrm{mm}$ and $q_0 = 1\,\mathrm{MW\,m^{-2}}$ figure 5.18 (a) shows the heat flux profile resulting from a simulation and the applied Eich fit function. For comparison the X-point profile is included as red dashed line. Figure 5.18 (b) shows the spreading functions found by deconvolution of the target profiles with the X-point. The 1D Model is based on a Gaussian, accordingly found by deconvolution of the fit function. The deconvolution of the heat flux profile from the simulation leads to a function in figure 5.18 (b) shown as blue line. Its peak is narrower than the Gaussian with a slower decrease after one to two decay lengths S in the SOL and PFR. Figure 5.18 (c) shows the deviation of the PSF found by deconvolution to the Gaussian with width S in percent with respect to the peak of the Gaussian. The shape of this deviation and its asymmetry is characteristic for different temperature dependencies α of the perpendicular diffusivity.

Figure 5.19 shows the deviation from the PSF to the Gaussian as introduced in figure 5.18 (c) for different α and constant $\frac{S}{\lambda_q}$. The lowest deviation is found for $\alpha = 2.5 \equiv \beta$, describing the same temperature dependence for perpendicular and parallel transport. In this case the PSF is symmetric, because the ratio of the diffusivities shows no temperature and therefore no spatial dependence. The PSF is closest to the Gaussian for $\alpha = \beta$. The deviation increases and an asymmetry develops for decreasing α in the range $0 \leqslant \alpha < \beta$. The least similarity to the Gaussian is found for $\alpha = 0$, for which the perpendicular transport has no temperature dependence. Reason is the lower temperature in the PFR compared to the SOL, resulting in a stronger perpendicular transport compared to the parallel transport and therefore stronger spreading of the parallel heat flux. The simulated data are better described using alternative fit functions.

Using the same temperature dependence for the perpendicular and parallel transport ($\alpha = \beta$), the shape of the target heat flux profile and with it the deviation of the PSF to the Gaussian is independent of the exponents, as long as the ratio of the diffusivities is constant.

A quantifier of the asymmetry is the ratio between the local minimum of the deviation on the right side to the minimum at the left side, further called γ. It is found, that this ratio does not depend on the divertor length L and q_0, but on the ratio $\frac{S}{\lambda_q}$. Figure 5.20 shows the dependence of the ratio γ on $\frac{\alpha}{\beta}$ for two ratios of S to λ_q. The

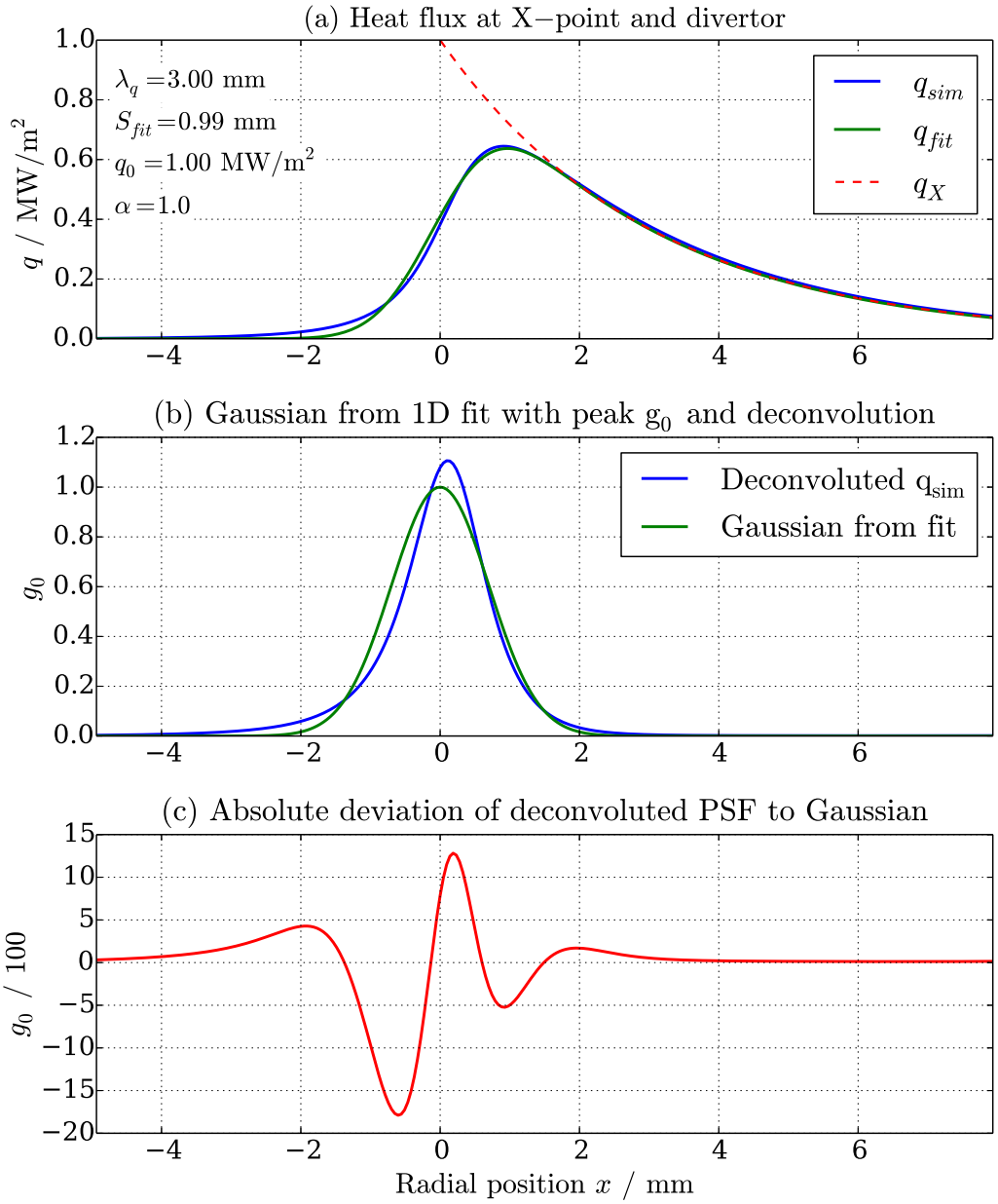

Figure 5.18.: (a) Comparison between heat flux density at target for $\alpha = 1$ in the simulation and best Eich fit and heat entering the divertor region at the X-point.
(b) Gaussian described by S of Eich fit and result of deconvolving divertor and X-point profiles, normalised to the peak of the Gaussian.
(c) Absolute deviation of deconvolved PSF to Gaussian in percent of Gaussian peak.

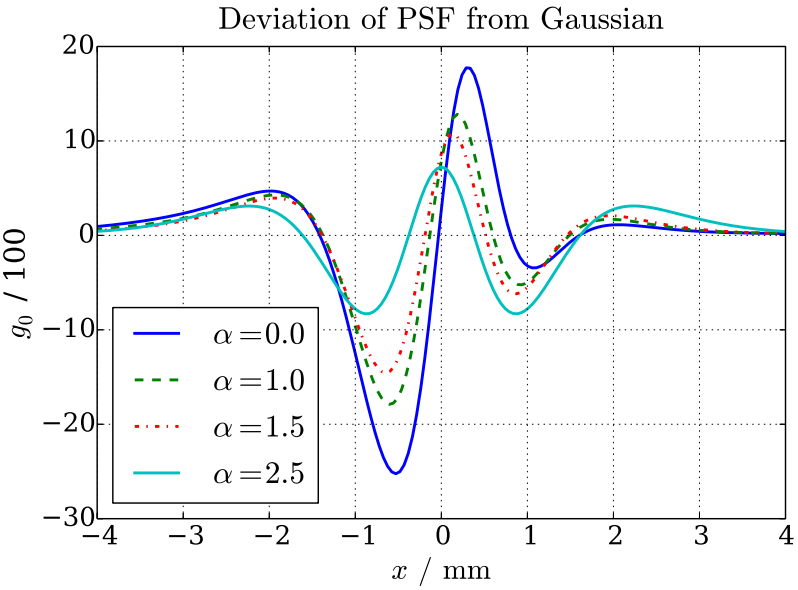

Figure 5.19.: Deviation of PSF to Gaussian for different α. $S = 1\,\mathrm{mm}$, $\lambda_q = 3\,\mathrm{mm}$, $q_0 = 1\,\mathrm{MW\,m^{-2}}$. For decreasing α, the magnitude of the deviation increases and the shape becomes asymmetric.

experimental relevant range of α is 1 to 1.5, referring to Bohm and Gyro-Bohm diffusion. On the x-axis this refers to the range 0.4 to 0.6 for Spitzer-Härm conduction in parallel orientation with $\beta = 2.5$. The best description is found using a hyperbolic sine with offset:

$$\gamma(S/\lambda_q = 1/3) = (0.1482 \pm 0.0039) \cdot \sinh\left((2.473 \pm 0.026)\frac{\alpha}{\beta}\right) + (0.1192 \pm 0.0022)$$

$$\gamma(S/\lambda_q = 1/6) = (0.1037 \pm 0.0043) \cdot \sinh\left((2.888 \pm 0.040)\frac{\alpha}{\beta}\right) + (0.0698 \pm 0.0035)$$

The sinh describes the trend better than an exponential or a power law, with uncertainties in the parameters in the order of 1%. No interpretation for this function is attempted.

This correlation can be used to derive α from a deconvoluted heat flux pattern for given S and λ_q. This requires to know the X-point heat flux profile and assumes negligible target temperatures. Applying the introduced deconvolution procedure to measured heat flux profiles results in a PSF with a too low resolution and too high noise of about 20-30% to make conclusions about α. Reducing the noise using a Wiener filter in the frequency domain is not sufficient to deduce α. It is up to future work to test this procedure with better measurements or more sophisticated

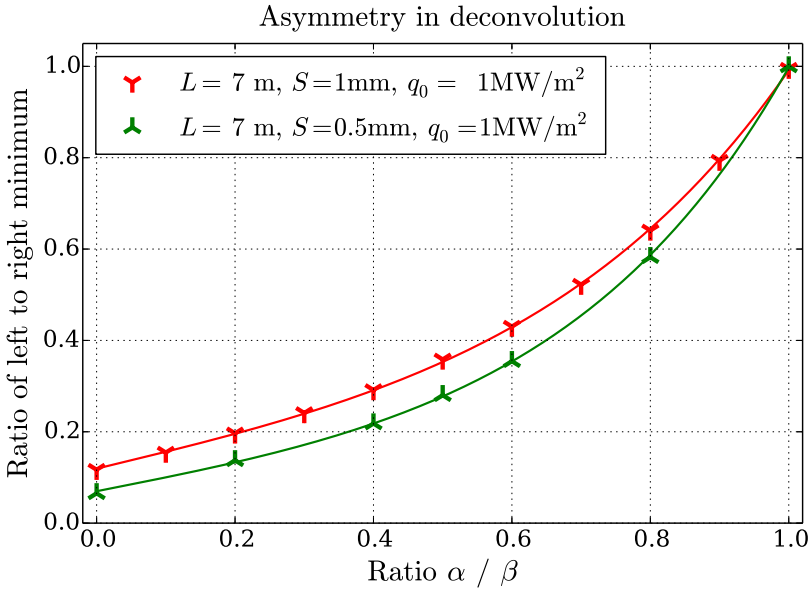

Figure 5.20.: Relation of right to left minimum in the difference from the deconvoluted profile against the gaussian versus α for $\beta \equiv 2.5$.

procedures.

Figure 5.21 shows the deconvolution procedure shown in figure 5.18 applied to a measured profile. The noise in the deviation to the Gaussian is in the order of the expected signal (figure 5.19).

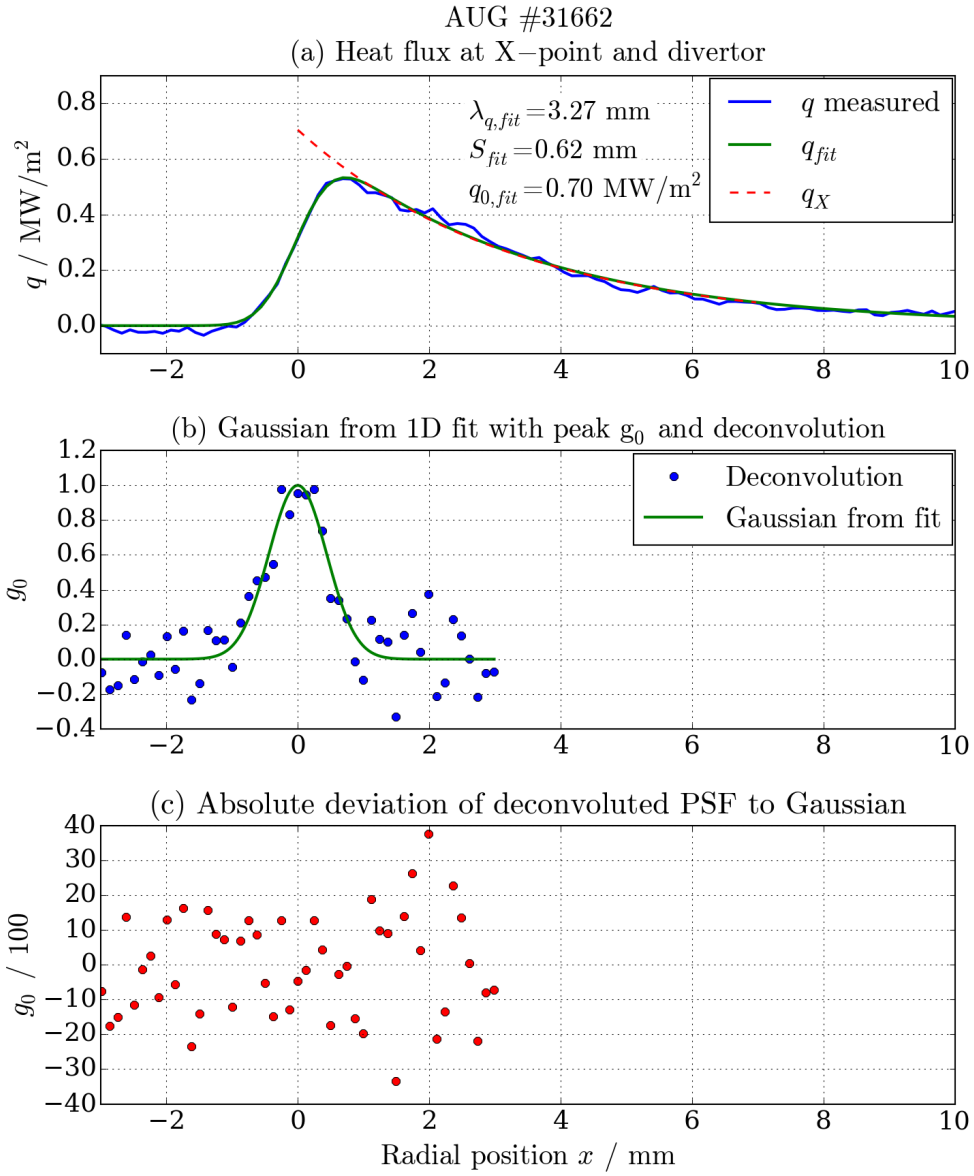

Figure 5.21.: (a) Comparison between measured heat flux density to the target, Eich fit and assumed exponential profile at the X-point in the 1D model. (b) Gaussian described by S of Eich fit and result of deconvolving divertor and X-point profiles, normalised to the peak of the Gaussian. (c) Absolute deviation of deconvolved PSF to Gaussian in percent of Gaussian peak.

5.5.2. Alternative Point Spread Function

The deconvolution method introduced above leads to a point spreading function (PSF) different from the Gaussian as fundamental solution of the 1D heat equation. Different fit functions are introduced and compared in order to achieve a better description of target heat flux profiles.

Cosh as PSF

The best description of the PSF for $\alpha = \beta$ is found to be a symmetric function with single exponential decay for both directions, given by the inverse of the *symmetric* cosh function:

$$g_{sym}(x) = \frac{n}{\exp(+\frac{x}{S}) + \exp(-\frac{x}{S})} \propto 1/\cosh\left(\frac{x}{S}\right) \tag{5.27}$$

n is a normalisation factor. Figure 5.22 shows this function fitted to the PSF obtained for $\alpha = \beta$. The absolute error with respect to the peak of the PSF is in the order of 10^{-4}.

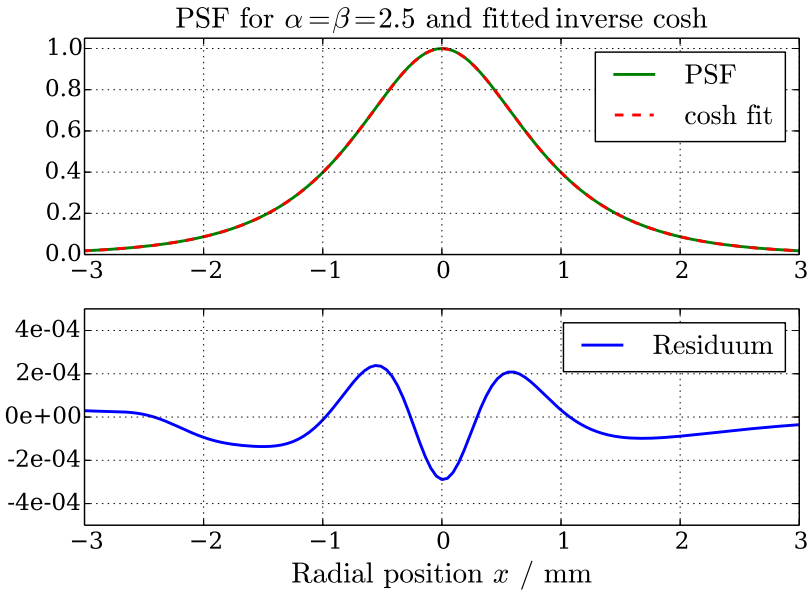

Figure 5.22.: Symmetric cosh fitted to deconvoluted point spread function for $\alpha = \beta$ in the simulation.

For $\alpha < \beta$ the PSF is not symmetric. Assuming an exponential decay with different fall-off length in the PFR and SOL leads to define what is further called the

asymmetrical cosh function:

$$g_{asym}(x) = \frac{n}{\exp\left(+\frac{x+x_0}{S_r}\right) + \exp\left(-\frac{x+x_0}{S_l}\right)} \tag{5.28}$$

n is a normalisation factor and x_0 expresses a radial offset. Figure 5.23 shows the inverse asymmetric cosh fitted to the PSF obtained for $\alpha = 1$, $\beta = 2.5$. The absolute error with respect to the peak of the PSF is in the order of 1%, whereas the Gaussian defined by the Eich fit deviates up to 18% for this profile, see figure 5.19.

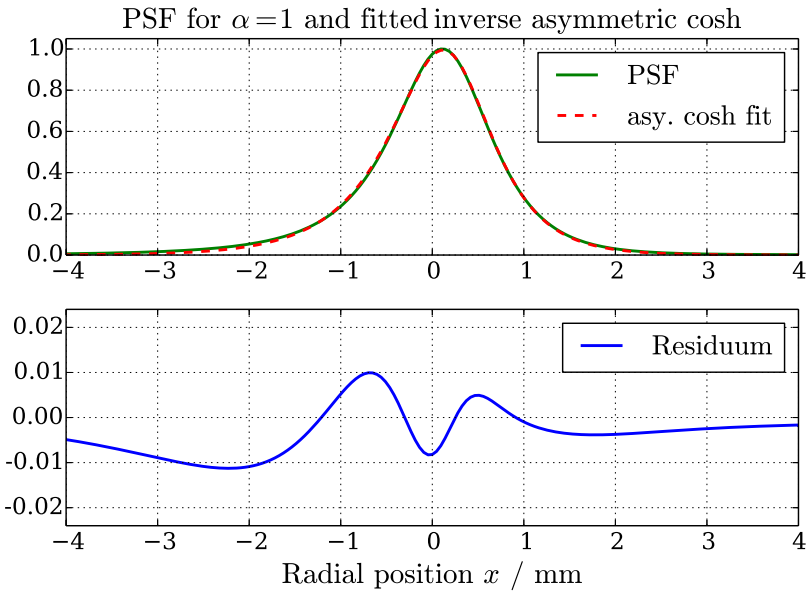

Figure 5.23.: Asymmetric cosh fitted to deconvoluted point spread function for $\alpha = 1$ in the simulation.

Figure 5.24 shows the Eich fit function applied to a heat flux profile from a simulation. Parameters are $q_0 = 100\,\mathrm{MW\,m^{-2}}$, $S = 1\,\mathrm{mm}$ and $\lambda_q = 3.0\,\mathrm{mm}$. The shown residuum therefore is in percent of q_0. The deviation is about 2 to 3 %, with its peak in the PFR and a visual less pronounced deviation at the separatrix and heat flux peak. The alternative fit functions in the following are compared to the same profile. The separatrix position is best described by the Eich fit.

Figure 5.25 shows the fit of an inverse asymmetric cosh convoluted to an exponential to a heat flux profile. The deviation is about 0.6% of q_0, therefore a factor 5 below the results of the Eich fit, shown in figure 5.24 for comparison. The values q_0 and λ_q deduced by the fit are in agreement to the boundary conditions of the simulation. As expected for $\alpha < \beta$ the spreading S_{PFR} in the PFR is larger than S_{SOL} in the SOL.

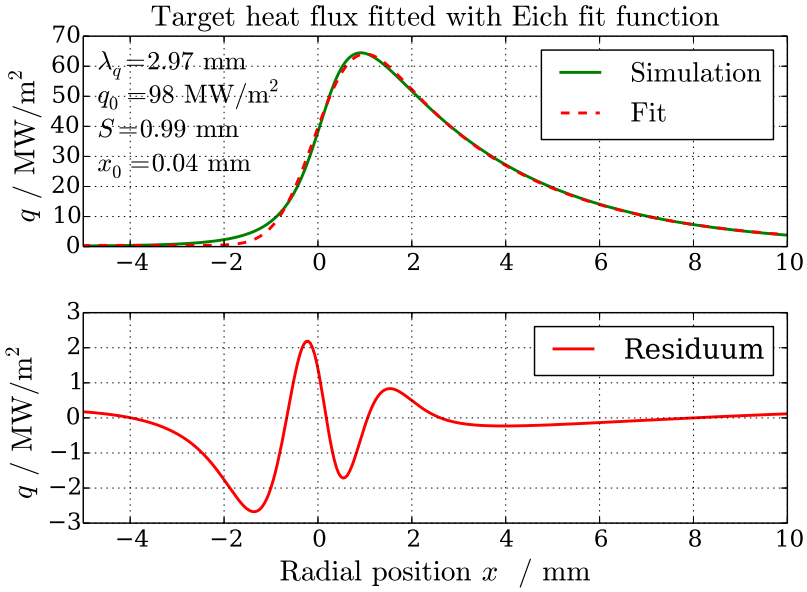

Figure 5.24.: Eich function fitted to target heat flux profile.

This values are not comparable to the Gaussian S. For a large divertor spreading the relative error in S_{SOL} and λ_q increases, as the radial decay of the profile in the SOL is described by both parameters. However, S_{SOL} affects the shape of the peak, mitigating this in parts for $S \simeq \lambda_q$.

Up to now no analytic formulation for the convolution of the exponential decay at the X-point and this new PSF has been found. The performed analysis includes a process of minimising the RMS, performing the needed convolution for every parameter set including 6 parameters. Those are λ_q and q_0 in the exponential, S_{PFR} and S_{SOL} as decay lengths and x_0 in the cosh and an offset q_0. However, the PSF found is shaped similar to the actual power density profile on the target and is in applicable without convolution.

Another quantification for the asymmetry than the ratio γ is to calculate the skewness of the PSF, not addressed in this work. Using different moments of the PSF is expected to identify α more precise for noise levels and resolutions found in measurements.

For $\alpha < \beta$ the temperature profile affects the local spreading in terms of perpendicular to parallel diffusivity, implying a temperature and therefore a radial dependence of heat flux spreading. No expression to correlate these different fall of lengths to the temperature or heat flux decay length is found.

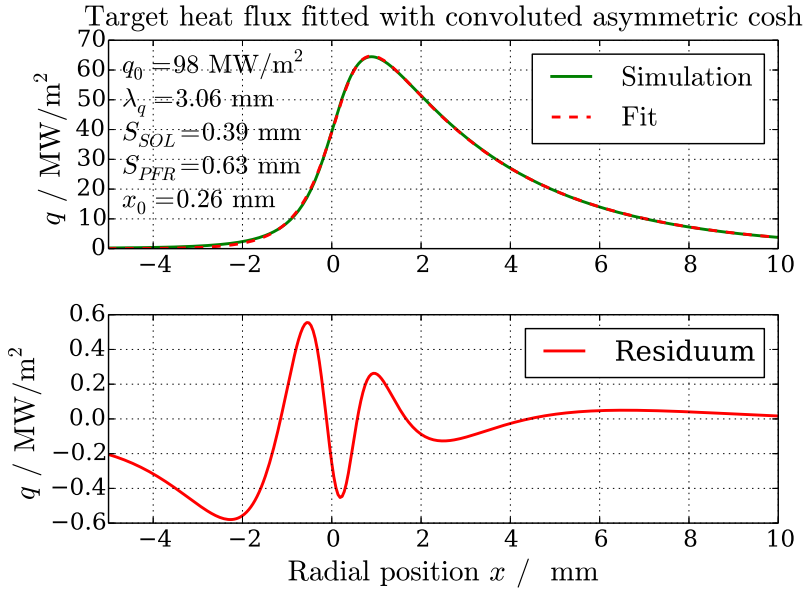

Figure 5.25.: Fit of the asymmetric cosh convoluted with an exponential.

Cosh without Convolution

The asymmetric cosh is used to describe the heat flux density profile without convolution to an exponential. The direct cosh (DC) function is defined to be:

$$q_{DC}(x) = q_0 \frac{2}{\exp(\frac{x-x_0}{\lambda_{SOL}}) + \exp(-\frac{x-x_0}{\lambda_{PFR}})} \tag{5.29}$$

It describes an exponential decay with decay length λ_{SOL} of the heat flux profile into the SOL, as given at the X-point and translated to the target, as well as into the PFR with decay length λ_{PFR}, arising from diffusion. λ_{PFR} describes the spreading into the PFR, but is not called S to distinguish it from the spreading described by the point spread functions. q_0 in this formulation yields the heat flux density at $x = x_0$, being below the peak heat flux for different λ_q. Figure 5.26 shows function q_{DC} fitted to a target heat flux profile and the residuum of the fit. The peak heat flux in the simulation is $q_0 = 100\,\mathrm{MW\,m^{-2}}$. For different ratios $\frac{S}{\lambda_q}$ the value q_0 in introduced function does not describe this value. Figure 5.24 shows the same heat flux profile fitted with the Eich fit for comparison, with about double the deviation in the PFR compared to the DC function.

The description of the heat flux profiles with the asymmetric cosh without convolution to an exponential is better than for the Eich fit. The computational effort to perform

a fit is lower than using an explicit convolution, resulting in a similar shaped profile. The peak heat flux q_0 is not described well, depending on the ratio $\frac{S}{\lambda_q}$.

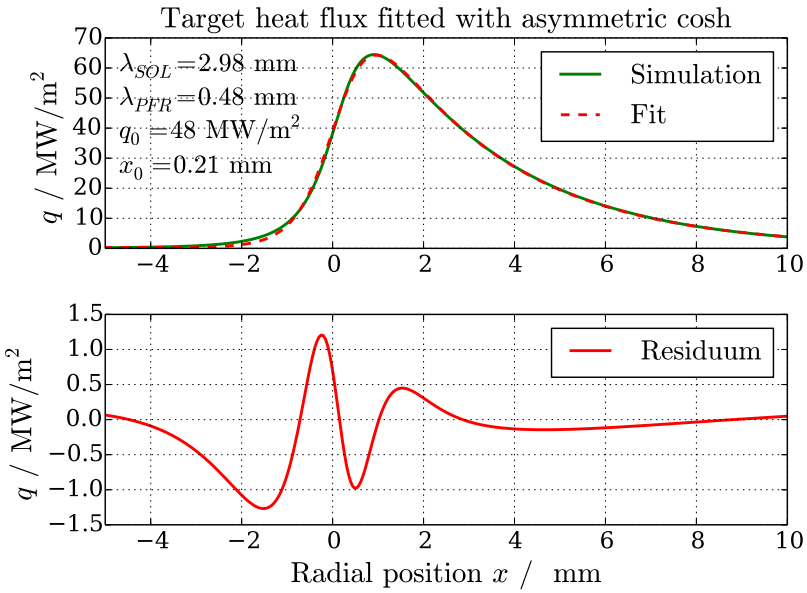

Figure 5.26.: Asymmetric cosh without convolution fitted to target heat flux profile. λ_q at the X-point is found as right fall-off length λ_{SOL}. λ_{PFR} describes the decay in the PFR well.

Asymmetric Gaussian as PSF

As an asymmetric Gaussian PSF is defined step wise with two distinct S for the SOL and PFR:

$$f(x) = \begin{cases} c \exp\left(-\left(\frac{x}{S_{PFR}}\right)^2\right) & x \leqslant 0 \\ c \exp\left(-\left(\frac{x}{S_{SOL}}\right)^2\right) & x > 0 \end{cases} \tag{5.30}$$

Fitting the convolution of this asymmetric Gaussian with an exponential to heat flux profiles from measurements and simulations shows no benefit compared to the Eich function. This is because the decay of the heat flux in the SOL is not described by a Gaussian, as found by deconvolution.

5.5.3. Comparison between S in Inner and Outer Divertor

Applying the Eich fit function to target heat flux profiles measured in ASDEX Upgrade results in different heat flux decay lengths for the inner ($\lambda_{q,in}$) and outer ($\lambda_{q,out}$) target. Assuming these values to be equal – mapped to the outer midplane to compensate f_x – at the corresponding side of the X-point, the fit can be applied to both profiles using the same λ_q. The introduced fit functions with distinct fall-off lengths for the SOL and PFR can enlarge the λ_q from X-point to target. Therefore the lower of the λ_q, found in the inner divertor, is used as fixed parameter for the fit of the profile of the outer divertor.

None of the fit functions describes the profile well with a too low λ_q. Using an averaged λ_q for both divertors is also not successfully, as a λ_q chosen too large can not be compensated by perpendicular diffusion.

As example figure 5.27 shows the heat flux density profile measured with IR diagnostic in ASDEX Upgrade in the inner divertor. Figure 5.28 shows the heat flux measurement at the same time in the outer divertor. For the red curve the Eich fit with λ_q as fit parameter is used, resulting in S_o, $\lambda_{q,o}$ and $q_{0,o}$. The blue curve is obtained by setting $\lambda_{q,i}$ fix in the fitting procedure.

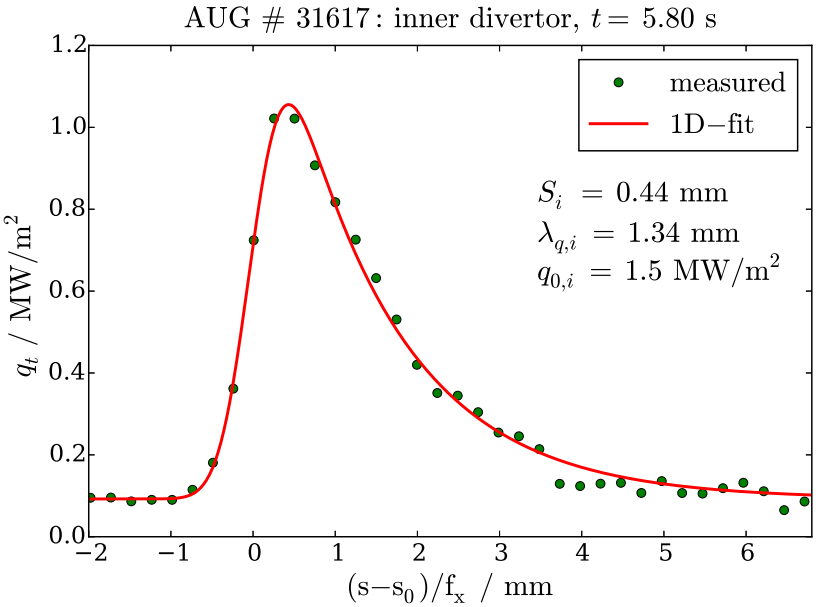

Figure 5.27.: Inner divertor heat flux density profile from IR diagnostic and 1D model.

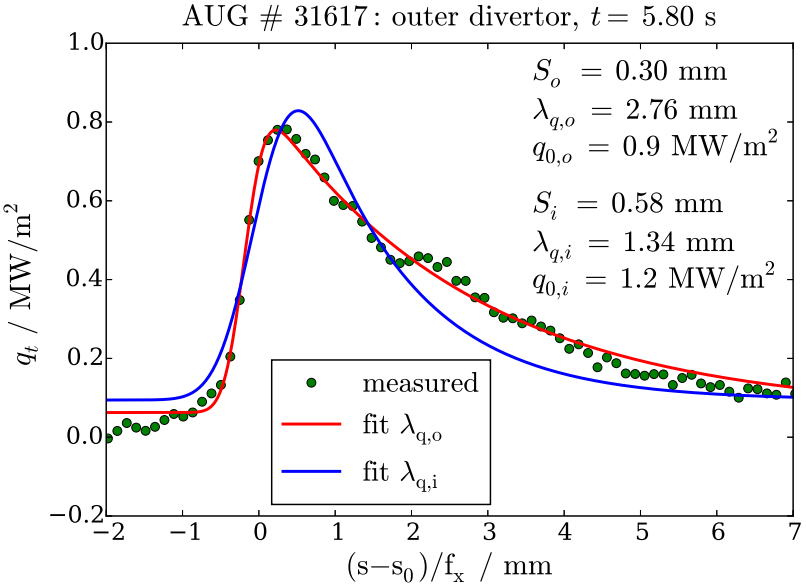

Figure 5.28.: Outer divertor fitted with Eich fit function for free $\lambda_{q,o}$ and for $\lambda_{q,i}$ fixed from fit of inner profile, see figure 5.27.

6.Summary and Conclusion

In this chapter the content of this thesis is summarised and the results are discussed. This includes comparisons between an 1D and a 2D description of heat diffusion in the divertor region of a tokamak to the target and target heat flux density profiles measured in ASDEX Upgrade. Alternative fit functions to describe the target heat flux profiles are deduced from deconvolving the target and X-point profile, yielding the point spread function of the divertor. None of the functions describes the heat flux profiles in the inner and outer divertor with a single heat flux decay length λ_q. In the end an outlook for further simulations and analysis methods is given.

Numerical Solution of the 2D Heat Diffusion Equation

A code to solve the 2D heat diffusion equation for temperature and density dependent diffusion coefficients is developed. Applicable boundary conditions are a constant temperature, constant heat flux and a heat flux dependent temperature to mimic sheath transport. The code solves the differential equations utilising the heat transport potential with an alternating direction implicit Crank-Nicolson method.

For transport parallel and perpendicular to the magnetic field Spitzer-Härm-like diffusion with constant, arbitrary temperature dependencies is implemented. Other transport mechanisms like convection and radiation are neglected and drift terms are not taken into account.

Comparison of 1D Model to 2D Simulation

Fitting the 1D diffusive model explained in section 2.3 to the target heat flux density profiles obtained by solving the 2D heat diffusion equation numerically describes the profiles, but exhibits a characteristic deviation at the separatrix and in the PFR. This deviation is found for different but also the same temperature dependencies for parallel and perpendicular transport. A similar deviation is also observed in experiments.

An approximation to the parallel heat flux density profile is found by assuming a linear dependence of S on the relative position between X-point and target (section 5.2).

Deconvolution

The 1D model describes the target heat flux profile by convolution of the X-point profile to a Gaussian of width S, which is the fundamental solution to the 1D heat diffusion equation assuming a constant parallel diffusion time.

It is found by deconvolution of the heat flux density profile at the target and the X-point, that the Gaussian described by the 1D model deviates to the point spread function found by solving the 2D heat diffusion equation. An inverse cosh for equal temperature dependence of parallel and perpendicular transport describes the deconvolution of simulated heat flux profiles (section 5.2). The point spread function is symmetric for equivalent diffusion models parallel and perpendicular to the magnetic field. Differing temperature dependencies in the diffusivities result in a temperature dependence of the heat spreading. As the temperature in the private flux region is lower than in the scrape-off layer, the point spread function is asymmetric and described with different decay lengths in the SOL and PFR. The difference in the decay lengths is assumed to be connected to the radial temperature profile in the divertor region. A qualifier is found, describing the difference in the temperature dependence of the heat diffusivites, in the difference of the deconvoluted point spread function to the Gaussian described by the 1D model.

In contrast to the simulation the measured profiles, obtained by IR thermography, exhibit noise. The noise level of the available data is too high to deduce the temperature dependence of the perpendicular heat diffusion. However, the presented method is expected to be applicable to other simulations, to quantify transport parameters.

Alternative Fit Function

A set of fit functions differing to the 1D model are introduced and compared. The convolution of the asymmetric inverse cosh with an exponential describes the target heat flux profiles best. The alternative description of the PSF leads to different spreading values, being not comparable to the 1D model parameter S. The 1D diffusive model connects the profile broadening to perpendicular diffusion in the divertor region. For the alternative fit functions investigated in this thesis no such interpretation is yet available.

Connecting Inner and Outer λ_q

Different heat flux decay lengths λ_q are found in experiments for the inner and outer divertor [27]. Using different spreading functions, including the description by the 1D model, does not describe experimental target heat flux density profiles in the inner and outer divertor with a single λ_q (section 5.5.3). No conclusion about the heat flux above the X-point is drawn.

Outlook

The code developed and used in the framework of this thesis offers the option to include spatially varying diffusion coefficients, due to the magnetic configuration in tokamak experiments. This can be used to study different diffusion models like Bohm and Gyro-Bohm diffusion, depending on the magnitude of the magnetic field.

For comparison to experiments the sheath condition can be refined and a proper pressure model – deducible with the same code applied to particle diffusion – has to be used.

Describing the heat flux density profiles at the X-point for the low and high field side of single null configurations allows to investigate and quantify the heat exchange in the PFR between the two sides. This exchange may not be negligible, requiring an analysis of both heat flux profiles in combination.

Heat losses due to radiation in the divertor region are neglected, which is a valid approximation for plasma with low density ($\simeq 10^{-19}\,\mathrm{m}^{-3}$) and high temperature ($> 20\,\mathrm{eV}$) in the SOL. Adding a temperature and density dependent loss term is compatible with the code developed.

A study for the applicability of the ratio $T_S = \frac{T_X}{2}$ for the *relevant temperature* T_S to calculate S based on equation (5.20) with experimental data for validation of diffusive transport in the divertor region is suggested.

Appendices

A.Numerics

I. Matrix Representation for CN with ADI

Section 3.5.5 explained the discretisation with the Crank Nicolson method (CN) using the alternate direction implicit (ADI) method, leading to a linear system of equations. Using matrix representation leads to a tridiagonal system with M equations:

$$\boldsymbol{A}\boldsymbol{u}^{k+1/2} = \boldsymbol{b}^{k} \tag{A.1}$$

Values in $\boldsymbol{b}$ at time step k are known, $\mathbf{u}$ contains the unknowns at time step $k + \frac{1}{2}$. An example is shown for an arbitrary column j, which index will be dropped for simplicity. Setting the heat potential u_{BC} as boundary at $i = 0$ and the heat flux density q as boundary condition at $i = M$ the system writes as

$$\begin{pmatrix} 1+2\gamma & -\gamma & 0 & \dots & 0 \\ -\gamma & 1+2\gamma & -\gamma & 0 & 0 \\ \vdots & \ddots & \ddots & \ddots & \vdots \\ 0 & 0 & -\gamma & 1+2\gamma & -\gamma \\ 0 & \dots & 0 & -\gamma & 1+\gamma \end{pmatrix} \cdot \begin{pmatrix} u_1^{k+1/2} \\ u_2^{k+1/2} \\ \vdots \\ u_{M-1}^{k+1/2} \\ u_M^{k+1/2} \end{pmatrix} = \begin{pmatrix} \gamma(\, u_2^k + 2 \cdot u_{BC}) + (1-2\gamma)u_1^k \\ \gamma(u_{i-1}^k + u_{i+1}^k) + (1-2\gamma)u_i^k \\ \vdots \\ \gamma(u_{M-2}^k + u_M^k) + (1-2\gamma)u_{M-1}^k \\ 2\gamma\, \Delta y\, q + \gamma u_{M-1}^k + (1-\gamma)u_M^k \end{pmatrix}$$

The boundary conditions are interchangeable as demanded by the problem, this constellation is used to illustrate both conditions.

Thomas algorithm is then used to solve the tridiagonal system, explained in the next section.

II. Solving a tridiagonal equation system

Thomas algorithm is a simplified variant of the Gaussian elimination algorithm and allows to solve equations of the form

$$\boldsymbol{Au} = \boldsymbol{x} \tag{A.2}$$

with tridiagonal matrix $\boldsymbol{A} \in \mathbb{R}^{N \times N}$ efficiently with $\mathcal{O}(N)$. A tridiagonal matrix is sparse with non zero elements only at the diagonal and entries one row below and above. Therefore the non-zero elements are written down as three vectors $\boldsymbol{a}$, $\boldsymbol{b}$ and $\boldsymbol{c}$:

$$\boldsymbol{A} = \begin{pmatrix} b_1 & c_1 & & & & 0 \\ a_2 & b_2 & c_2 & & & \\ & a_3 & b_3 & c_3 & & \\ & & \ddots & \ddots & \ddots & \\ & & & a_{N-1} & b_{N-1} & c_{N-1} \\ 0 & & & & a_N & b_N \end{pmatrix}$$

Decomposition and forward substitution, solving equations recursive for u_i, we define

$$c'_i = \left\{ \begin{array}{c} \frac{c_1}{b_1} : i = 1 \\ \frac{c_i}{b_i - c'_{i-1} \cdot a_i} : i > 1 \end{array} \right\}$$

and

$$d'_i = \left\{ \begin{array}{c} \frac{x_1}{b_1} : i = 1 \\ \frac{x_i - x'_{i-1} a_i}{b_i - c'_{i-1} \cdot a_i} : i > 1 \end{array} \right\}$$

The solution $\boldsymbol{u}$ is found by backward substitution

$$u'_i = \left\{ \begin{array}{c} \frac{x'_i}{\vdots} i = N \\ \frac{x_i - c'_i u_{i+1}}{\vdots} i < N \end{array} \right\}$$

The actual Fortran code used to solve the system of linear equations for the alternating direction implicit method introduced in section 3.5.5 based on [29]:

```
Subroutine NRtrisol(N, D, UD, LD, X, B)
  ! Solver for problem given by tridiagonal Matrix A * x = b with
  !  x to be found

  ! pre-condition:
  !  integer N: length of the vectors
  !  double precision vectors D, UD, LD: Diagonal, Upper and Lower
  !   Diagonal elements of A
  !  double precision vectors X, B: Known and unknown quantities
  ! post-condition:
  !  double precision vector X: result of A * x = b

  Integer, Intent(IN):: N
  double precision, dimension(N), Intent(INOUT):: X
  double precision, dimension(N), Intent(IN):: D, UD, LD, B
  double precision, dimension(N):: ws
  double precision:: tmp
  integer:: ii

  ! Forward substitiution
  tmp = D(1)
  X(1) = B(1) / tmp

  Do ii = 2, N
    ws(ii) = UD(ii-1) / tmp
    tmp = D(ii) - LD(ii) * ws(ii)
    X(ii) = (B(ii) - LD(ii) * X(ii-1) ) /tmp
  End Do

  ! Backward substitution
  Do ii = N-1, 1, -1
    X(ii) = X(ii) - ws(ii+1) * X(ii+1)
  End Do

End Subroutine NRtrisol
```

Bibliography

[1] Prof. Dr. Frank Jenko. “Plasmaphysik 2”. In: (2014).

[2] IPP. www.aug.ipp.mpg.de. Accessed at 30.09.15.

[3] PD Dr. Emanuele Poli. “Plasmaphysik 1”. In: (2014).

[4] EUROfusion. www.euro-fusion.org. Accessed at 23.09.15.

[5] E. Barbato, G. Tardini, and H. Zohm. “On the use of Lower Hybrid Current Drive in ASDEX Upgrade”. eng. In: European Physical Society, 2004.

[6] Felix Reimold. *Experimental Studies and Modeling of Divertor Plasma Detachment in H-Mode Discharges in the ASDEX Upgrade Tokamak*.

[7] M. Keilhacker and ASDEX Team. “The ASDEX divertor tokamak”. In: *Nuclear Fusion* 25.9 (1985), p. 1045. URL: http://stacks.iop.org/0029-5515/25/i=9/a=008.

[8] T. Eich et al. “Scaling of the tokamak near the scrape-off layer H-mode power width and implications for ITER”. In: *Nuclear Fusion* 53.9 (2013), p. 093031. URL: http://stacks.iop.org/0029-5515/53/i=9/a=093031.

[9] “Interpretation of the deep cracking phenomenon of tungsten monoblock targets observed in high-heat-flux fatigue tests at 20 MW/m2”. In: *Fusion Engineering and Design* 101 (2015), pp. 1 –8. ISSN: 0920-3796. DOI: http://dx.doi.org/10.1016/j.fusengdes.2015.09.008.

[10] B Sieglin et al. “Power load studies in JET and ASDEX-Upgrade with full-W divertors”. In: *Plasma Physics and Controlled Fusion* 55.12 (2013), p. 124039. URL: http://stacks.iop.org/0741-3335/55/i=12/a=124039.

[11] Bernhard Sieglin. *Divertor Power Load Studies in All Metal ASDEX Upgrade and JET*.

[12] B.K. Venkanna. *Fundamentals of Heat and Mass Transfer*. Prentice-Hall Of India Pvt. Limited, 2010. ISBN: 9788120340312.

[13] A Herrmann et al. “Energy flux to the ASDEX-Upgrade diverter plates determined by thermography and calorimetry”. In: *Plasma Physics and Controlled Fusion* 37.1 (1995), p. 17. URL: http://stacks.iop.org/0741-3335/37/i=1/a=002.

[14] P. L. Bhatnagar, E. P. Gross, and M. Krook. “A Model for Collision Processes in Gases. I. Small Amplitude Processes in Charged and Neutral One-Component Systems”. In: *Phys. Rev.* 94 (3 May 1954), pp. 511–525. DOI: 10.1103/PhysRev.94.511.

[15] Michael Kaufmann. *Plasmaphysik und Fusionsforschung*. 2nd. Springer, 2013. DOI: 10.1007/978-3-658-03239-5.

[16] David Bohm. “The characteristics of electrical discharges in magnetic fields”. In: *New York: McGraw-Hill* (1949).

[17] A Taroni. “Global and local energy confinement properties of simple transport coefficients of the Bohm type”. In: *Plasma Physics and Controlled Fusion* 36 (1994). URL: http://iopscience.iop.org/0741-3335/36/10/003.

[18] C M Roach. “Modelling ohmic confinement experiments on the START”. In: *Plasma Physics and Controlled Fusion* 38 (1996). URL: http://iopscience.iop.org/0741-3335/38/12/011.

[19] A. Loarte, S. Bosch, A. Chankin, et al. “Multi-machine scaling of the divertor peak heat flux and width for L-mode and H-mode discharges”. In: *Journal of Nuclear Materials* ().

[20] M. A. Makowski et al. “Analysis of a multi-machine database on divertor heat fluxesa)”. In: *Physics of Plasmas* 19.5, 056122 (2012).

[21] Bernhard Unterberg. “Transport processes in the plasma edge”. In: *Fusion science and technology* 53.2 T (2008). ISSN: 1536-1055.

[22] R.J. Goldston. “Heuristic drift-based model of the power scrape-off width in low-gas-puff H-mode tokamaks”. In: *Nuclear Fusion* 52.1 (2012), p. 013009. URL: http://stacks.iop.org/0029-5515/52/i=1/a=013009.

[23] Marco Wischmeier. “Simulating Divertor Detachment in the TCV and JET Tokamaks”. PhD Thesis. École Polytechnique Fédérale de Lausanne.

[24] B. Sieglin et al. “Real time capable infrared thermography for ASDEX Upgrade”. In: *Review of Scientific Instruments* 86.11, 113502 (2015).

[25] C. Hopf. Max-Planck-Institut für Plasmaphysik; Laboratory Course Experiment ’Elektrische Sonden im Plasma’.

[26] Robert J. Goldston. “Downstream heat flux profile versus midplane T profile in tokamaks”. In: *Physics of Plasmas* 17.1, 012503 (2010).

[27] M Faitsch et al. “Change of the scrape-off layer power width with the toroidal B-field direction in ASDEX upgrade”. In: *Plasma Physics and Controlled Fusion* 57.7 (2015), p. 075005. URL: http://stacks.iop.org/0741-3335/57/i=7/a=075005.

[28] A. Scarabosio, T. Eich, F. Hoppe, et al. “Scaling of the Divertor Power Spreading (S-factor) in Open and Closed Divertor Operation in JET and ASDEX Upgrade”. In: *EFDA-JET* ().

[29] William H. Press et al. *Numerical Recipes*. third edition. Cambridge University Press, 2007.